Instrument development for exploring the influence of interfacial chemistry on aerosol growth, aging, and partitioning of gases

Cecilia Lynn Amick

Dissertation submitted to the Faculty of the

Virginia Polytechnic Institute and State University

in partial fulfillment of the requirements for the degree of

Doctor of Philosophy

in

Chemistry

John R. Morris, Chair

Linsey C. Marr

Brian M. Tissue

Gabriel Isaacman-VanWertz

October 31, 2019

Blacksburg, Virginia

Keywords: Instrumentation, atmospheric chemistry, aerosols, cavity ring-down spectroscopy

Instrument development for exploring the influence of interfacial chemistry on aerosol growth, aging, and partitioning of gases

Cecilia Lynn Amick

(ABSTRACT)

Investigation of aerosol chemistry and growth under atmospheric conditions in a novel rotating aerosol suspension chamber with cavity ring-down spectroscopy provided key insight into the effect of pollutants and other vapors on the overall atmospheric lifetime of particulate matter. The Atmospheric Cloud Simulation Instrument (ACSI) creates a well-defined and controllable atmosphere of suspended particles, analyte gases, and background gas molecules, which remains stable up to several days. Preliminary studies have shown that monodisperse polystyrene latex ($d_p = 0.994$ µm) and polydisperse ammonium sulfate (CMD $d_p = 100$ nm) particles remain suspended for at least 22 hours while the chamber rotates at 2 RPM. Further investigation into the aerosol dynamics showed the coagulation efficiency of high concentration particle suspensions (>10^6 particles/cm^3) depends on particle phase state and composition. The coagulation efficiency decreased with increased humidity in the model atmosphere and with increased ion concentrations in the aerosols. The decrease in efficiency is attributed to repulsive forces from like-charges on the particle surfaces. In addition to humidity, the spectroscopy integrated into the main chamber monitors the real-time response to a perturbation in the model atmosphere, such as the introduction of a gas-phase reactant. Cavity ring-down spectroscopy, performed *in situ* along the center axis, records mid-infrared spectra (1010 cm^{-1} to 860 cm^{-1}) to identify gas species evolved from gas-particle heterogeneous chemistry. In accord with previous studies, my results show that a known reaction between monomethyl amine and ammonia occurs readily on suspended ammonium sulfate particles in >50% RH and the extent of the reaction depends on the humidity of the model atmosphere. Acidic ammonium bisulfate aerosols also produced a detectable amount of ammonia upon exposure to monomethyl amine in a model atmosphere with >50% RH. Overall, the new ACSI approach to atmospheric science provides the opportunity to study the influence of interfacial chemistry on particle growth, aging, and re-admission of gas-phase compounds.

Instrument development for exploring the influence of interfacial chemistry on aerosol growth, aging, and partitioning of gases

Cecilia Lynn Amick

(GENERAL AUDIENCE ABSTRACT)

"Molecules don't have a passport." - Carl Sagan. Gas molecules and particles emitted into the atmosphere in one area can travel thousands of kilometers over the course of hours to days, even weeks for some compounds. The gas-solid interactions that occur over the lifetime of particulate matter are largely unknown. I focused my doctorate on bridging the knowledge gap between traditional environmental monitoring research and highly controlled laboratory experiments. To do so, I designed a new instrument capable of creating stable model atmospheres that more accurately simulate the gas-particle interactions in Earth's atmosphere than previous environmental chambers. The Atmospheric Cloud Simulation Instrument design included a rotating chamber to increase the duration of stable particle suspensions in a laboratory and a multi-pass infrared spectrometer to monitor gas-phase reactions *in situ*. I explored the effect of humidity and particle composition on particle-particle coagulation and gas-particle reactions. For example, liquid aerosols at humidities higher than 35% RH do no coagulate as fast as a solid particle with the same composition in <35% RH. Similarly, the same liquid aerosols produced more gaseous product during a heterogeneous reaction with a 'pollutant' gas than solid particles. Overall, the ACSI will be an important tool for future experiments exploring individual aspects of complex atmospheric processes.

Dedication

For my husband and family

Acknowledgments

First, I'd like to acknowledge my family, especially my parents. You instilled in me a strong work ethic and perseverance to endure challenges. To my dad– thank you for teaching me how to troubleshoot problems, whether it was mathematical or mechanical, I still use those skills today. To my mom–thank you for setting an amazing example for me as a career woman in the sciences. You showed me it's possible to have everything I wanted, including a career and a family. To my brother, Jason–thanks for encouraging me to follow in the footsteps of our grandfather, the first person in our family to earn a doctorate. Your words of encouragement led me to this point, where I'm acknowledging you in my very own dissertation, thank you.

To my husband Josh. We met during my second year, right before the whirlwind of the literature review and preliminary exam. Your unwavering support has encouraged me not to give up, even when the thought of completing this degree felt impossible. I'm lucky to have met you when I did.

To my pseudo, graduate school family I gained while at Virginia Tech: Dr. Chrissy DuChane, and Dr. Matt and Kiaya Vincent. Thank you for listening to all of the rants about my project, relationships, and life in general. Knowing I could count on you helped me through some tough times.

To my research group–thanks for asking interesting questions during group meetings and welcoming an atmospheric pressure chamber to a UHV research lab. I'd like to especially thank Dr. Guanyu Wang, we supported and commiserated with each other at each milestone, from the preliminary exam to the ORP and beyond. I cherish our friendship.

Finally, I'd like to thank my research advisor, Dr. John Morris. Thank you for challenging me to question my data beyond the obvious and perform as many experiments as possible "while the sun's shining." I believe I am a better analytical chemist than when I joined your group. I could not have completed as ambitious of a project as building an instrument from scratch without your expertise. Thank you.

Contents

List of Figures

List of Tables

List of Abbreviations

χ	Shape correction factor
η	Dynamic gas viscosity
γ	Sticking coefficient for particle collisions
λ	Wavelength of light
λ_g	Mean free path of gas molecules
λ_p	Mean free path of a particle
ν	Frequency of light
ω	Angular velocity
$\overline{c}$	Particle mean thermal velocity
$\overline{K}$	Coagulation coefficient for a polydisperse suspension of particles
ρ_0	Density of water, 1.0 g/cm^3
ρ_p	Density of the particle
$\sigma(\nu)$	Frequency-dependent absorption cross section for one absorbing species
σ_g	Geometric standard deviation
τ	Particle residence time
$\tau(\nu)$	Frequency-dependent ring-down time
ε	Dielectric constant of the medium
ε_0	Permittivity of vacuum
$A(\nu)$	Frequency-dependent absorbance
C	Undiluted particle concentration before n samples
c	Speed of light
C_c	Cunningham correction factor
C_d	Diluted particle concentration after n samples
C_m	Particle mass concentration
D	Diffusion coefficient for particles
d	Optical path length

$d(t)$	Particle diameter at time, t
d_a	Aerodynamic particle diameter
d_e	Effective particle diameter
d_m	Collision diameter
d_o	Initial particle diameter
d_p	Diameter of the particle
dn/dt	Rate of collisions between the selected particle and the other particles
dN/dx	Concentration gradient of the particles at the collision surface of the selected particle
dn_c/dt	Rate of collisions per unit volume
E	Electric field
e	Charge of an electron
f_n	Fraction of particles of size d_p that has n surface charges
g	Gravitational acceleration constant
$I(\nu, t)$	Intensity of light at a specific frequency after entering the CRDS optical cavity as a function of time
$I_o(\nu)$	Initial light intensity after one pass through the CRDS optical cavity
J	Particle flux at the surface of a given particle
K	Corrected coagulation coefficient
k	Exponential decay constant
k_b	Boltzmann's constant
K_E	Constant of proportionality based on the units used in f_n (9.0×10^9 N $\cdot$ m^2/C^2)
K_o	Coagulation coefficient
$K_{1,2}$	Coagulation coefficient for two different sized particles
L	Distance between the CRDS mirrors
N	Number concentration
n	Number of surface charges on a particle
n	Refractive index

N/N_o	Particle number suspension efficiency
n_s	Number of samples taken from chamber
$p^o_{\mathrm{H_2O}}$	Saturation vapor pressure of water
$p_{\mathrm{H_2O}}$	Partial pressure of water vapor
R	Radius of the chamber
r	Distance between two particle centers
$R(\nu)$	Frequency-dependent mirror reflectivity
r_0	Radius of the particle area
t	Time
V/V_o	Particle volume suspension efficiency
V_{tot}	Total volume of the chamber
V_s	Total particle sample volume (sample flow rate × sample time)
V_{TE}	Terminal electrostatic velocity
W_c	Coulomb force correction factor for coagulation
z_i	Charge of particle i, including sign
$\mathrm{PM}_{2.5}$	Particulate matter smaller than 2.5 μm in diameter
ACSI	Atmospheric Cloud Simulation Instrument
APS	Aerodynamic particle sizer
CMD	Count median diameter
CRDS	Cavity Ring-down Spectroscopy
DMA	Differential mobility analyzer
DMS	Dimethyl Sulfide
DRH	Deliquescence relative humidity
EC	Elemental carbon
ERH	Efflorescence relative humidity
FWHM	Full width half maximum
HITRAN	High Resolution Transmission spectral database

MCT	Mercury cadmium telluride
MFC	Mass flow controller
NO_x	Oxides of nitrogen (NO, NO_2, NO_3)
nss-sulfate	Non-sea-salt sulfates
OA	Organic aerosol
OC	Organic carbon
ppb	Parts per billion
ppm	Parts per million
PSLs	Polystyrene latex particles
PV-MCT	Photovoltaic Mercury cadmium telluride detector
RH	Relative humidity
RPM	Rotations per minute
SCCM	Standard cubic centimeters per minute
SLPM	Standard liters per minute
SMPS	Scanning mobility particle sizer
SOA	Secondary organic aerosol
TIC	Toxic industrial compound
UA	Urban aerosols
UHP N_2	Ultra high purity nitrogen
UHV	Ultra High Vacuum
ZnSe	Zinc Selenide

.

Chapter 1

Introduction and Motivation

1.1. Thesis Statement

The objective of this project is to develop a novel instrument and corresponding experimental method for exploring heterogeneous reactions between atmospheric gases and aerosols through non-destructive, *in situ* spectroscopic monitoring of the gas species while maintaining a stable particle suspension.

1.2. Background

Aerosols, liquid droplets, and other particles that persist in our atmosphere undergo physical and chemical changes due to particle-particle interactions and reactions with gas molecules. Chemical reactions occurring in the atmosphere facilitate new particle formation,[1–3] changes in volatility,[4] and even act as atmospheric "sinks", or removal process, for some pollutants.[5–7] Currently, researchers employ various techniques to study aerosol chemistry, such as direct atmospheric monitoring,[8] fundamental vacuum studies,[9] single particle levitation,[10] and cloud chambers.[11,12] Each approach has drawbacks: atmospheric monitoring lacks experimental control, vacuum studies are performed on a fixed particle bed under non-atmospheric conditions, particle levitation only provides information on a single particle, not a distribution of particles, and particles quickly settle out or deposit on the walls of cloud chambers. Most cloud chambers also require a large laboratory space.[11,12] I designed the Atmospheric Cloud Simulation Instrument (ACSI) to extend particle suspension duration, spectroscopically monitor changes in gas composition *in situ*, and maintain a relatively compact design. The instrument design and method development described in the following chapters address the following objectives:

1. Design an instrumental approach for exploring particle growth over extended durations.

2. Develop experimental methods that enable simultaneous monitoring of gas-phase composition and particle size distributions over time.

3. Use the instrument to study of the emission of interfacial reaction products that result from a perturbation to the atmospheric conditions.

The following sections in Chapter 1 provide background information on particulate matter and gases that play a major role in heterogeneous atmospheric chemistry.

1.2.1. Atmospheric Particulate Matter

Teragrams of particulate matter are released into the atmosphere every year.[13] Aerosol composition varies based on the source, size, and overall reactivity of the material. The major natural, or biogenic, sources include wind-blown mineral dust, volcanic dust, combustion, and sea spray aerosols. Anthropogenic, or man-made, particle sources consist of industrial dust, combustion, and vehicle emissions. Particle source and composition will be described further in Section 1.2.1.2. Aerosols are also characterized by size: coarse mode (>2.5 μm), accumulation mode (0.1–2.5 μm), and Aitken mode (10 nm–0.1 μm). Heterogeneous chemistry alters the aerosol composition as particles persist in the atmosphere, a process also known as aerosol aging.

Coarse mode particles remain in the atmosphere for less than a few hours, which is the shortest lifetime of the three size ranges.[13] Efficient sedimentation results in the short atmospheric residence times for coarse particles and do not persist in the atmosphere long enough to experience extensive atmospheric aging. Therefore, coarse particles will not be explored experimentally in this dissertation.

Aitken mode particles are also referred to as ultrafine particles. Aitken mode particle generation is dominated by condensation of molecules from the vapor phase.[13,14] The main

condensable vapors involved in particle generation are water, sulfuric acid, and high molecular weight volatile organic compounds (VOCs). A comprehensive description of particle nucleation and condensation can be found in Pandis and Seinfeld.[15] Continued condensation and coagulation, or the process of particles colliding and adhering with one another,[16] are the major removal processes for Aitken mode particles. Both processes eventually produce accumulation mode-sized particles.[13,14] Ultrafine particles, though short-lived, undergo the beginning stages of aerosol aging. The ACSI is designed to explore ultrafine aerosol growth and aging in a controlled, model atmosphere.

Particles between 0.1–2.5 μm, also referred to as fine particulate matter or $PM_{2.5}$, persist in the atmosphere for the longest amount of time due to inefficient removal processes. There are two major types of removal processes: dry and wet 'sinks'. Dry sinks include deposition and coagulation.[14] Deposition for $PM_{2.5}$ can be neglected because the sedimentation velocity for this size range is <0.1 cm/s. A substantial amount of self-coagulation, or coagulation between similarly sized particles, is required to increase the particle size by an order of magnitude. Therefore, coagulation of ultrafine and fine particulate matter with larger, pre-existing particles is the main dry removal process for accumulation mode aerosols. Coagulation of only $PM_{2.5}$ is too slow to produce coarse mode particles.[17] For example, Whitby defined the turn-over time for particles as the total mass concentration of the primary particle divided by the mass flux adding to the pre-existing particle population due to coagulation, which approximates the amount of time a specific-sized particle remains suspended in the atmosphere.[18] The turn-over time solely from dry coagulation in low humidity and low concentrations of condensable vapors is 1 hour to 100 days.[14,18,19] However, a more practical turn-over time of 3–30 days for accumulation mode particles includes wet particle loss processes as well as dry coagulation.[14,19] See Section 1.2.1.1 for more information on aerosol coagulation. All three objectives of my thesis seek to lay the foundation for interpreting the effect of various model atmospheres on fine and ultrafine aerosol dynamics.

The interaction between existing particles and clouds is referred to as cloud processing,

which is considered a wet sink for $PM_{2.5}$. Clouds mainly consist of liquid water and ice aerosols and water mass concentrations ranging from 0.05 to 3 g/m^3, depending on cloud type and location. Clouds are effective at reducing fine particle concentrations. For example, Jaenicke and Ogren and Charlson found that the 12 hour median concentration of fine particulates inside Arctic fog was <0.1 particles/cm^3 and >100/cm^3 outside of the fog.[19,20] Hygroscopicity of the particle, cloud type and cloud frequency affects the cloud processing of fine particulates.[13,14] Fine particulates in tropical climate remain suspended for less than a day and remain in the atmosphere for several weeks in an Arctic climate..[14]

Vapor condensation, coagulation, and cloud processing change the internal and external composition of the original aerosols.[14] Internal mixing denotes an even mixture of compounds throughout the particle and external mixing indicates layers or sections of different types of particulate material. The atmospheric lifetimes of $PM_{2.5}$ permit the particles to transform into complex mixtures of condensable materials, different types and sizes of primary particles, and other heterogeneous reaction products. Figure 1.1 illustrates the complex aging processes for each size range of particles. In general, the reactions involved in aging processes oxygenate the aerosols, which eventually leads to the wet deposition of particulate matter. However, the effect of each individual reaction contributing to the overall aging process on aerosol lifetimes needs to be studied further. The ACSI was designed to control, explore, and understand specific mechanisms involved in the multi-day aging processes of fine particulate matter.

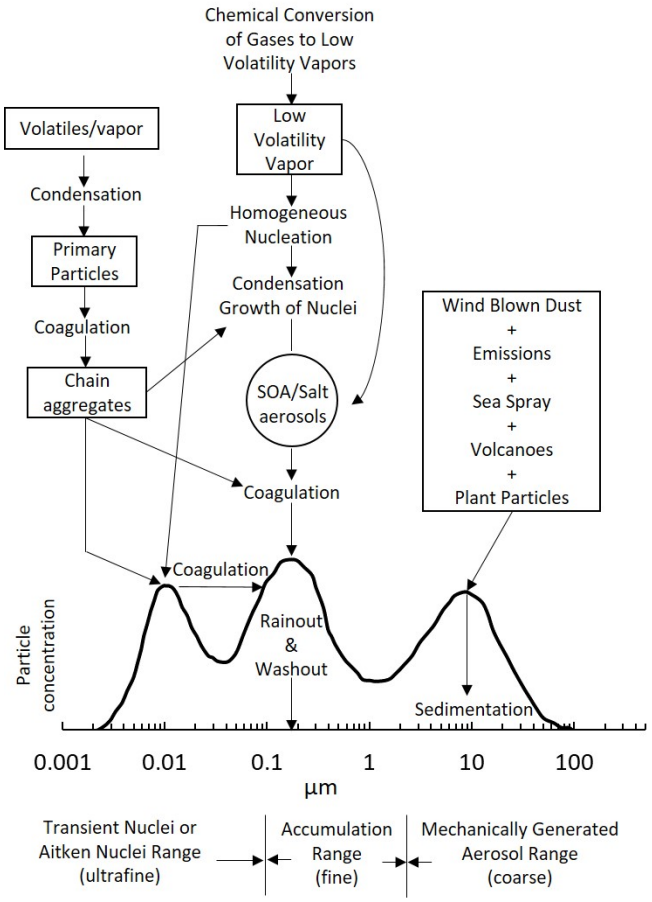

Figure 1.1: Illustration of aerosol aging processes for ultrafine, fine and coarse particulate matter. The figure is adapted from reference 13.

1.2.1.1. Aerosol Dynamics

Vapors partition into the particle phase and particles undergo coagulation, both processes increase particle size over time, see Figure 1.1. Condensation results in larger particles and higher particle mass or volume concentrations while maintaining a stable particle number concentration. Eventually, condensation alone could increase the particle size to over 1–2 µm without directly reducing the number of particles. High particle concentration areas permit particle-particle collisions, initiating coagulation. Unlike condensation, coagulation increases particle size while the particle number concentration decreases as particles collide and adhere. The particle mass or volume concentration remains unchanged during coagulation. The following derivation mathematically describes how particle suspensions change over

time due to coagulation beginning with a simple monodisperse system. The computational model is then applied to polydisperse suspensions. Chapter 3 describes the application of the computational model to analyze changes in polydisperse, fine particle number and volume concentrations suspended in various model atmospheres.

The following coagulation derivation from Hinds assumes the suspension is comprised of monodisperse, hard spheres with diameters (d_p) > 0.1 μm.[16] The first step in the derivation is to determine the particle collisional frequency in a suspension. The particle flux (J) at a selected particle surface is defined using Fick's first law of diffusion, Equation 1.1.

$$J = -D\frac{dN}{dx} \tag{1.1}$$

N is the particle concentration and dN/dx is the particle concentration gradient at the collision surface, and D is the diffusion coefficient for a particle of size d_p (Equation 1.2).

$$D = \frac{k_b T C_c}{3\pi\eta d_p} \tag{1.2}$$

Equation 1.2 depends on temperature (T), the Cunningham slip correction factor (C_c), the dynamic gas viscosity (η, Equation A.1), and particle diameter (d_p). The Cunningham slip correction factor, C_c, accounts for small particles 'slipping' on a collisional surface (see Equations A.2 and A.3).[16] The effect of slip on collisions decreases as particle size increases. The gas mean free path of air (λ_g) is 0.066 μm at 760 Torr and 293 K (Equation A.4).[16] Gas mean free path is only used in the calculations for the Cunningham slip correction factor and the analytical solution derived for the polydisperse particle coagulation coefficient, described later in this section (Equation 1.21).

The rate of collisions (dn/dt) of surrounding particles on the selected particle surface is defined as the product of the surface area (A_s) and flux (J) (Equation 1.3). Particles of diameter, d_p, have a collisional surface area equal to the surface area of a sphere with a

diameter of $2d_p$.

$$\frac{dn}{dt} = A_s J = -\pi(2d_p)^2 D\frac{dN}{dx} \tag{1.3}$$

Fuchs provided the solution for the concentration gradient at the collision surface for particles with a diameter larger than the particle mean free path (Equation 1.4).[21] The mean free path of a particle (λ_p), defined as the average distance the center of a particle travels before it completely changes direction, is the product of the particle relaxation time and the mean thermal velocity of the particle (Equation 1.5).

$$\frac{dN}{dx} = -\frac{2N}{d_p} \qquad \text{for } d_p > \lambda_p \tag{1.4}$$

$$\lambda_p = \tau\bar{c} = \tau\left(\frac{48k_bT}{\pi^2\rho_p d_p^3}\right)^{1/2} \tag{1.5}$$

Particle relaxation time (τ) is the amount of time required for a particle to 'relax' to a new velocity under a new force. Relaxation time depends on the particle density (ρ_p), particle diameter (d_p), the Cunningham slip correction factor (C_c), and the dynamic gas viscosity (η).

$$\tau = \frac{\rho_p d_p^2 C_c}{18\eta} \tag{1.6}$$

Substitution of Equation 1.4 into Equation 1.3 results in the rate of collisions of surrounding particles with a selected particle (dn/dt, Equation 1.7).

$$\frac{dn}{dt} = 8\pi d_p DN \tag{1.7}$$

The rate of collisions per unit volume (dn_c/dt) accounts for the number of particles per unit of volume (N) and incorporated a factor of 1/2 to avoid double counting the collisions.

$$\frac{dn_c}{dt} = \frac{N}{2}(8\pi d_p DN) = 4\pi d_p DN^2 \tag{1.8}$$

The change in particle concentration over time (dN/dt) is equal but opposite to the rate of collisions per unit volume under the assumption that every collision results in the adherence of two particles. The constants in Equation 1.9 are combined to generate the coagulation coefficient for a monodisperse distribution (K_o). I defined a scalar, γ, that represents a sticking coefficient of each collision, or the probability that the collisions results in particle coagulation. The following integration of Equation 1.9 yields the an analytical solution to predict the change in number concentration over time for an initially monodisperse suspension. The following derivation expands the definition of K_o to apply to any polydisperse aerosol suspension.

$$\frac{dN}{dt} = -\gamma 4\pi d_p D N^2 = -\gamma K_o N^2 \tag{1.9}$$

$$K_o = 4\pi d_p D = \frac{4k_b T C_c}{3\eta} \tag{1.10}$$

Under the assumption that the particle diameter is larger than the particle mean free path ($d_p > \lambda_p$), Equation 1.4 does not accurately describe the concentration gradient within one particle mean free path of the particle surface when the particle diameter approaches 0.4 μm. Therefore, Fuchs provided values for a correction factor, β, to adjust the coagulation coefficient (K_o) as particle size decreases.[21] For example, the correction factor for particles with a diameter of 0.1 and 0.4 μm is 0.82 and 0.95, respectively (see Figure A.1).

$$K = K_o \beta \tag{1.11}$$

Equation 1.9 is rearranged so like variables are together then integrated over some interval of time ($0 \rightarrow t$), which results in an analytical solution to predict particle concentration after some amount of time (t). N_o is the initial particle concentration and $N(t)$ is the particle concentration after some interval of time. The solution, conveniently, is an equation of a

straight line. Kim et al. determined K from the slope of experimental data according to Equation 1.13, a technique that is explored further in Chapter 3.[22] Figure 1.2 shows a representative plot for determining the coagulation coefficient from the slope of a straight line for various particle sizes.

$$\int_{N_o}^{N(t)} \frac{dN}{N^2} = \int_0^t -\gamma K dt \tag{1.12}$$

$$\frac{1}{N(t)} - \frac{1}{N_o} = \gamma K t \tag{1.13}$$

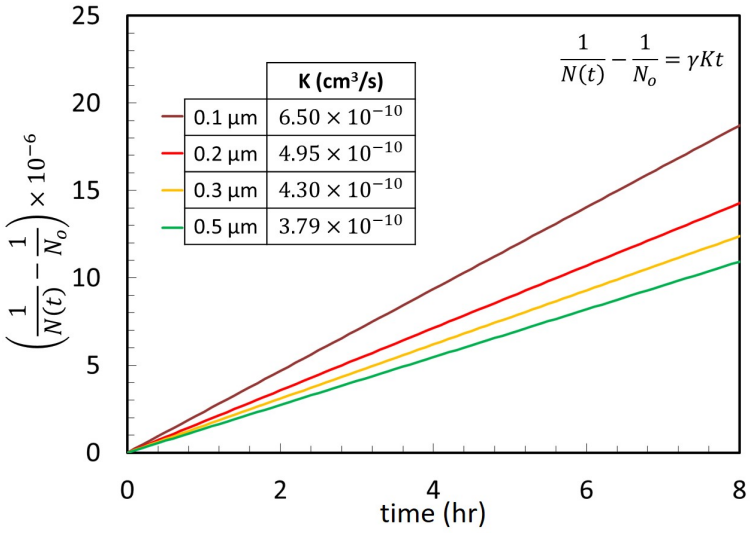

Figure 1.2: Calculated plot of Equation 1.13 for various initial sizes of monodisperse particles. The inset provides the size-corrected coagulation coefficient for each size. The initial concentration (N_o) is $10^5/\text{cm}^3$ for each size.

Rearranging Equation 1.13 yields the function for particle concentration over time due to coagulation. Equation 1.14, along with an experimental γK, can be used to model the number suspension efficiency in a chamber over time. Chapter 3 describes the application of Equations 1.13 and 1.14 to data collected with the ACSI, which includes plots similar to Figure 1.2 and 1.3.

$$\frac{N(t)}{N_o} = \frac{1}{1 + N_o \gamma K t} \tag{1.14}$$

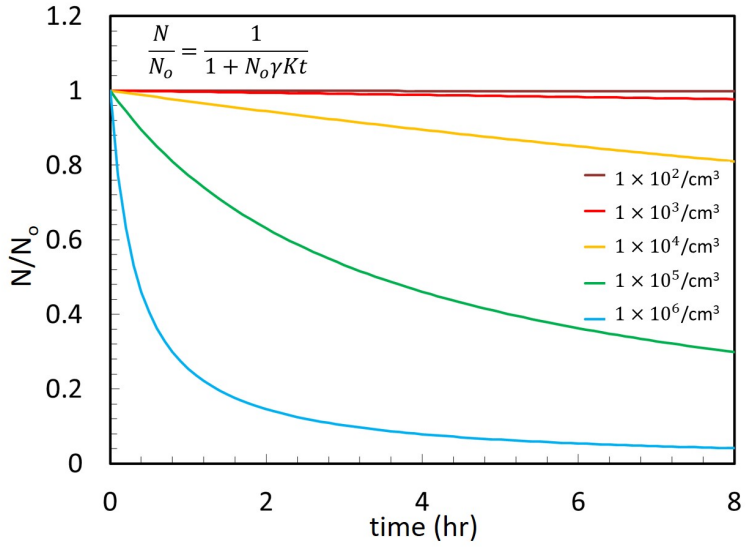

Figure 1.3: Calculated change in particle number concentration for monodisperse, 0.1 µm, standard particles at various initial concentrations over 8 hours.

Particle number concentration decreases with each collision, assuming each collision results in two particles adhering to one another (Equation 1.9). As stated before, the total particle mass and volume concentrations remain constant. Therefore, the mass or volume concentration can be used to predict the average diameter of the coagulated particles (Equation 1.15).

$$C_m = N_o \frac{\pi}{6} \rho_p d_o^3 = N(t) \frac{\pi}{6} \rho_p d(t)^3 \tag{1.15}$$

The diameter of the coagulated particles can be calculated at any time (t) using Equation 1.17 for an initially monodisperse particle suspension under the assumption there is no loss in total particle mass during coagulation. Figure 1.4 shows the increase in particle diameter due to coagulation over time according to Equation 1.17 for monodisperse 0.1 µm particles.

$$\frac{d(t)}{d_o} = \left[\frac{N_o}{N(t)}\right]^{1/3} \tag{1.16}$$

$$d(t) = d_o(1 + N_o \gamma K t)^{1/3} \tag{1.17}$$

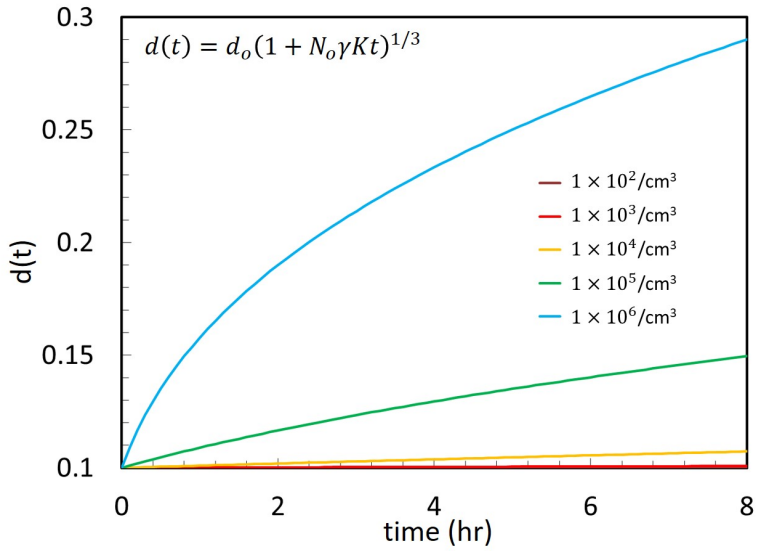

Figure 1.4: Calculated change in diameter for 0.1 μm monodisperse suspensions over time at various initial particle concentrations.

In a non-ideal system, particles suspensions are never perfectly monodisperse. Polydisperse distributions are suspensions with a wide range of particle sizes, usually described mathematically using Equation 1.18.

$$N(d_p) = \frac{N_o}{\sqrt{2\pi}} \frac{1}{\ln(\sigma_g)} \frac{1}{d_p} \exp\left[- \frac{(\ln d_p - \ln \mathrm{CMD})^2}{2(\ln \sigma_g)^2} \right] \tag{1.18}$$

The number of particles of some size ($N(d_p)$) depends on the total initial concentration (N_o), the count median diameter (CMD), and the geometric standard deviation of the distribution (σ_g). In experimental settings, monodisperse particle suspensions are defined as a distribution with a geometric standard deviation (σ_g) less than 1.2.[16]

The coagulation coefficient for a polydisperse suspension can be calculated using the CMD as the d_p in Equation 1.10. If the number concentration decreases less than 8-fold over time, the coagulation coefficient calculated using the CMD will predict the change of a polydisperse particle concentration within 30%.[16]

A more accurate derivation for K within a polydisperse suspension begins with calculat-

ing the coagulation coefficient between two different sized particles ($K_{1,2}$, Equation 1.19).

$$K_{1,2} = \pi(d_1 D_1 + d_1 D_2 + d_2 D_2 + d_2 D_1) \tag{1.19}$$

$K_{1,2}$ depends on the diameter of each particle, d_1 and d_2, and the diffusion coefficient for each particle, D_1 and D_2. The summation of all coagulation coefficients for every particle size within a polydisperse distribution results in Equation 1.20, where K_{ij} is the coagulation coefficient between particles of ith and jth size, and f_i and f_j are the fractions of the total number of particles in the ith and jth intervals, respectively.

$$\overline{K} = \sum_{i=1}^{k} \sum_{j=1}^{k} K_{ij} f_i f_j \tag{1.20}$$

If $\overline{K}$ does not change appreciably over time, the value can be used in Equation 1.14. Lee and Lee and Chen developed an analytical solution for $\overline{K}$ for a polydisperse distribution when CMD $> \lambda_g$ (Equation 1.21), which corresponds to fine particles with diameters greater than ~0.066 μm in 1 atm air.[23,24]

$$\overline{K} = \frac{2k_b T}{3\eta}\left(1 + \exp(\ln^2 \sigma_g) + \frac{2.49\lambda_g}{\text{CMD}}[\exp(0.5 \ln^2 \sigma_g) + \exp(2.5 \ln^2 \sigma_g)]\right) \tag{1.21}$$

The analytical solution for coagulation of polydisperse suspensions provides the ability to predict how particle suspensions change over time. For example, a 70 nm monodisperse, spherical particle suspension in air with a number concentration of $1 \times 10^6/\text{cm}^3$ requires approximately 0.4 hours for the concentration to decrease by half. After ~2.3 hours, the particle size doubles ($N(t) = 0.125N_o$, $d_p(t) = 2d_o$). Similarly, a polydisperse suspension in air with the initial total number concentration of $1 \times 10^6/\text{cm}^3$, geometric standard deviation of 1.7, and an initial count median diameter of 70 nm requires approximately 0.2 hours for the total number concentration to decrease by half. Therefore, a polydisperse suspension coagulates faster than a monodisperse suspension under similar conditions, see Figure 1.5.

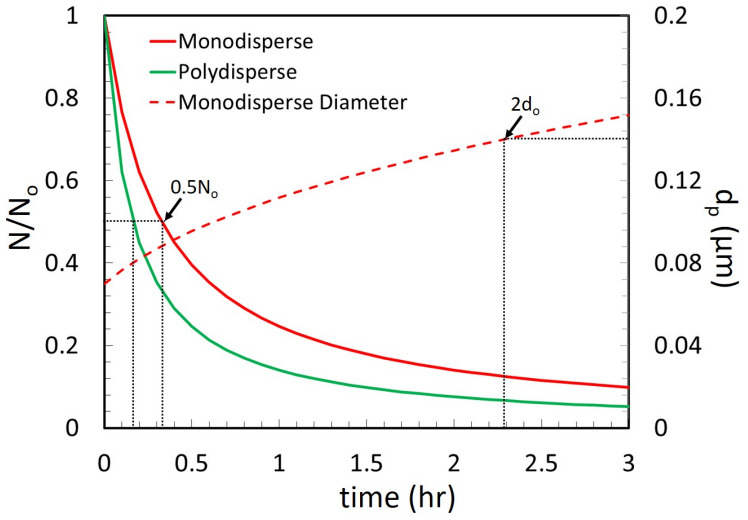

Figure 1.5: Calculated change in number concentration for 70 nm, $1 \times 10^6/\text{cm}^3$ monodisperse and polydisperse ($\sigma_g = 1.7$) suspensions after 3 hours. The secondary axis represents the increase in diameter for the monodisperse suspension due to coagulation.

Although Equation 1.21 provides a description for the coagulation of solid, spherical particles, particle shape and phase affect the rate of coagulation. For example, Zebel reported that ellipsoid particles enhance the coagulation coefficient ($\overline{K}$) by 35% when compared to spherical particles with the same volume.[25] Irregularly shaped particles have a larger collisional cross section than spherical particles. The collisional frequency in a particle suspension is proportional to the particle collisional surface area (Equation 1.7), which contributes to the enhanced coagulation coefficient of ellipsoids. As I explore different particle types, shapes and sizes, the derivation described in this section will provide a starting point for understanding the aerosol dynamics observed during experiments using the ACSI.

1.2.1.2. Particle Sources and Composition

Aerosols are either emitted directly into the atmosphere (primary) or formed by gas-to-particle conversion processes and reactions (secondary).[13] Primary particles eventually undergo chemical transformations while remaining in the particle phase to become secondary particles.[26] 'Secondary' indicates a gas-phase chemical reaction and a change of phase, i.e. gas-phase to either the liquid or solid-phase. Secondary aerosols consist of organic molecules

that have undergone chemical reactions resulting in a lower volatility compound before condensing or transferring to the particle phase.

Ultrafine particles usually enter the atmosphere as primary particles before secondary material condenses onto the particle surface.[17] Most fine particulate matter contains primary ultrafine particles that have undergone coagulation and condensation. Larger, coarse-mode particles are mostly primary particles from mechanical processes such as windblown dust and sea spray aerosols. Some coarse particles contain secondary material like sulfates or nitrates on the surface.[17]

Table 1.1: Estimated total yearly flux (Tg/yr) of particle mass from common sources. Table adapted from Reference 13.

Source	**Estimated flux (Tg/yr)**
Natural	
Primary	
Mineral dust, total	1490[27]
0.1–1.0 μm	48[27]
1.0–2.5 μm	260[27]
Sea salt	10,100[28]
Volcanic dust	30[29]
Secondary	
Sulfates from dimethyl sulfide (DMS)	12.4[30]
Sulfates from volcanic SO_2	20[29]
Organic aerosols from biogenic VOC	11.2[31]
Anthropogenic	
Primary	
Industrial dust	100[29]
Black carbon	12[32]
Organic carbon	81[32]
Secondary	
Sulfates from SO_2	48.6[30]
Nitrates from NO_x	21.3[33]

Particulate matter composition depends on the source. Section 1.2.1 established that $PM_{2.5}$ generally contains particles formed via gas-to-particle conversion processes and persists in the atmosphere for the longest amount of time compared to other sizes of particles. This section focuses on the sources and composition of fine and ultrafine particulate matter.

Table 1.1 lists the estimated yearly flux (Tg/yr) from common fine and ultrafine particle sources.[13]

Mineral or crustal dust is generally released into the atmosphere from wind storms in arid and semi-arid regions. For example, the Saharan desert alone introduces 250 Tg/yr of crustal dust into the atmosphere.[34] Dust storms affect the immediate area as well as surrounding regions due to long-range atmospheric particle transport.[17,35] Research studies have shown that enough dust originating from a Saharan dust storm travelled across the Atlantic ocean to reduce visibility on the eastern coast of Florida and South America.[36,37] Asian dust storms also contribute to mineral dust transport across the Pacific ocean. Figure 1.6 is satellite imagery from NASA's CALIPSO, which illustrates dust transport from the Saharan desert to South America. Dust particles involved in long-range transport (≥5000 km) consist of metal oxides indicative of the source material and are less than 10 μm in diameter.[17]

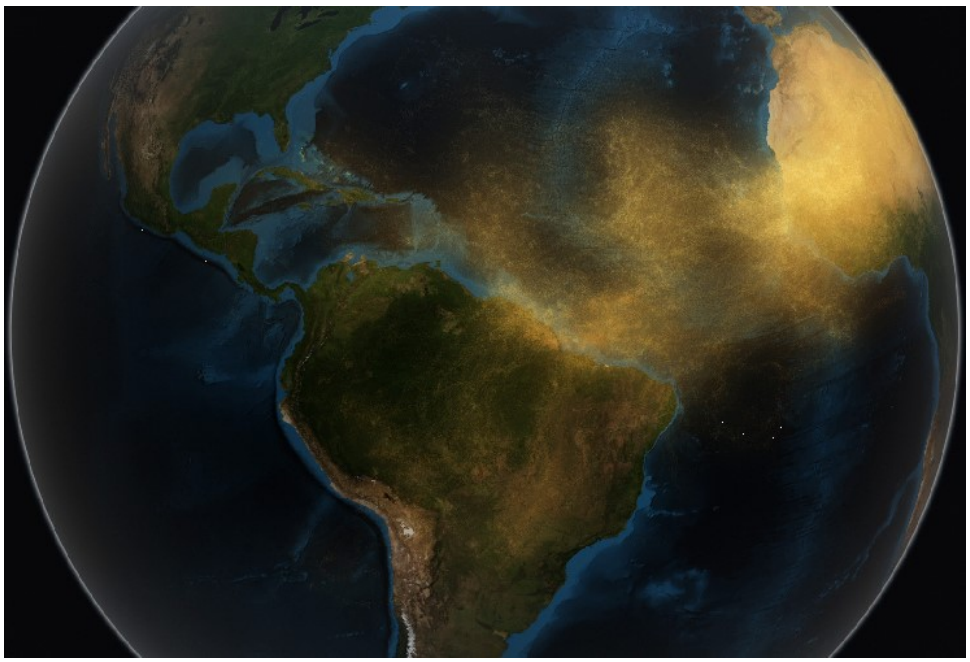

Figure 1.6: Satellite imagery from NASA's Goddard Space Flight Center CALIPSO illustrating dust transport from the Saharan desert to South America. The image is from Reference 37.

The most abundant metal oxide species in crustal dust include quartz, clay, calcite, gypsum and iron oxides.[17,38] Some secondary material, such as sulfates, nitrates, and organic molecules, condense on the surface of the mineral dust particles that persist in the atmosphere.[39–45] As mineral dust transmits over remote oceans, up to 70% of particle mass associated with crustal dust is internally mixed with sea salt aerosols, which results in particles approximately 1 μm in diameter.[46–48] Andreae et al. suggested that cloud processing and coagulation result in internally mixed particles, including mineral dust particles.[48] The mineral dust average mass concentration ranges from 0.05 to 0.5 $\mu g/m^3$, however, the mass concentration is occasionally higher and comparable to the average sea salt aerosol concentration during major continental dust events.[46,47,49,50]

Sea salt, also referred to as sea spray or marine aerosols, have the highest yearly flux into the atmosphere, over 10,000 Tg/yr[13,28] and typical number concentrations around 100–$300/cm^3$.[17,46,51] Each size mode defined in Section 1.2.1 is present in marine aerosols and are generated by different processes.[46] Agitation on the ocean surface due to wind and waves create bubbles that burst and evaporate to form the larger, coarse marine aerosols.[46,52] Larger marine particles consist mostly of NaCl and other natural substances found in the ocean.[46,52,53] Coarse mode sea salt aerosols represent ~95% of the total mass concentration but less than 10% of the total number concentration.

Fine and ultrafine marine aerosols amount to approximately 95% of the total number concentration and contain non-sea-salt sulfate (nss-sulfate) and sea salt.[46] Gas-to-particle conversion of sulfates in clouds form nss-sulfate ultrafine aerosols (<0.25 μm) found over the oceans.[46,54,55] Marine aerosols larger than ~0.3 μm mainly consist of sea salt similar to NaCl.[46,55] The concentration of nss-sulfate particles near coasts is nearly an order of magnitude higher than that over remote areas of the Pacific ocean.[46,56] Fitzgerald speculated that nss-sulfate particles found over remote oceans are the result of long-range transport from continental sources with small amounts of *in situ* formation over the ocean.[46]

Fine particles found over the ocean larger than 0.35 μm in diameter are more likely to

contain nitrate salts than nss-sulfate salts.[46,57–59] Remote regions of the ocean have 90% less nitrate-containing particles than coastal regions.[46,59] For example, 30–50% of the particles collected in the equatorial region of the Pacific ocean contained nitrate salts, whereas <5% of particles over latitude 60°S had nitrate present. The 60°S is unique because there is no land mass at this latitude, resulting in the most remote regions of the ocean. The higher concentration at equatorial regions indicate biogenically produced organic nitrogen from the ocean near land masses may be an important source for nitrate-containing particles.[46,59,60] Parungo et al. also reported that atmospheric NO_x (oxides of nitrogen) from the stratosphere or upper tropospheric lightning were not sufficient sources for the amount of nitrate salt found in marine aerosols.[59] Size differences between nss-sulfate particles and nitrate particles indicate the nitrate aerosols are not formed by homogeneous nucleation gas-to-particle conversion processes.[46] Instead, atmospheric NO_2 selectively dissolves into larger, more basic sea salt aerosols that persist in the atmosphere.[59] Common atmospheric gases, such as SO_2 and NO_2, will be discussed further in Section 1.2.2. Higher concentrations of nss-sulfate and nitrate particles near continental regions indicate anthropogenic sources of inorganic particulate matter affect the atmosphere on a global scale. Sulfate-containing particles contribute to heterogeneous chemistry explored in Chapter 4. See Section 1.2.3 for more information on atmospheric heterogeneous reactions.

Urban areas introduce over 100 Tg of anthropogenic aerosol material every year into the atmosphere.[13,29] Average mass concentration of urban aerosols (UA) ranges from 30-50 $\mu g/m^3$.[17] The main sources of UA include industrial processes, power generation, and transportation.[14,17] Particle concentrations near major roadways are 10–20% higher than the average urban aerosol concentrations. Transportation introduces particles via tire and brake wear, resuspension of various particles on the roadways from vehicle traffic,[61] and primary particles from combustion processes.[17] Coarse mode UA primarily consists of soil dust, sea salt, and brake and tire wear particles. Most UA, however, are Aitken mode particles, less than 0.1 μm in diameter. Accumulation mode particles form either from coagulation of

the Aitken mode, directly from combustion, or from gas-to-particle conversion processes involving sulfates, nitrates, elemental carbon, and organic carbon. Gases present in urban environments condense onto the larger, accumulation mode particles. Urban aerosols continue to age through vapor condensation and cloud processing as the particles transport to rural areas. Heintzenberg reported that the average concentration of fine particles in rural areas is only a factor of two lower than in urban areas.[14] However, the amount of highly oxidized organic material on the UA increases as the aerosols transport through the atmosphere to the rural and remote areas.[62] The ACSI set-up has the capability to analyze the individual effects of specific gases and model atmospheres on the lifetime of urban aerosols.

Carbonaceous particulate matter found in both anthropogenic and natural aerosols is characterized into two main categories: elemental carbon (EC) and organic carbon (OC).[26] EC exhibits molecular properties similar to graphite and OC encompasses hundreds of volatile organic compounds (VOCs) that include atoms other than carbon, such as hydrogen, oxygen, and nitrogen, and eventually partition onto particles.[62–65] Present research is focused on not just EC and OC found in particulate matter but the sources and formation pathways for the highly oxidized carbonaceous material found in SOA (secondary organic aerosols). Organic carbon (OC) can be either directly emitted as volatile organic compounds or evaporate off of primary organic aerosols such as diesel particulate matter,[62,64] which eventually oxidize and condense on pre-existing particles. Ambient VOCs consist of a complex mixture of organic compounds with up to 30+ carbons, including but not limited to n-alkanes, n-alkanoic acids, n-alkanals, aromatic and aliphatic polycarboxylic acids, polycyclic aromatic hydrocarbons, ketones, quinones, and N-containing compounds.[26,64,66–71] According to Robinson et al., less than 10% of the organics present in particulate matter and in the gas phase has been characterized in current atmospheric models.[64] The oxidation and condensation of gases evaporated off of primary particles or emitted directly into the atmosphere contributes up to 20–90% of the organic material in $PM_{2.5}$.[62] In urban areas, organic aerosol (OA) concentrations reach 10-80 $\mu g/m^3$, especially in heavily trafficked regions

like Beijing, China.[62,64] Aerosol science currently has a disconnect between results found from atmospheric monitoring studies and laboratory research on the origin of the organic fraction found on secondary aerosols. The ACSI provides the opportunity to explore and monitor the process of low- and semi-volatile organic molecules partitioning off of primary organic aerosols like diesel particulate matter, oxidizing in a model atmosphere, and then re-condensing onto the remaining aerosols.

Other gases, such as sulfur and nitrogen-containing gases, contribute to secondary inorganic aerosols. Sulfur- and nitrogen-containing molecules oxidize in the atmosphere to produce sulfates and nitrates, which form water-soluble inorganic particulate matter. Secondary inorganic matter either forms new particles or adsorbs to existing particulate matter, which increases the hygroscopicity of the water-insoluble particles like mineral dust.[72] The hygroscopicity of a particle, defined as the ability to adsorb or release water vapor, is directly related to the particle composition. Composition determines the effectiveness for conventional removal pathways, such as cloud processing. For example, the hygroscopicity of insoluble, fine mineral dust increases as sulfates and nitrates adsorb onto the surface, enhancing the ability for cloud droplets to scavenge and remove dust particles from the atmosphere.[72]

Natural sources introduce approximately 32.4 Tg of sulfur per year from dimethyl sulfide (DMS) and volcanic SO_2 that eventually form secondary sulfate aerosols.[13,29,30] Anthropogenic sources of sulfates and nitrates contribute 48.6 Tg(S) and 21.3 Tg(N) per year, respectively.[13,30,33] Section 1.2.2 provides detail about common atmospheric gas sources and related gas-phase chemical reactions. Secondary inorganic salt ions exist in most types and sizes of particles, especially near continental and urban areas.[14,39,40,46,48–51,60] Wall et al. found that ammonium, sulfate and nitrate ions have the largest concentrations in fine particles, between 0.3–1.2 μm in diameter, see Figure 1.7 for the size distribution of inorganic ions in particles.[38] The ammonium concentration in accumulation mode particles is high enough to chemically neutralize sulfuric acid and nitric acid.[73] Ultrafine particles do not contain enough ammonium to chemically neutralize the inorganic acids, which implies the

acidic sulfates are not fully available for neutralization potentially due to an organic coating around a sulfate core. Since fine inorganic salt particles also potentially act as a catalyst for heterogeneous chemistry involving VOCs,[74] I chose to explore the aerosol dynamics and heterogeneous chemistry of ammonium sulfate for the initial experiments using the ACSI.

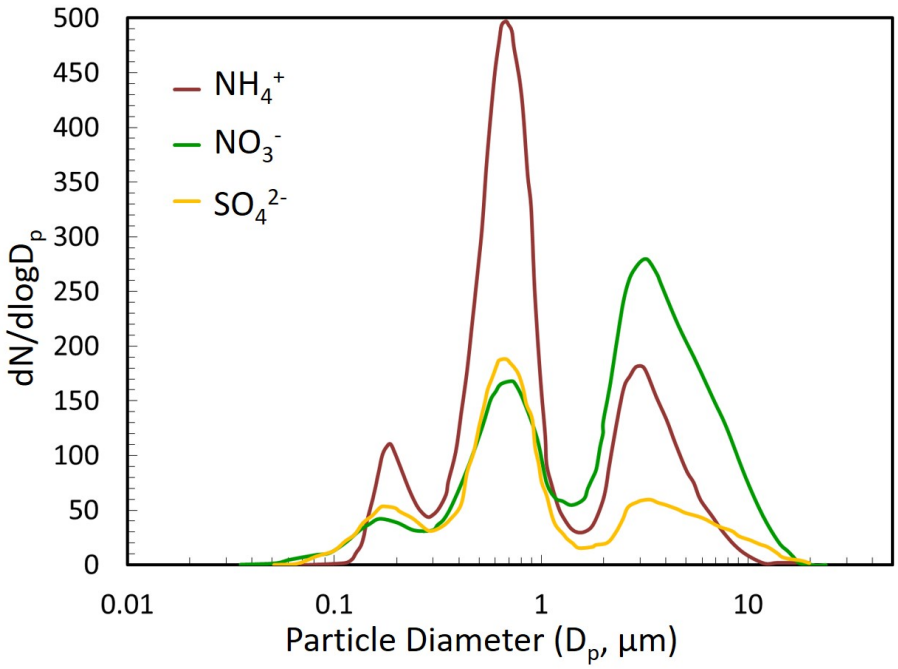

Figure 1.7: Size distribution of common inorganic salt ions. This figure adapted from Reference 38.

1.2.2. Atmospheric Gases

All types of particles, from nss-sulfate particles to urban and carbonaceous aerosols, interact with gases, vapors and other particles until removed from the atmosphere via deposition. The most abundant atmospheric gases are inert, such as molecular nitrogen. Reactive gases are generally present in trace quantities but have significant effects on particle composition through heterogeneous reactions and vapor condensation. Gases emitted directly from anthropogenic and natural sources undergo aging processes as well, which usually involves gas-phase oxidation. Aged gases either continue to react in the gas-phase or partition into the particle phase. This section details important reactions involving the most prominent gases in the atmosphere.

The most reactive gases in the atmosphere are oxidants, such as ozone, oxygen, and the hydroxyl radical. Ozone (O_3) exists throughout the troposphere (altitudes <10 km) and the stratosphere (altitudes 10–50 km) at various concentrations.[13] The stratosphere contains approximately 90% of the naturally occurring ozone between 20 and 30 km above the Earth's surface, also known as the ozone layer. Stratospheric ozone, referred to as 'good' ozone, absorbs UV radiation from the sun, protecting organisms from dangerous high energy light. Tropospheric 'bad' ozone, however, is harmful to humans and other organisms and contributes to urban particulate matter pollution through gas-phase oxidation reactions. Tropospheric O_3 concentrations have increased by 1.48%/yr between 1979 and 1992 in the Pacific S. America region.[75] Although ozone participates in oxidation reactions, ozone produces an even stronger oxidant, the hydroxyl radical, upon photolysis and reaction with water vapor.[76,77]

Tropical areas with high humidity produce the most hydroxyl radicals.[78] The hydroxyl radical production reaction is the only known gas-phase reaction that breaks the O−H bonds in water and is the only appreciable source for the radical in the atmosphere. Hydroxyl radicals react with virtually all atmospheric trace gases, including VOCs, sulfur-containing molecules, and nitrogen-containing molecules.

Volatile organic compounds (VOCs) released from both anthropogenic and natural sources oxidize in the atmosphere, which results in hundreds of different molecules that affect air quality and interact with particulate matter.[13] Alkanes and alkenes are the two most common types of atmospheric VOCs. Alkanes, fully saturated alkyl chains, undergo hydrogen abstraction by oxidants, such as the hydroxyl and nitrate radicals.[78]

Once an alkane reacts with a hydroxyl or nitrate radical, the molecule continues to oxidize to form a short chain carbonyl, such as formaldehyde (HCHO), or carbon dioxide (CO_2). Larger alkanes produce longer chain aldehydes that react or condense onto particulate matter. The simplest hydrocarbon, methane (CH_4), is the most abundant VOC and almost 600 Tg(C) of methane are emitted every year.[13] Twenty-two Tg(C)/yr are not readily removed

through sinks, resulting in an accumulation of methane in the atmosphere. The average concentration of methane has increased by a factor of two in the last 100 years.[79] Methane accumulated in the atmosphere eventually reacts with hydroxyl radicals to form formaldehyde. Formaldehyde, a known carcinogen,[13] remains in the atmosphere for approximately 3.5 hours. Hydroxyl radicals only abstract hydrogen atoms from VOCs with nonreactive single carbon-carbon bonds.

Instead of hydrogen abstraction, hydroxyl radicals add to the more reactive double bonds in unsaturated VOCs with alkene functional groups. Unsaturated alkenes account for approximately 10% of the nonmethane organic compounds in urban areas.[78,80,81] Most natural VOCs contain at least one double bond and originate from plants and organisms. Natural alkene concentrations depend strongly on the source organism and the time of year. The addition of the hydroxyl radical to double bonds permits the formation of aldehydes and could initiate isomerization between multiple VOCs to produce higher molecular weight, lower volatility, organic molecules. The increase in reactivity from double bonds drastically decreases the atmospheric lifetime of alkenes. The reactions mentioned in this section are only a few of the potential pathways for VOC oxidation and aging. Hundreds of different oxidized VOCs are produced from the aging process.[26] Aged, oxidized molecules are more likely to react with aerosols or partition onto the particle phase, forming secondary organic aerosol material.[26,82] The ACSI will elucidate how individual aged VOCs affect aerosol dynamics as the molecules react with and condense onto particles in model atmospheres.

Nitrogen-containing gases, including ammonia, alkyl amines and nitrogen oxides (NO_x), are another type of volatile compound present in the atmosphere. Approximately 57.6 Tg of nitrogen from ammonia are emitted each year.[13,83] Agriculture involving domesticated animals, fertilizers, and crops is the main source of ammonia, which accounts for an average of 37.4 Tg(N) per year.[1,13,84] Natural sources of nitrogen-containing VOCs include the ocean, undisturbed soils, wild animals and biomass burning. Amines remain in the atmosphere for an average of 10 days and are removed via adsorption to surfaces, such as water, soil and aerosols.

Concentrations are higher over source-rich regions and range from 0.1–10 ppb. Ammonia and alkyl amines are the most significant basic gases in the atmosphere. Dimethylamine, specifically, is the most abundant aliphatic amine found in ambient particulate matter,[85,86] in the gas-phase,[87] in fog water,[88] and in cloud water.[86] Youn et al. found that dimethylamine participates in new particle formation events because the aliphatic amine is less volatile and more basic than ammonia.[86] The lower volatile dimethylamine is basic enough to react with ammonium sulfate aerosols and displace ammonia, which partitions back into the gas-phase. Nitrate and sulfate salts are the most common secondary inorganic ions found in particles along with ammonium ions. Chapter 3 and Chapter 4 describes the aerosol dynamics and heterogeneous chemistry involving nitrogen-containing particles and gases.

Nitrates form in the atmosphere as NO_x molecules oxidize. NO_x is defined as nitrogen oxides including NO and NO_2. High temperature combustion of molecular nitrogen produces NO_x. Internal combustion engines used to emit much more NO_x before catalysts were added to the exhaust system in order to reduce the nitrogen oxides back to molecular nitrogen. For example, Houghton et al. reported 51.9 Tg(N) of NO_x is released each year, and fossil fuel combustion alone contributed 33 Tg(N).[79] NO_x concentrations range from 10–1000 ppb in polluted urban and suburban areas and less in rural and remote areas.[89] Previously mentioned oxidants, such as ozone or the hydroxyl radical, continue to oxidize nitrogen oxides until nitric acid (HNO_3) is formed. Nitrogen oxides and nitric acid adsorb onto existing aerosols, which affect the chemical and physical properties of the particle.[72,90–92] More of the common heterogeneous reactions occurring between atmospheric gases and particles will be explored in Section 1.2.3.

Similar to NO_x, sulfur dioxide (SO_2) leads to the formation of inorganic, water soluble, sulfate-containing aerosols. Oxidation reactions involving SO_2 and dimethyl sulfide (DMS) in clouds are the main sources of atmospheric sulfate. Approximately 98–120 Tg(S) of sulfur-containing VOCs are emitted per year from anthropogenic and natural sources, not including sea salt emissions.[13,93,94] Anthropogenic sources account for 75% of the total atmospheric

sulfur and 90% of the sulfur in the Northern Hemisphere.[13,94] The oxidation state of sulfur containing compounds dictates how readily the compound will react with hydroxyl radicals and other atmospheric oxidants. Sulfur oxidation states range from the most reduced, -2, to the most oxidized, +6.[13] Table 1.2 lists the most abundant sulfur-containing compounds with the respective sulfur oxidation states, yearly emissions, atmospheric lifetimes, and common phase state. As sulfur compounds oxidize, the molecules partition to the particle phase, forming aerosols like ammonium sulfate.[13] Gas-to-particle conversion processes involving sulfates generate ultrafine and fine particulate matter.[46] Most of the fine particulate matter contains non-sea-salt sulfate and represents approximately 95% of the total particle number concentration in the atmosphere.

Table 1.2: Common sulfur-containing compounds in the atmosphere and the total yearly flux (i.e. from fossil fuels, oceans, etc.), sulfur oxidation state, average atmospheric lifetime, and usual phase state found in the atmosphere.[13,94]

Compound	**Total Yearly Emissions (Tg(S))**	**Oxidation state**	**Atmospheric Lifetime**	**Usual Atmospheric Phase State**
Dimethyl sulfide (DMS, CH_3SCH_3)	17–27	−2	0.5 days	gas
Sulfur dioxide (SO_2)	79–80	+4	2 days	gas
Sulfate ion (SO_4^{2-})	6–10	+6	5 days	aqueous, aerosol

Most gases emitted into the atmosphere react with oxidants such as the hydroxyl radical, and eventually interact with existing particles. Particles participate in heterogeneous reactions in a variety of ways including organic reaction catalysis,[74] reactive molecule removal processes,[95–98] secondary organic matter accumulation on existing aerosols,[72,90] and the release of gases back into the gas-phase.[1,99,100] The ACSI is capable of being modified to accommodate oxidative model atmospheres. The initial experiments described in Chapter 4 demonstrate the ability of the ACSI to monitor heterogeneous reactions between nitrogen-

containing gases and inorganic salt particles.

1.2.3. Heterogeneous Reactions in the Atmosphere

Fine particles ($PM_{2.5}$) persist for days to weeks in the atmosphere, as explained in Section 1.2.1. Longer suspension durations allow for heterogeneous reactions, vapor condensation onto the particle surface, and cloud process, all of which alter the surface and potentially the aerosol bulk properties as well. The term "aerosol aging" encompasses all types of reactions and changes a particle sustains while suspended in the atmosphere. Changes in aerosol composition alter how a particle interacts with the surrounding environment. For example, Kelly et al. reported that soluble nitrates and sulfates adsorbed to existing particles increases the ability of the particle to adsorb water, effectively increasing the likelihood that the particle will participate in cloud processing.[72] In other instances, heterogeneous reactions result in dissolved gases or particle-phase molecules to partition back into the gas-phase.[99] Previous experiments exploring atmospherically-relevant heterogeneous reactions involve highly controlled, short duration, gas-phase experiments,[10] reactions occurring in solution,[74] or reactions on a fixed particle bed.[90,101,102] The ACSI was created to monitor gas-phase changes due to reactions between stable fine particle suspensions and pollutant gases. Chapter 4 provides more detail on the initial heterogeneous reactions studied using the new instrumentation and experimental approach.

Metal oxides represent components of crustal dust originating from arid and semi-arid regions and react with existing gases. For example, nitric acid irreversibly and dissociatively adsorbs to most metal oxides.[90] When Goodman et al. increased the relative humidity within the experimental chamber, the nitric acid reacted faster with metal oxides, like alumina and calcium oxide.[90] Furthermore, a layer of nitric acid solution formed and remained on the surface of alumina, while nitric acid reacted throughout the bulk of calcium oxide under high humidity.[90,91] Similar to nitric acid, nitrates also adsorb to mineral oxide surfaces.[92] Fairlie et al. found that particulate nitrate is associated with mineral dust while particulate sulfate is more commonly associated with ammonium ions.[92] Nitrate adsorption onto mineral dust

potentially acts as an atmospheric sink for NO_x and increase the cloud processing potential of insoluble, metal oxide particles.[72,95–97]

Metal oxides found in mineral dust also react with volatile organic compounds in the atmosphere. For example, several research groups found that isopropanol reacts on metal oxide simulants that mimic natural mineral dust.[103–105] Romanías et al. performed a similar experiment and reported adsorbed isopropanol photochemically reacted with natural Gobi desert dust.[98] Competition for similar adsorption sites between isopropanol and water resulted in a decrease in isopropanol uptake as humidity increased. Once the adsorbed isopropanol reached a steady-state concentration, the exposed Gobi dust sample was irradiated with UV light and a mass spectrometer detected gas-phase products that included: acetone, formaldehyde, and acetic acid. Other produces bound to the surface were analyzed via liquid chromatography and included: hydroxyacetone, formaldehyde, acetaldehyde, acetone and methylglyoxal. The reaction occurred under both dry and humid conditions. Romanías et al. predicted that Gobi dust can potentially deplete up to 38% of the isopropanol in dust storm conditions and then go on to form oxidized VOCs as the particles transport to regions with >50% RH.[98] Majority of the experiments involving metal oxides or mineral dusts utilize non-atmospheric reaction conditions, such as a fixed particle bed or a flow tube reactor. The ACSI is set up to detect the gas-phase products from similar reactions on particles suspended in a model atmosphere *in situ*. Future researchers can easily add a light source to the ACSI to explore photochemical heterogeneous reactions.

Inorganic, soluble salts catalyze organic reactions, such as aldol condensation reactions, that are commonly known to require strong acid or base catalysts to yield appreciable amounts of products.[74] Established in Sections 1.2.1 and 1.2.1.2, inorganic salts, such as ammonium sulfate or ammonium carbonate, are generally found in fine particulate matter and persist in the atmosphere for an average of 4–5 days. Glyoxal aldol condensation reaction products are known to exist in the atmosphere and Nozière et al. suggested that the ammonium and carbonate ions in aerosols catalyze the reaction.[74] Acetaldehyde and

acetone formed aldol condensation products in an ammonium carbonate solution, similar to the aldol condensation reaction catalyzed by concentrated sulfuric acid.[74] Over 95% of the acetaldehyde converted into the olefinic aldol products in a solution containing ammonium ions. Aldol condensation reactions produce linear, conjugated, carbonyl compounds that remain on the particle rather than partitioning back into the gas-phase, which could lead to an increase in secondary organic material on aerosols. Though inorganic salt aerosols act as catalysts in organic reactions, the ions also contribute to acid-base reactions in the atmosphere.

Atmospheric acid-base reactions generally involve sulfuric acid and some type of basic amine or ammonia. Most commonly, ammonia gas neutralizes sulfuric acid to form ammonium sulfate salt. Other types of alkyl amines, such as monomethyl or dimethyl amine, also participate in acid-base reactions. Tao et al. detected alkyl aminium salts in Aitken and accumulation mode atmospheric particles as a result of alkyl amine gases participating in chemical neutralization reactions.[1] Another study collected particle samples and reported that particles containing dimethylamine had a peak mass concentration between 0.18 and 0.56 μm, which is an identical peak mass concentration to particles containing ammonium and sulfate ions.[86] Similarly, nitrate-containing particles exhibited a peak mass concentration larger than sulfates. The peak mass concentration trends of particles containing aminium, sulfate, and nitrate ions indicate that basic amines preferentially neutralize sulfates over nitrates.

Alkyl amines involved in atmospheric, heterogeneous acid-base reactions are stronger bases compared to ammonia. The alkyl amines react readily with sulfuric acid to form aminium sulfate particles during new particle formation events.[1,106,107] You et al. compared the ratios of the recorded gas-phase concentration of ammonia and a short chain amine to the corresponding particle ammonium and aminium concentrations.[106] Over half of the ammonia molecules remained in the gas-phase while only 0.8–1.2% of the short chain alkyl amines remained in gas-phase when compared to the corresponding ion concentration in

the collected particles. Since alkyl amines are stronger bases than ammonia, alkyl amines also react with existing ammonium sulfate particles, causing ammonia to partition back into the gas-phase.[99,100] Basic alkyl amines that react with acidic particles[108,109] and oxidants such as ozone, hydroxyl radicals and nitrate radicals[110] could contribute to higher secondary organic material incorporated into inorganic salt particles.[86] The ACSI was designed to elucidate the effect reactive gases have on the atmospheric lifetimes and aging processes of atmospherically-relevant particles.

To summarize, different types of particles participate in reactions involving pollutant gases. For example, nitrates affect the hygroscopicity of metal oxides,[72] inorganic salt particles catalyze organic reactions,[74] and acid-base reactions cause gases to partition back into the gas-phase.[99,100] Fine particles also experience many different types of environments due to long-range transport and extended atmospheric lifetimes. The new ASCI will provide insight into the effect of particle phase, particle composition, and heterogeneous chemistry on aerosol coagulation dynamics. Fundamental information of gas-particle interactions discovered with ASCI will contribute to existing atmospheric and computational models.

1.3. Instrument Design and Overview

After identifying remaining key scientific questions and current experimental limitations for laboratory-based research studies, I compiled a detailed list of design criteria (Table 2.1) that influenced the final design of the Atmospheric Cloud Simulation Instrument. The two main demands for studying atmospheric aerosols in a laboratory include:

1. A technique for suspending the fine particulate matter for long durations to simulate transport, aging, and fate of atmospheric particles.

2. A method for monitoring the gas-phase composition within the reaction chamber during controlled particle aging processes.

My design approach incorporated a rotating main chamber to maintain a stable particle suspension with cavity ring-down spectroscopy to monitor the gas-phase. Employing a

rotating cylindrical main chamber increases the drag force, which negates the gravitational force acting on the suspended particles, thus increasing the effective particle suspension duration.[111–114] Mid-infrared cavity ring-down spectroscopy (CRDS) interrogates the gas composition within the chamber. CRDS, a multi-pass spectroscopic technique, allows for effective sample path lengths up to 1000 meters.[115] This technique is commonly used in gas-phase infrared spectroscopy.[115–118] The CRDS incorporated into the ACSI employs a mid-infrared spectral window (860–1010 cm^{-1}) to decrease interference from $PM_{2.5}$ within the chamber and to detect unique spectral features from most VOCs of interest. The particle suspension characteristics in a rotating chamber and cavity ring-down spectroscopy are described in more detail in Chapter 2. Figure 1.8 shows an assembly drawing of the ACSI main chamber. Other design elements will be discussed in more detail in Chapter 2.

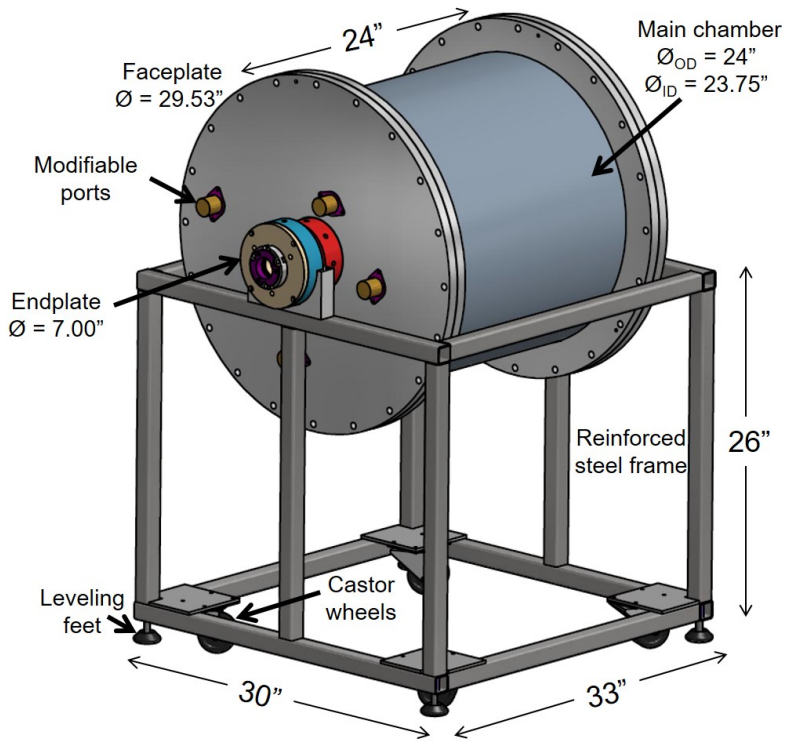

Figure 1.8: Assembly drawing of the Atmospheric Cloud Simulation Instrument. The height of the stand was determined to match the height of the cavity ring-down spectrometer optics table (not shown here). Leveling feet were used to reduce vibrations, align the CRDS, and raise the stand so it did not rest on the castor wheels. The motor, belt, gas lines and gas-handling manifold omitted for clarity.

1.4. Summary and Overview of Thesis

Atmospheric heterogeneous chemistry research requires precise control over the gas and aerosol composition in model atmospheres. I addressed these issues by designing and testing a novel system with a rotating main chamber, which provided the capability to suspend any type of particle or aerosol desired, whether it is a liquid droplet, dry metal oxide, atomized salt particle or even secondary organic aerosol.[111–113] I incorporated humidity control into the design of the ACSI as well as the capability to control the gas environment within the chamber to mimic most atmospheric conditions. The instrument design affords the possibility to modify the chamber to accommodate future atmospheric aerosol research. The following chapters describe the design process, benchmark testing, and the first heterogeneous chemistry system explored using the Atmospheric Cloud Simulation Instrument.

Chapter 2

Experimental Approach for Aerosol Studies

2.1. Introduction

The atmosphere contains a complex mixture of particulate matter and gases. Gases interacting and reacting with particulate matter alter the surface and bulk particle composition over the course of the particle atmospheric lifetime. In order to understand the heterogeneous reactions occurring in the environment, I needed to develop a strategy to mimic typical atmospheric conditions. The experimental approach needed to be able suspend particles on atmospherically-relevant time scales depending on particle size. For example, larger, coarse particles ($d_p > 2.5$ μm) generally deposit within a few hours after emission[12] while fine particulate matter ($PM_{2.5}$, $0.1 < d_p < 2.5$ μm) remains in the atmosphere for days to weeks,[13] as explained in Section 1.2.1.

Fine particles encounter many different atmospheric compositions ranging from dry, unpolluted, remote deserts to humid, coastal cities during long-range transport and extended atmospheric lifetimes compared to other sized particles. Model atmospheres in the ACSI need to be able to contain various volatile organic compounds (VOCs), like amines, that simulate pollutants and age or alter fine particulate matter suspensions. A decrease in the initial analyte pollutant gas concentration, a chemical change of the analyte induced by interactions with the particulate matter, or even the evolution of a different gas altogether from the particle surface constitute the potential gas composition changes due to heterogeneous reactions.[74,98,99] The instrument needed to be able to the track gas-phase composition *in situ* and as well as any changes in particle size distributions over the course of an experiment.

Previous research studies employed other techniques for exploring atmospheric reactions, which included short duration, gas-phase experiments,[10] solution-based reactions,[74] or reactions on a fixed particle bed.[90,101,102] Our goal was to develop an instrument and ex-

perimental approach to bridge the gap between direct environmental monitoring research and previous fundamental studies conducted under non-atmospheric conditions. The new Atmospheric Cloud Simulation Instrument (ACSI) utilizes cavity ring-down spectroscopy to monitor gas-phase composition and a rotating main chamber to establish stable fine particle suspensions.

The unique rotating chamber feature provides the capability to suspend and investigate interesting chemistry for any type of particle or aerosol desired, whether it is a liquid or oil droplet, dry metal oxide, atomized salt particle or secondary organic aerosol.[111–113] Cavity ring-down spectroscopy is a highly sensitive spectroscopic technique incorporated into the central axis of the rotating chamber that allows for the detection of trace gas concentrations nearing the parts per billion (ppb) level. I also included humidity control into the ACSI design as well as the capability to control the gas environment within the chamber to mimic most atmospheric conditions. In addition to current experimental requirements, the instrument design affords the possibility to modify the chamber for future atmospheric aerosol research projects. The following sections describe the design considerations, computational model, benchmark testing, and the first heterogeneous chemistry systems explored using the Atmospheric Cloud Simulation Instrument.

2.2. Design Criteria

Atmospheric heterogeneous chemistry research requires precise control of various experimental parameters such as humidity, gas composition, aerosol material, etc. The ACSI was specifically designed to simulate atmospheric conditions by creating a stable particle suspension utilizing a rotating cylindrical chamber while exploring the changes in gas and aerosol composition during the aging process with cavity ring-down spectroscopy. Longer suspension durations allow for heterogeneous reactions or vapor condensation to occur, which alter the surface and potentially the aerosol bulk material as well. Experimental criteria and the corresponding design solutions, listed in Table 2.1, enable complete experimental control as well

as adaptability for future research requirements. Figure 2.1 revisited is the general assembly drawing for the chamber design after all of the criteria listed in Table 2.1 were addressed. Future experiments using the ACSI will provide insight into changes in aerosol dynamics from heterogeneous reactions help understand our complex atmosphere.

Table 2.1: List of experimental criteria necessary for heterogeneous aerosol chemistry studies and the respective design approach for the ACSI.

Experiment Criteria	**Design Approach**
Long term particle suspension durations	Rotating Chamber
Monitor gas phase species	Cavity ring-down spectroscopy
Analyte introduction and minimal particle interaction with spectroscopic mirrors	6 in diameter stationary tube extensions
Aerosol introduction directly into the chamber	Unique aerosol pathway and ports
Ability to alter and continuously monitor chamber humidity	MFC-controlled humidity introduction and relative humidity and temperature probe
Adaptable to future research requirements such as photochemistry or particle collection	8 modifiable ports on the main chamber

2.2.1. Particle Suspension

Natural and anthropogenic aerosols persist in the atmosphere for different lengths of time depending on particle size and composition. Fine particulate matter ($PM_{2.5}$) remain in the atmosphere for up to weeks and consist of mineral dust, sea-spray aerosols, secondary inorganic salts, etc. See Section 1.2.1.2 for more information on the composition and lifetimes of atmospheric particulate matter. Particles can travel over thousands of kilometers[17,35,36] and experience a variety of different types of environments, such as various humidities, higher concentration of pollutants and other pre-existing particles. For example, wind storms in Africa introduce mineral dust particles into the atmosphere that transport through regions of low humidity (<30% RH), high humidity (>70% RH), high concentrations of sea-spray aerosols, and eventually urban environments over Florida.[36] Aerosol aging processes, including coag-

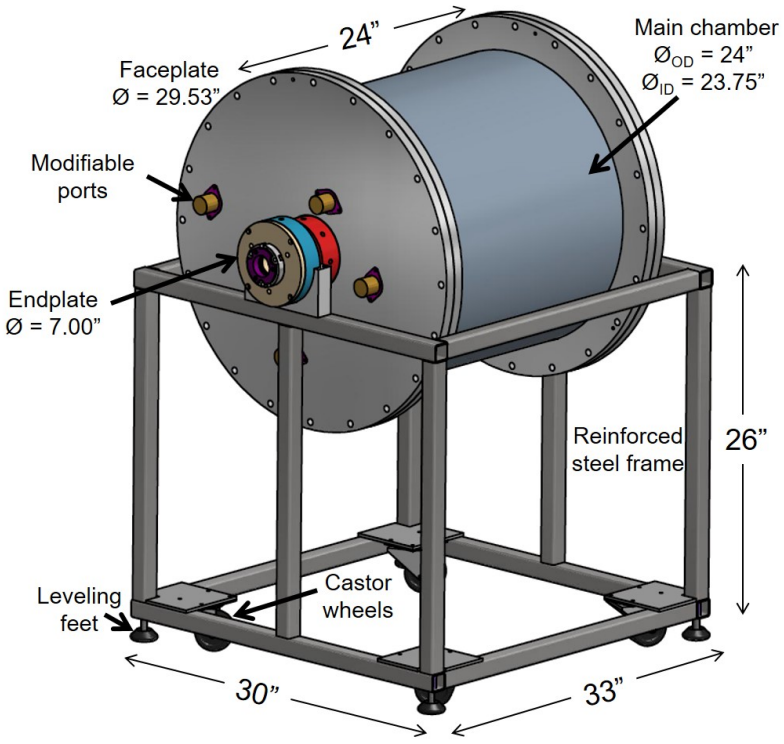

Figure 2.1: Assembly drawing of the Atmospheric Cloud Simulation Instrument. The height of the stand was determined to match the height of the cavity ring-down spectrometer optics table (not shown here). Leveling feet were used to reduce vibrations, align the CRDS, and raise the stand so it did not rest on the castor wheels. The motor, belt, gas lines and the gas-handling manifold omitted for clarity.

ulation, vapor condensation, and cloud processing, alter particle size and composition. In order to understand how these environments and aerosol aging processes affect atmospheric aerosol lifetime, I developed a chamber to suspend any type of $PM_{2.5}$ for hours to days and in any model atmosphere.

Aerosol suspensions in experimental settings are affected by a variety of phenomena including electrostatic forces, pressure and concentration gradients, inter-particle collisions, gravity, and viscous drag from surrounding gas molecules.[112,113,119] Mathematical models that support the use of a rotating cylindrical chamber to extend particle suspension durations only considered gravitational and viscous forces and assumed other forces were negligible under normal conditions. Two mathematical models for particle suspensions in rotating chambers were developed by Gruel et al. and Asgharian and Moss.[112,113] The Gruel et al.

model predicted the particle suspension efficiency in a chamber rotating between 0.1–10 RPM, however the model did not converge with gravitational settling as the rotating speed approached 0 RPM.[112] Asgharian and Moss revised the model and applied the method of limiting trajectories to account for transient particle loss in a chamber rotating less than 1×10^{-3} RPM.[113] The two approaches resulted in similar optimal rotation speeds but predicted different suspension efficiencies. Our collaborators at Clarkson University expanded on the two previous models and developed a method to account for the particles re-entering the particle field in the Asgharian and Moss model.[113,114] The new Brown and Dhaniyala model converged with the Gruel et al. model for fine particulate matter suspended in a chamber rotating at a moderate speed (0.5–5 RPM), which also encompasses optimal rotating speeds for $PM_{2.5}$.[112,114] The following computational model outlines the Gruel et al. model applied the initial, moderate rotating speed experiments in Chapter 3.[112] For more information on the Brown and Dhaniyala model, see Appendix Section A.1.1.[114]

Gruel et al. predicted the fraction of particles remaining in a suspension due to the combination of centrifugal force acting on the particles (Equation 2.1) and gravitational settling (Equation 2.2).[112]

$$\left.\frac{N}{N_0}\right|_{\text{rot}} = \exp(-2\tau\omega^2 t) \tag{2.1}$$

The particle suspension efficiency is defined as N/N_0, where N is the number of particles at time t, and N_0 is the initial particle concentration, ω is defined as angular velocity in radians per second (determined by the chamber rotation speed), and τ is particle relaxation time or particle time constant, defined in Equation 1.6. The particle relaxation time depends on the particle density (ρ_p), particle diameter (d_p), the Cunningham correction factor (C_c, Equation A.2),[16] and the dynamic gas viscosity (η, Equation A.1). The rate of particle loss due only to centrifugal forces, Equation 2.1, increases as the chamber rotation speed increases and is independent of chamber size.

Particle loss due to gravity depends on the particle time constant and chamber rotation rate relative to the chamber radius. Particle suspension efficiency is defined as the area of particle concentration normalized to the chamber area (Equation 2.2). The point where terminal settling velocity of the particle is equal and opposite in magnitude to the chamber tangential velocity determines the radius of the particle area (r_0, Equation 2.3).

$$\left.\frac{N}{N_0}\right|_{\text{grav}} = \frac{(R - r_0)^2}{R^2} \tag{2.2}$$

$$r_0 = \frac{\tau g}{\omega} \tag{2.3}$$

Gruel et al. assumed a steady state particle concentration loss due to gravity,[112] therefore the total rate of particle loss in a rotating chamber is the product of Equation 2.1 and Equation 2.2 resulting in Equation 2.4.

$$\left.\frac{N}{N_0}\right|_{\text{total}} = \frac{(R - r_0)^2}{R^2} \exp(-2\tau\omega^2 t) \tag{2.4}$$

The new model from Brown and Dhaniyala converges to the gravitational settling rate of the particles when chamber rotation speed approaches zero and converges with the Gruel et al. model when $\omega t/2\pi > 1$.[112,114] Therefore, Equation 2.4 is used determine the optimal rotational speed and depends on the diameter and density of the particles under investigation. Figure 2.2 compares the modeled particle suspension efficiency for a variety of particle sizes (0.5 μm to 20 μm) versus chamber rotation rate after 8 hours using the models from Asgharian and Moss, Gruel et al., and Brown and Dhaniyala.[112–114]

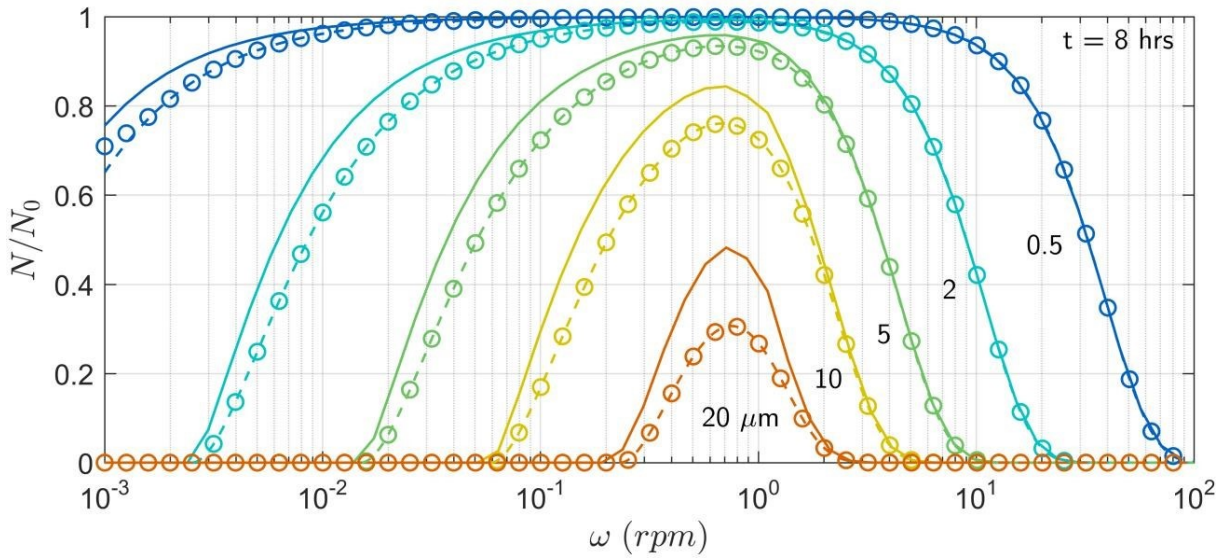

Figure 2.2: Computational models from Asgharian and Moss (solid)[113] Gruel et al. (dashed)[112] and Brown and Dhaniyala (o)[114] models for particle suspension efficiency (N/N_o) as a function of chamber rotation rate for multiple particle sizes and a test duration of 8 hrs. This figure is from Reference 114.

Fine particles ($PM_{2.5}$), which remain suspended in the atmosphere for the longest amount of time, do not remain suspended in an extremely slow rotating ($<1 \times 10^{-3}$) or stationary chamber according to the models due to the gravitational force. Similarly, if the chamber rotates at speeds over 5 RPM, the centrifugal force acting on the particles would overcome the gravitational force, causing particles to deposit on the walls of the chamber. However, the computational model predicts 80–100% of the $PM_{2.5}$ will remain suspended after 8 hours in a chamber rotating between 0.5 and 2 RPM. The peak N/N_o fraction determines the optimal rotation speed for that diameter particle. The desired atmospheric studies involve a range of particle sizes that may change over time due to aging processes, therefore rotational speeds between 1–2 RPM should result in the highest particle suspension efficiencies for polydisperse particles used in the preliminary studies. Using the models described above, I decided that a rotating aerosol chamber would extend particle suspension durations to perform the necessary experiments to explore heterogeneous reactions involving fine particulate matter over the course of several hours or days.

2.2.2. Cavity Ring-down Spectroscopy

The atmosphere contains a complex mixture of natural and anthropogenic pollutant gases, including sulfur-containing compounds, nitrogen oxides (NO_x), volatile organic compounds (VOCs), and toxic industrial compounds (TICs). Gas-phase contaminants either originate with reactive functional groups, like natural alkenes, or undergo oxidation that produces complex and reactive compounds, like aldehydes or other carbonyl functional groups.[26,66–71] For more information on gases in the atmosphere, see Section 1.2.2. Such complex mixtures make understanding the individual interactions between a specific gas and type of particle difficult. For example, a simple system involving one type gaseous amine and an ammonium sulfate particle suspension will introduce a trace amount of ammonia gas into the model atmosphere.[99,100,120] One of the objectives of the ACSI is to provide more fundamental insight into observed reactions from environmental monitoring studies by precise control of the model atmospheres.

Interfacial chemistry and subsequent release of surface adsorbates into the model atmosphere can be characterized using a type of infrared spectroscopy. Common heterogeneous atmospheric reactions involve trace amounts of gases that fall below the limits of detection for many conventional, non-destructive gas detection methods. For example, ammonia is known to react with sulfuric acid and sulfates and has ambient concentrations below ~10 ppb.[99,106] Typical instrumental techniques capable of detecting gases on the ppb scale generally include gas chromatography or mass spectrometry. Both approaches require *ex situ* sample analysis and destroy the sample gas. A spectroscopic method incorporated into the instrument provided the ability to analyze the gas-phase composition without disturbing the model atmosphere. The design constraints of the ACSI required a spectroscopic technique that could detect molecules of interest at trace levels with a ~1 m long, fixed path length. A traditional single pass technique would not have the sensitivity necessary for atmospherically-relevant concentrations, such as ~10 ppb for ammonia. Cavity ring-down spectroscopy increases the absorption sensitivity proportional to the effective path length, which is increased with every

pass or round-trip the light makes through the sample chamber.

According to Beer's Law (equation 2.5), absorbance ($A(\nu)$) is proportional to path length (d), therefore, a longer path length increases the absorbance for a given trace gas concentration (N). The ACSI CRDS increases the effective path length of the sample cell from an actual length of 1 m to ~1000 m, thus, the sensitivity will increase by three orders of magnitude.

$$A(\nu) = \sigma(\nu)Nd \tag{2.5}$$

The unique multi-pass feature of cavity ring-down spectroscopy employs pulsed laser light injected into an optical cavity formed by a pair of highly reflective mirrors. The intensity of each pulse of light exponentially decays with every pass or round-trip through the optical cavity. Light intensity decreases over time due to losses within the chamber, which include mirror surface imperfections, transmission through the mirrors, and the absorbing media in the model atmosphere. The spectrometer records the exponential decay of light intensity for every pulse of light while stepping through the spectral window at a given wavenumber interval, which results in an infrared spectrum. Equation 2.6 describes the exponential decrease of light intensity over time with one absorbing medium present in the optical cavity.[115,121,122]

$$\frac{I(\nu,t)}{I_o(\nu)} = \exp\left(\frac{-tc}{L}(\ln R(\nu) - \sigma(\nu)Nd)\right) \tag{2.6}$$

$I(\nu,t)$ is the intensity of light at a specific frequency (ν) as a function of time, $I_o(\nu)$ is the initial light intensity after one pass through the optical cavity, t is time in microseconds, c is the speed of light in cm/μs, L is the physical distance between the highly reflective mirrors, $R(\nu)$ is the reflectivity of the mirrors at that frequency, $\sigma(\nu)$ is the frequency-dependent absorption cross section for one absorbing medium, N is the number density or concentration of the absorbing medium, and d is the effective optical path length. The intensity of the light exponentially decreases without any absorbing medium present due to the transmission of a small amount of light ($T = 1 - R$) through the mirrors with each pass.

Frequency-dependent absorbance due to one absorbing medium ($\sigma(\nu)Nd$) is computed from each exponential decay using Equations 2.7 and 2.8. The reciprocal of the exponential decay constant (k) is the characteristic "ring-down time" ($\tau(\nu)$). Equation 2.7 describes the relationship between the intensity of light over time ($I(\nu,t)/I_o(\nu)$), $\tau(\nu)$, mirror reflectivity ($R(\nu)$) and absorbance ($\sigma(\nu)d$). When the chamber contains no absorbing medium, the reflectivity of the mirrors dictates the initial ring-down time, $\tau_o(\nu)$.

$$\frac{I(\nu,t)}{I_o(\nu)} = \exp(-kt) \text{ where } \frac{1}{k} = \tau(\nu) = \frac{L}{c(1-R(\nu)+\sigma(\nu)Nd)} \tag{2.7}$$

Once $\tau_o(\nu)$ and $\tau(\nu)$ are obtained, equation 2.8 is used to calculate absorbance due to the absorbing medium ($\sigma(\nu)d$).

$$\frac{(\tau_o(\nu)-\tau(\nu))}{\tau_o(\nu)\tau(\nu)}\frac{L}{c} = \sigma(\nu)Nd \tag{2.8}$$

Atmospheric reactions rarely involve a single absorbing species. Therefore, we need to separate the total absorbance due to different species into the absorbance due to each component in a gas mixture. According Beer's Law, individual components in a mixture additively absorb light and scale linearly with the concentration of each absorbing medium (equation 2.9). Thus, the spectrum for a specific absorbing medium may be isolated through subtracting known or control absorbance spectra after extracting the necessary information from the ring-down time.

$$A(\nu) = \sigma_1(\nu)N_1d + \sigma_2(\nu)N_2d + \ldots \sum_{i=1}^{n}\sigma_i(\nu)N_id \tag{2.9}$$

The CRDS theory outlined in this section supports the experimental approach that combined a rotating chamber to elongate particles suspension duration and a cavity ring-down spectrometer for monitoring small changes in gas composition within the chamber. Section 2.2.1 and Section 2.2.2 will serve as the basis for understanding and explaining the heterogeneous chemistry observed in the ACSI as I begin to explore different model

atmospheres containing various particles, gases, and different relative humidities. The final design addresses all of the criteria listed in Table 2.1 and detailed construction information is described in Section 2.3.

2.3. Chamber Construction

Every atmospheric research project requires a unique experimental approach in order to effectively study the desired chemistry. For example, a study monitoring gas evolution from a gas-particle reaction needs the ability to sustain a particle suspension, perturb and control the model atmosphere, monitor changes in the gas composition, as well as adequately clean the reaction chamber between experiments. Table 2.2 lists experimental approaches the ACSI employed to address requirements necessary to conduct atmospheric chemistry research with a rotating aerosol suspension chamber.

Table 2.2: Experimental requirements for a generic atmospheric study and our approach with the ACSI. Each topic will be discussed further in the following sections.

	Experimental Requirement	Approach
1.	Rotate the main chamber and maintain continuous access to ports and optics.	Chamber rests on double-wall ball bearings around the axles for smooth rotation and fixed tubes provide a location for stationary ports and optical mounts.
2.	Minimize particle loss throughout the experimental procedure.	Shortest possible, dedicated, stainless steel tube pathway allows for introduction of aerosols directly into the main chamber.
3.	Generate a model atmosphere with different gases through individual introduction pathways.	Five male VCR ports welded onto both fixed tubes allows for up to ten gas introduction pathways.
4.	Produce different types of salt aerosols, solid particles, or liquid droplets in a controlled manner.	Generate the aerosols from solution and remove residual aerosol water with a diffusion dryer along the aerosol introduction path.
5.	Monitor and control the humidity within the chamber without introducing water droplets or condensation.	Bubble nitrogen gas through two water reservoirs and an empty container then into the chamber while spectroscopically monitoring for condensation on the CRDS mirrors. A probe continuously monitors the humidity.
6.	Remove gases, particles and humidity and maintain a clean chamber between experiments.	One port on the fixed tube connected via a valve and filter to a vacuum scroll pump for chamber evacuation. Valve remains open to the pump between experiments.

The ACSI design employed a rotating chamber for suspending particles and two stationary sections for the optical path, analyte introduction, and particle sampling. The rotating portion consisted of a 24" diameter 316 stainless steel main chamber and faceplates (Kurt J. Lesker, Inc. MJ5GG28196 and QF630-BF) shown in Figure 2.3A and 2.3B. The axle (Figure 2.3D) attaches to the faceplate from the inside of the chamber. Two double-walled ball bearings (VXB Bearing KA050CP0) were pressed onto the outside of each axle and rest on a clamp affixed to the stand. The bearings allow the chamber to rotate while a fixed tube remains stationary (Figure 2.3E), which houses gas and aerosol ports and the CRDS optical mounts (Requirement 1). Stainless steel is a robust, conductive material, which is necessary to reduce aerosol loss due to electrostatic forces (Requirement 2). Stainless steel is used throughout the chamber construction unless otherwise noted. Three rotary vacuum seals (SKF 36740 LDS) hydraulically pressed into each axle keep the chamber airtight between the fixed tube and the axle. A 1/8 HP parallel shaft DC gear motor (McMaster 6470K87) powered by an AC to DC, variable speed controller regulates the chamber rotation speed. A cut-to-length, ¾" wide timing belt (McMaster 1840K4) and L-series quick disconnect pulley mounted to the motor shaft ensures minimal slipping while the chamber rotates.

Both stationary fixed tubes house six ports necessary for every experiment (Requirement 3). Each port welded onto the fixed tube is a male VCR port (6LV-4-HVCR-1-6TB7). The port on the top of the fixed tube is dedicated to aerosol introduction. A 90° tube welded between the aerosol port on the fixed tube and a channel machined into the axle provides a dedicated pathway for aerosol introduction and sampling (Figure 2.3 Aerosol Intro/Sampling, Requirement 2). The fixed tube/axle channel allows for aerosol introduction and sampling through a stationary port while the chamber rotates (Requirement 1). Both axle channels have eight male VCR ports (6LV-4-HVCR-1-6TB7) that connect to the four modifiable ports on the faceplate via stainless steel tubing. The four additional axle ports provide options for the shortest possible path with the fewest 90° angles for aerosol introduction in order to reduce particle loss (Requirement 2 and 4). The unused ports are capped. The modifiable

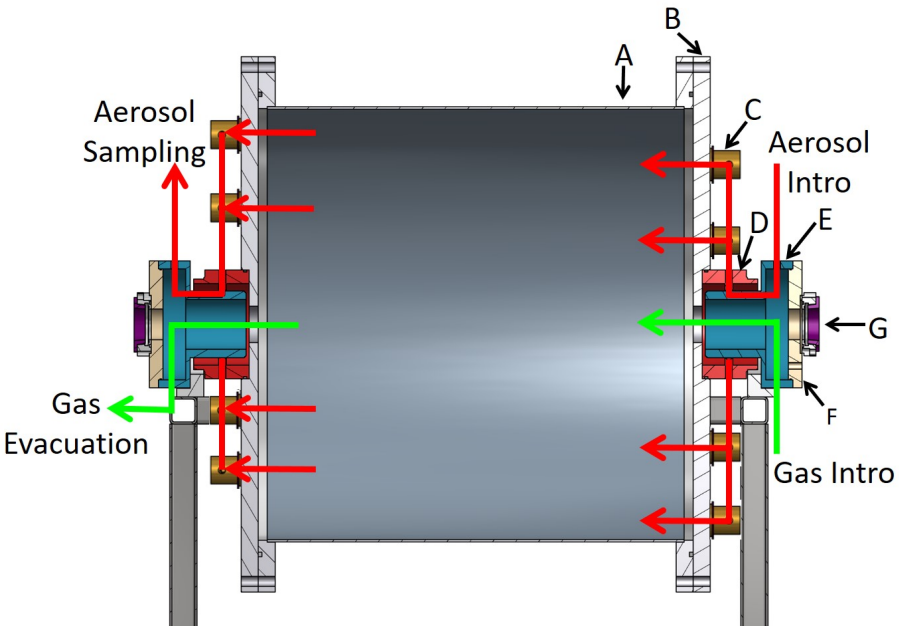

Figure 2.3: Cross-sectional assembly drawing of the chamber design. Part A is the 222.4 L main chamber. Part B is the faceplate modified to mount four aerosol ports (C) and the axle (D). The stationary fixed tube (E) has six male VCR ports equally spaced around the larger diameter section. The CRDS optical mounts for the highly reflective mirrors (G), RH/T probe (not pictured here), and pressure gauge (not pictured here) are attached to the end plate (F) on the gas evacuation side of the chamber. Newly generated aerosols flow through a 90° tube welded between the vertical introduction port and a hole bored in the smaller diameter section of the tube extension, which is aligned with a separate channel in the axle. The ports (C), connected to the axle via stainless steel tubing, are located at radii of 5 in, 7 in, 9 in and 11 in. Background and analyte gases flow through ports on the tube extension and into the main chamber through a 2 in hole in the faceplate.

ports are mounted to the main chamber faceplate at different radii (5 in, 7 in, 9 in and 11 in from center, Figure 2.3C). The ports located at four, different radii for aerosol introduction allows us to assume the particle introduction process is uniform throughout the entire chamber. The four ports also allow for sampling at a variety of locations in order to characterize spatial distributions and verify uniform aerosol distributions during an experiment. One fixed tube port is dedicated to evacuating the chamber via a vacuum scroll pump. The chamber is kept under vacuum between experiments to remove gases and aerosols and maintain a clean chamber (Requirement 6). Background and reagent gas introduction occurs through ports on the fixed tube opposite of the pump.

Endplates on the fixed tubes contain mounts for the CRDS optics and other instrumentation. Los Gatos Research, Inc. (LGR, Inc.) manufactured the two optical mounts for the highly reflective mirrors. Both endplates contain a machined inset designed to house the optical mounts. A Rotronic humidity/temperature probe (HC2-IE302) and an MKS absolute capacitance manometer pressure gauge (727A13TCE2FB) mounted to one endplate continuously monitor the model atmospheric conditions within the chamber (Requirement 5).

2.4. Optical Set-up

As described above in Section 2.2.2, CRDS relies on a pulsed laser source injected into a rigid optical cavity formed by a pair of highly reflective mirrors. The optical cavity within the ACSI was established along the axis of rotation (Figure 2.4). In this arrangement, a planar Au-coated mirror focused pulsed laser light from the external cavity tunable quantum cascade laser (Daylight Solutions 11100-UT, 9 μm to 12 μm, 35 kHz pulse frequency, 0.5 μs pulse width) through a 5 mm hole in a reinjection mirror (Newport 20DC500ER.1). The pulse width is much less than the average $\tau_o(\nu)$ (2 μs–4 μs) and the pulse frequency allows for the decay of light ($I(\nu,t)/I_o(\nu)$) to approach zero between pulses, ~30 μs. A tunable laser is necessary to record the ring-down time at different frequencies by tuning through the wavelength range at 0.5 cm^{-1} step sizes, which will produce a mid-infrared spectrum of the gases within the chamber. The spectroscopic range in the mid-infrared allows us to detect most common VOCs with minimal interference from $PM_{2.5}$. Section 3.2.3 describes the interaction between fine particulate matter and light in more detail, specifically Rayleigh scattering.

After passing through the hole in the reinjection mirror, the light enters the optical cavity formed by two 50.8 mm diameter, 5 mm thick, plano-concave zinc selenide (ZnSe) mirrors that have a broadband highly reflective coating (9.9–12.4 μm) and a 0.9949 m radius of curvature from II-VI Infrared. Zinc selenide is a robust material that withstands most corro-

sive gases, humidity and large pressure differentials while maintaining infrared transparency. Transmission of small amount of light through the mirror closest to the laser is reflected back into the optical cavity by the reinjection mirror with each round-trip. The reinjection mirror increases the ring-down time and the sensitivity by up to an order of magnitude. A 2 in diameter ZnSe meniscus lens (ULO Optics 20ZLF43/10.0 μm) collected and focused light transmitted through the exit mirror, which is then detected by a photovoltaic HgCdTe detector (PV-MCT, Teledyne J19D11-M204-R01M-60). The PV-MCT signal is amplified by 10^5 (FEMTO DLPCA-S1) then digitized by the NI-DAQ board. A LabVIEW program developed by LGR, Inc records the decrease in light intensity over time at 10 million samples/s for 20,000 traces that are boxcar averaged with 2000 points at each frequency before calculating the characteristic ring-down time, ($\tau(\nu)$). The data collection is triggered by the falling edge of the pulse and the first 40 points after the trigger are omitted from the data analysis. The falling edge trigger and the data point omission ensures the data involved in calculating the τ is due to the ring-down and not the 0.5 μs pulse width of the laser. Any calculated $\tau(\nu)$ outside of 0.3–10 μs is rejected by the LabView program. Plots of $\tau(\nu)$ (μs) versus time (s) or wavenumber (cm^{-1}) provide the change in absorption overtime or an infrared spectrum, respectively. Appendix Figure A.3 shows the ring-down time, $\tau_o(\nu)$, and mirror reflectivity (R) when the chamber is filled with ~700 Torr of ultra high purity nitrogen. Figure 2.4 depicts the optical set-up described above.

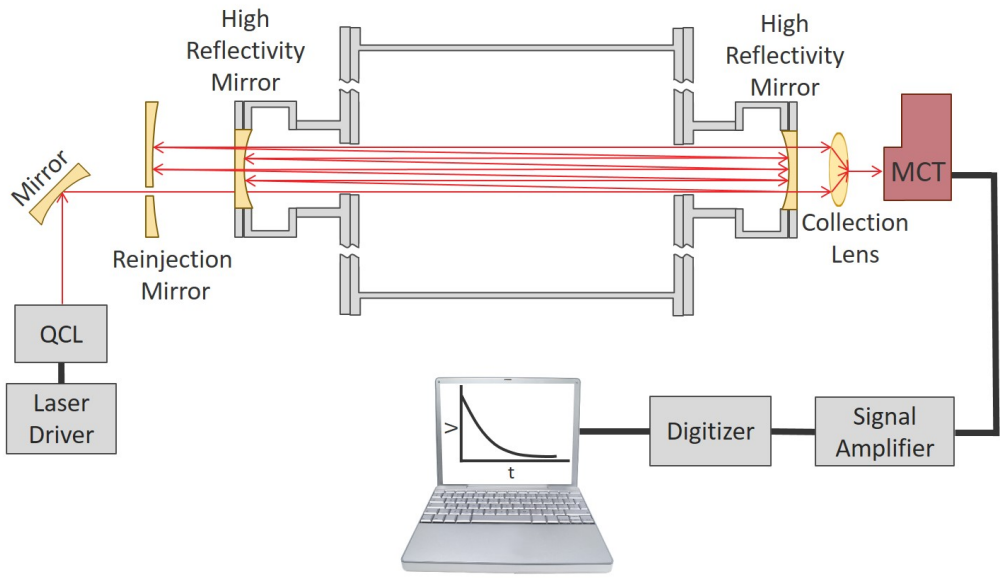

Figure 2.4: Optics schematic involved in acquiring CRDS infrared spectra. Laser light is focused into the cavity through a 5 mm hole in the reinjection mirror using flat mirrors. Two highly reflective mirrors create the optical cavity that produces the ring-down. A lens collects the exiting light, which is then detected by a PV-MCT. A LabVIEW program records the intensity after the signal is amplified and digitized. Not drawn to scale.

2.5. Experimental Background Measurement Procedure

The chamber is kept under vacuum (<1 Torr) between each experiment to remove existing particulate matter and residual gas phase species, which satisfies Requirement 6. Each experiment began by closing the evacuation valve and flowing in 5000 SCCM of ultrahigh purity nitrogen (UHP N_2) using an MKS metal sealed mass flow controller (GM50A013503SBV020) until the main chamber pressure reached atmospheric pressure, approximately 695–715 Torr for Blacksburg, Virginia. The motor was then set to rotate the chamber at the desired speed and a background IR spectrum was recorded. An Aerodynamic Particle Sizer (APS, TSI 3321) or a Scanning Mobility Particle Sizer (SMPS, TSI 3080 EC/TSI 3081 DMA/TSI 3782 CPC)) sampled the UHP N_2-filled, rotating chamber to ensure minimal or no residual particles were present from previous experiments or laboratory air. A port on the opposite side of the chamber to the sampling tube was opened to filtered laboratory air (Parker Balston 9922-05-CQ) to maintain atmospheric pressure within the chamber during active sampling.

The filter removed 99.98% of the particles >0.5 μm. A series of control studies using the CRDS and particle sizers showed that the open filter had negligible effect on the gas-phase composition and particle concentration inside the chamber (see Section 2.5.2). At this point, the relative humidity is increased to the desired amount using the procedure outlined in Section 2.5.1.1.

2.5.1. Humidity Control

Water vapor in the atmosphere, or humidity, varies based on the weather and location. Relative humidity is the ratio of the partial pressure of water vapor (p_{H_2O}) to the saturation vapor pressure of water ($p^o_{H_2O}$) at a specific temperature (Equation 2.10).

$$\% \text{ RH} = \frac{p_{H_2O}}{p^o_{H_2O}} \times 100 \tag{2.10}$$

The Saharan desert, for example, has an average 25% RH, coastal regions average ~70% RH, and clouds and fog have 100% RH.[19,20,123] The atmospheric water vapor concentration determines the dominant removal process of a particle, such as cloud and fog processing (wet) or deposition and coagulation (dry). The dominant removal process directly affects the particle lifetime. Wet removal processes are more effective at reducing fine particle concentrations when compared to dry processes. For instance, particles in a relatively dry Arctic climate experience longer atmospheric lifetimes (several weeks) than those in tropical climates (less than a day).[12,13] Particle composition dictates the state the particle is in, liquid or solid, and depends on the relative humidity. Therefore, a model atmosphere in an experimental setting requires the ability to control the water content within the chamber (Requirement 5).

Our current design approach incorporated the ability to control the water vapor, or humidity, in the chamber using a tandem bubbler system explained in the following sections. Chapter 3 and Chapter 4 describe experiments performed to determine the effect of variations in humidity on aerosol dynamics and heterogeneous chemistry.

2.5.1.1. Water Vapor Introduction Procedure

The procedure for introducing humidity into the chamber started with background measurements, described in Section 2.5. UHP N_2 flowed through an elastomer-sealed, MKS mass flow controller (GE50A013503SBV020) at 2500 SCCM through two Nalgene bubblers containing HPLC grade, submicron filtered water (Figure 2.5A&B). A third container, downstream of the bubblers and preceding the chamber, captured any large water droplets before the humid nitrogen flowed into the rotating chamber (Figure 2.5C). In conjunction with the wet nitrogen introduction, approximately 500–1500 SCCM of dry UHP N_2 was added into the chamber to prevent condensation on the CRDS mirror. A valve opened to the laboratory, equipped with a Parker Balston filter, prevented over-pressurization within the chamber during the humidity introduction process. Figure 2.5 depicts the humidity control set-up.

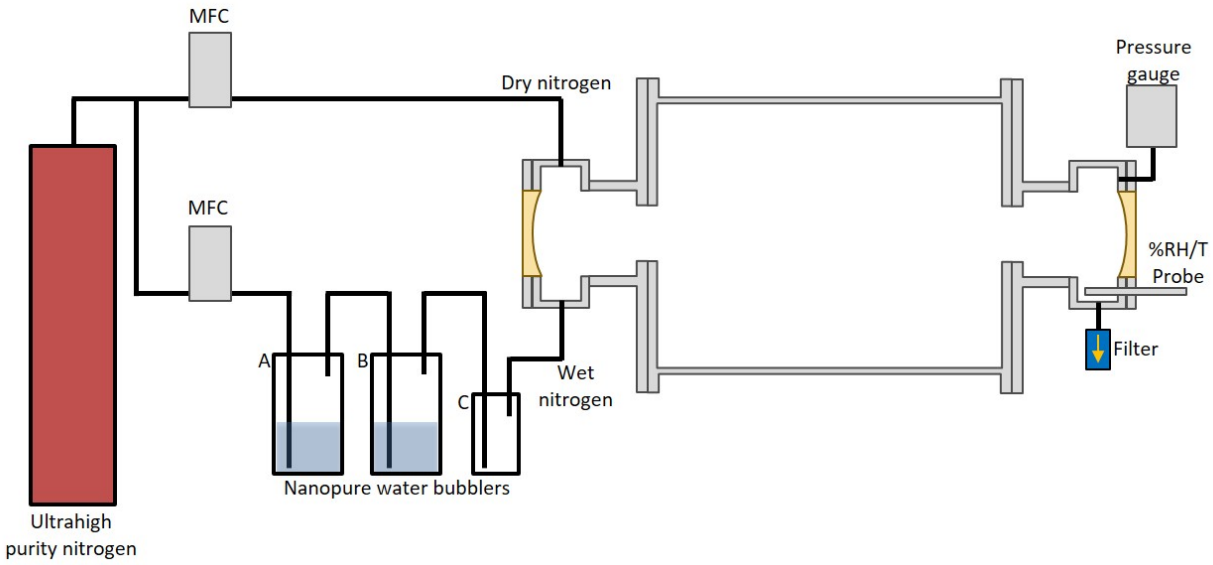

Figure 2.5: Schematic for humidity control system. UHP N_2 flows through the nanopure water in the series of bubblers (Nalgene containers A & B). The wet nitrogen then flows through container C, an empty container, to trap any large droplets or condensation before entering the rotating main chamber. Dry nitrogen simultaneously flows into the main chamber to prevent condensation on the mirror. A relative humidity and temperature probe monitors the composition on the opposite side of the chamber. A Parker Balston filter is opened to laboratory air to prevent over-pressurization. Not drawn to scale.

Introduction of the humid/dry nitrogen mixture continued until the chamber reached

the desired relative humidity (up to ~80% RH), measured by a Rotronic relative humidity and temperature probe (HC2-IE302). Rotating the chamber shortened the time required to reach the chosen relative humidity compared to a stationary chamber. Figure 2.6 shows the % RH recorded with the Rotronic % RH/T probe during the humidity introduction for an experiment requiring 60% RH.

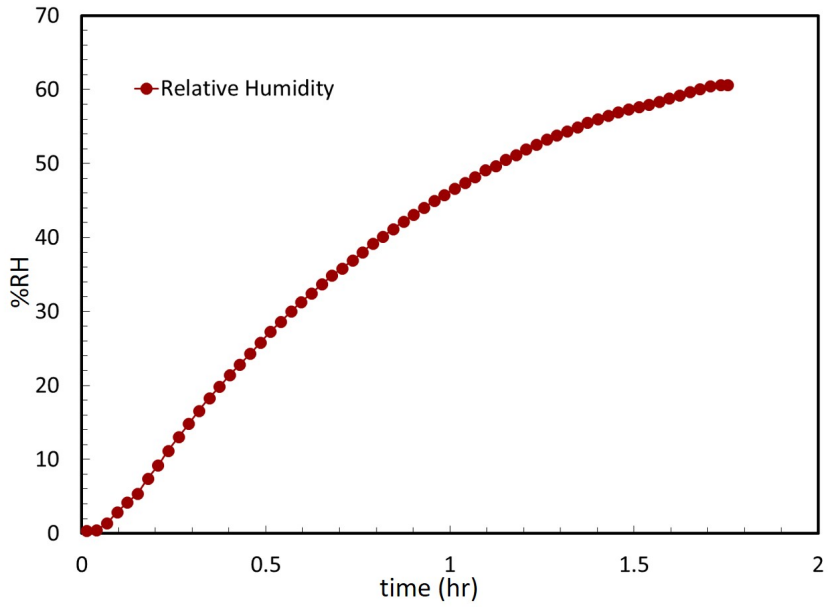

Figure 2.6: Humidity introduction process monitored via the RH/T probe. 60% RH achieved after approximately 2 hours of water vapor introduction.

2.5.1.2. Water Vapor Spectral Analysis

An important aspect of the humidity control system in the ACSI is understanding the effect water vapor has on the CRDS mid-infrared spectra. Water vapor has two intense spectral features close to, but outside of, the ACSI CRDS spectroscopic window. The two spectral features detected with traditional, single-pass spectroscopic techniques are the P-branch of the asymmetric bending rovibrational band centered around 1595 cm^{-1} and a pure rotational band centered at 204 cm^{-1}. These spectral features overlap in the CRDS spectral window (860–1010 cm^{-1}). Figure 2.7 shows the High Resolution Transmission (HITRAN) simulated spectra of the rovibrational and rotational bands of water below 2000 cm^{-1}, as

well as an inset of the wavelength range accessible via the CRDS incorporated into the ACSI.[124,125] Notice the spectral line intensities of water between ~860–1010 cm^{-1} are five orders of magnitude lower in intensity than those typically detected with traditional, single-pass spectroscopic techniques.

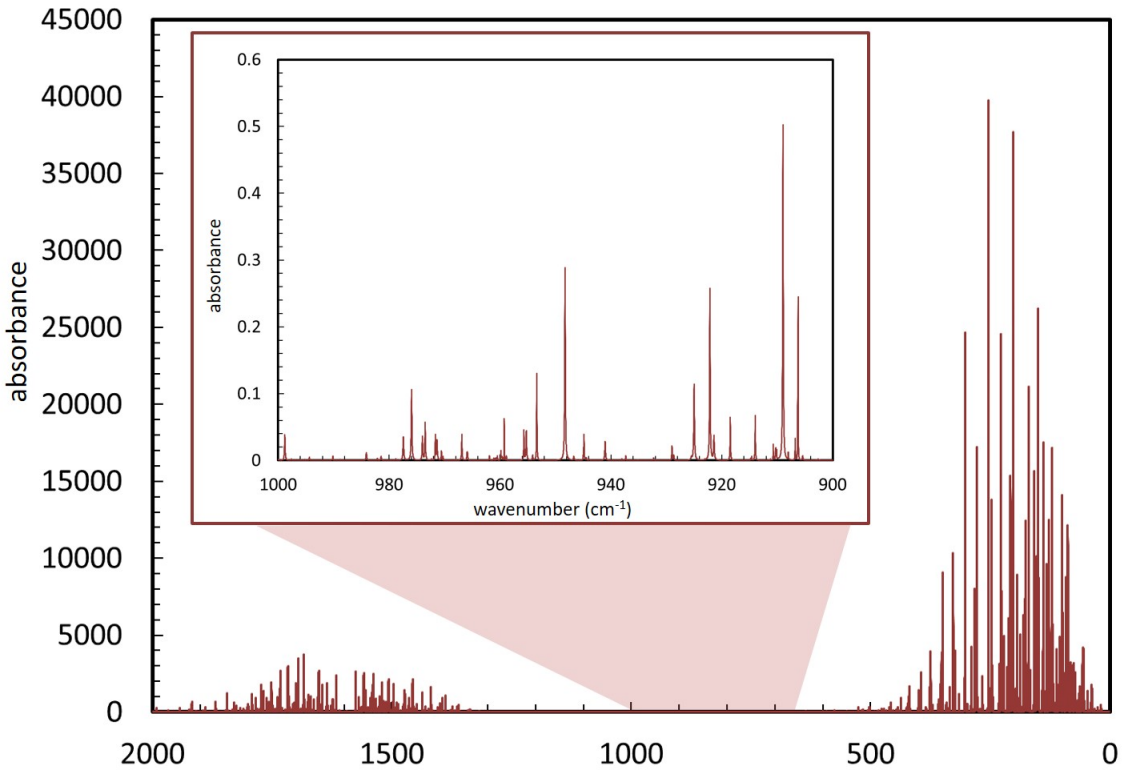

Figure 2.7: Simulated spectra of the rovibrational and rotational bands of water below 2000 cm^{-1} using SpectraPlot.[126] The pressure is 1 atm, path length is set to 80000 cm (comparable to the ACSI CRDS set-up), temperature is 300 K and χ_{H_2O} is 0.0016. The inset includes the spectral features in the wavelength range accessible via mid-infrared CRDS. The spectral line positions and intensities are calculated with the process described in Reference 126 using the database in Reference 125.

A highly detailed spectrum of water vapor recorded by the ACSI CRDS in Figure 2.8 illustrates the sensitivity of the multi-pass technique. The figure shows excellent agreement between the average spectrum of 11.4 Torr water vapor, or 61.3±0.7 % RH, and the scaled HITRAN calculated spectral line positions and anticipated relative intensities.[124,125]

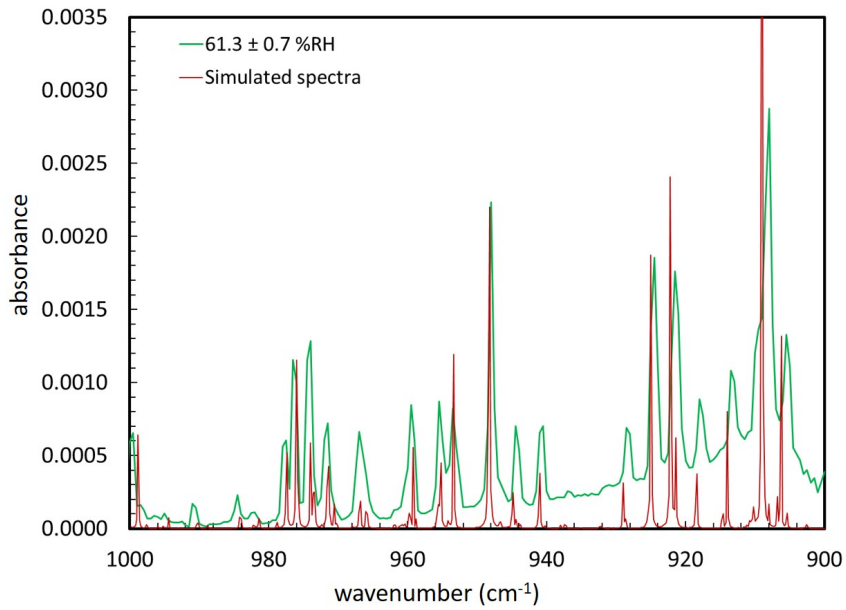

Figure 2.8: Offset absorbance spectra of 11.4 Torr of water vapor (61.3±0.7 % RH, red line) filled to 700 Torr with UHP N_2. Simulated water spectra using the algorithm developed by Goldenstein et al. showing excellent agreement between the computational model and experimental data.[126]

The water vapor spectrum recorded with the CRDS shows a sharp peak in the middle of the spectral window at 948 cm^{-1}. The change in absorbance at 948 cm^{-1} was recorded over time to monitor the humidity introduction process, also referred to as a 'free-scan'. Figure 2.9 compares the absorbance at 948 cm^{-1} free-scan to the % RH recorded with the Rotronic humidity probe for an experiment that required 60% RH in the model atmosphere. The quicker response to the humidity introduction in the CRDS free-scan is due to the water vapor that immediately entered the optical path but had not yet reached the humidity probe. After the water vapor reached a uniform concentration throughout the chamber, the signal from the CRDS directly correlated to the % RH recorded by the humidity probe. The free-scan also ensured that there is no condensation on the highly-reflective mirrors while increasing the humidity. If condensation were to occur, there would be a complete loss of the ring-down signal.

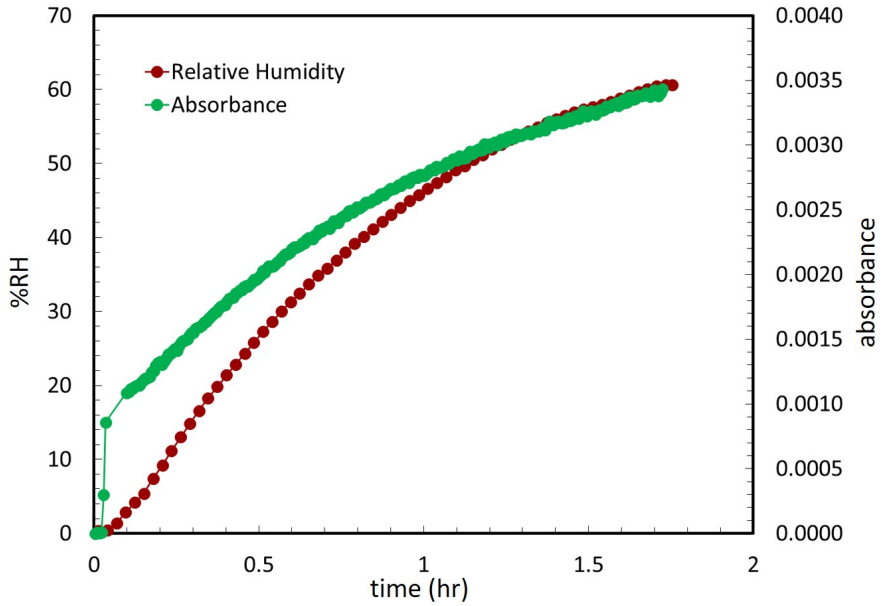

Figure 2.9: Humidity introduction process monitored via the RH/T probe (red, left axis) and CRDS (green, right axis). The CRDS recorded the ring-down time for 948 cm^{-1} over time. Absorbance was determined using Equation 2.8 where $\tau_0(\nu)$ is the ring-down time recorded before beginning the water vapor introduction process.

2.5.2. Parker Balston Filter Control Studies

Valves open to the laboratory equipped with particulate matter filters maintained atmospheric pressure during aerosol and humidity introduction as well as aerosol sampling. The Parker Balston particulate matter filters (922-05-CQ) were selected as a cost-effective option to filter 99.98% of particles >0.5µm. The size range was chosen to capture the particles used in experiments as well as those present in the laboratory. The following sections explore the effectiveness of these filters throughout a standard experiment.

The procedure for increasing the humidity in the chamber resulted in a positive pressure differential between the chamber and the laboratory, which forced air out of the Parker Balston filter. The filter also restricted the introduction of chamber contents into the laboratory space. Figure 2.10 represents the average water vapor spectrum recorded for different experiments after the background, dry UHP N_2 was displaced with the water vapor and UHP N_2 mixture. Gas-phase contamination from the laboratory air during the humidity introduction

process would appear as new peaks in the infrared spectrum for higher humidities, which required a longer introduction time to achieve the desired humidity. As expected, agreement between the average water vapor spectra at each relative humidity suggests that the humidity control process does not introduce significant amounts of gas-phase contaminants.

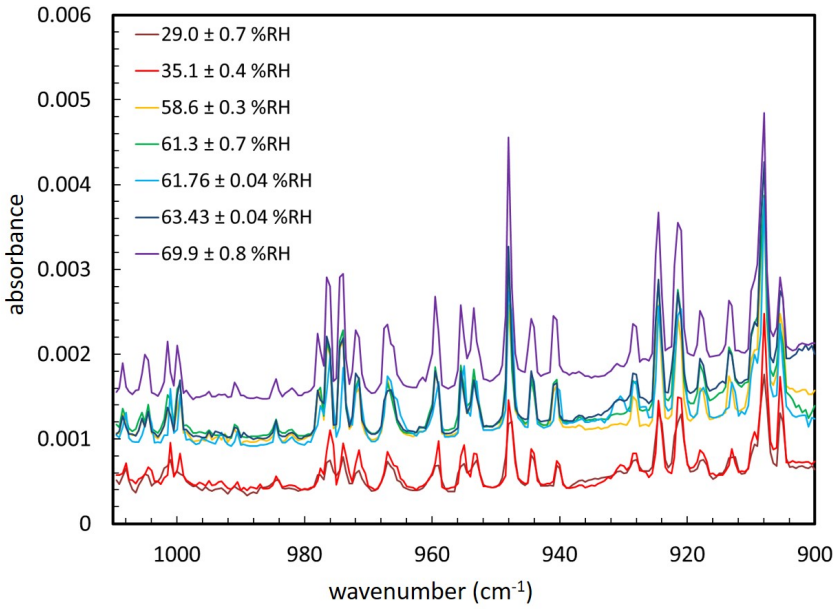

Figure 2.10: Average CRDS spectra for positive pressure Parker Balston filter control. Each spectrum represents the average spectrum for different relative humidities. Humid nitrogen was added to the chamber by flushing out dry nitrogen through a Parker Balston filter.

Each spectrum in Figure 2.10 is the spectrum determined with the CRDS, i.e. there is no offset for clarity. The increase in baseline as the relative humidity increases is likely caused by the water vapor self-continuum.[127] According to current reports, the water vapor self-continuum is caused by water–water molecular interactions, in addition to water–nitrogen and water–oxygen interactions.[127] Some spectral databases and atmospheric models use a semi-empirical value for modeling the self-continuum in different wavelength ranges. To the best of my knowledge, the water vapor self-continuum for the ASCI spectral range has not been quantified in a laboratory study.

In addition to the water vapor self-continuum, the line width of the pulsed laser also prevents quantification of molecules with sharp rovibrational spectral features, like water

vapor. The line width of the pulsed laser employed in the CRDS is approximately 1 cm^{-1} (Figure A.10). The average full width at half maximum (FWHM) for the rovibrational and rotational spectral features for water in the ACSI spectral range is less than 0.4 cm^{-1}. Water vapor and other molecules with spectral features that exhibit a FWHM less than the laser line width cannot be quantified with the current set-up. Therefore, a calibration curve for different relative humidities cannot be produced with the information available.

A negative pressure differential, created by sampling process of the particle sizers, introduced filtered laboratory air into the chamber. The following control experiment involving polydisperse ammonium sulfate particles in a 50% RH model atmosphere determined the filtered laboratory air drawn into the chamber did not introduce appreciable gaseous contaminants. Ammonium sulfate particles in various model atmospheres are the basis of the initial experiments described in Chapter 3 and Chapter 4. Approximately 50% RH and a polydisperse distribution of ammonium sulfate particles were added to the main chamber. Particles were sampled at 0.4 SLPM for two minutes in triplicate using the SMPS every half hour. Multiple CRDS spectra were recorded between each particle sampling. Figure 2.11 shows the average spectrum between each particle sampling event. Gas contamination from the laboratory air would appear as new peaks in the infrared spectrum, which would increase over time as more and more laboratory air is drawn into the chamber with each round of aerosol sampling. No additional CRDS spectral features appear after 10 sampling events over five hours, indicating negligible gas-phase contaminants from the filtered laboratory air were drawn into the chamber during the particle sampling process.

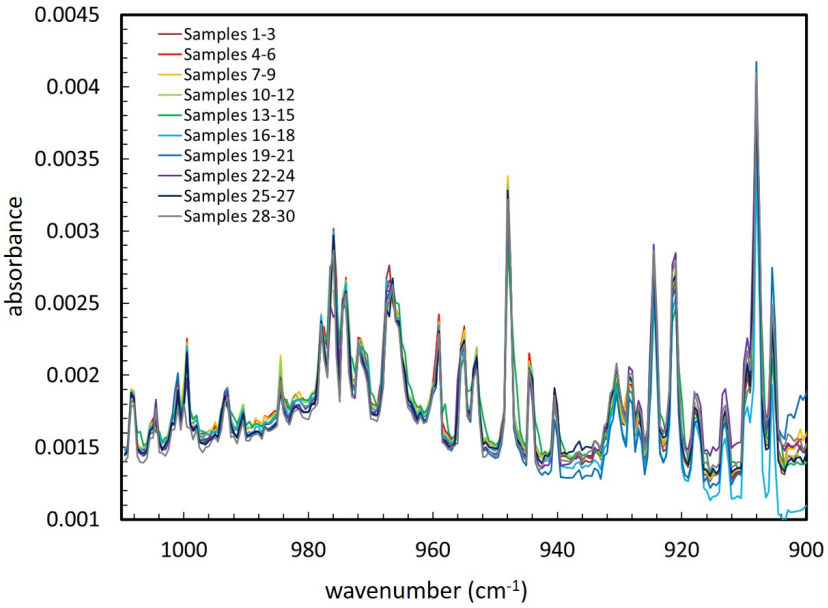

Figure 2.11: CRDS spectra for negative pressure differential Parker Balston filter control. Each trace represents the average spectrum after each set of three particle samples.

The negative pressure differential induced by the standard aerosol sampling procedure has the potential to introduce contaminant particulate matter along with gas-phase impurities. Figure 2.12 shows the particle sampling data from the same ammonium sulfate and ~50% RH experiment described above for Figure 2.11. The introduction of particulate matter through the Parker Balston filter during the course of the experiment is insignificant and negligible compared to the amount of analyte aerosols. If the filtered laboratory air introduced particle contaminants, there would be a non-zero particle concentration to after humidity introduction and an increase in particle concentration throughout the course of the control experiment. The Parker Balston particulate matter filters are effective at preventing appreciable gas and particulate contamination during different aspects of the experiments reported in Chapter 3 and Chapter 4.

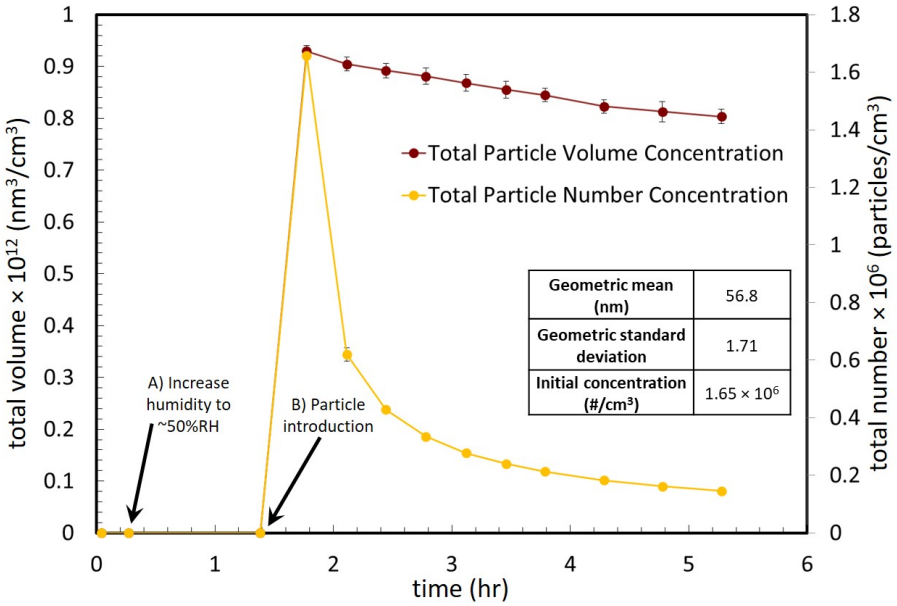

Figure 2.12: Ammonium sulfate particle concentration over time during the Parker Balston filter control. The left axis corresponds to the dark red trace representing the total particle volume concentration (nm^3/cm^3). The right axis corresponds to the yellow trace representing the total particle number concentration ($particles/cm^3$). The initial particle distribution characteristics are listed in the inset. Error bars represent absolute error of the average value, error bars smaller than the data point markers are not displayed.

Polydisperse particle distributions in experimental settings experience a decrease in particle number concentration from inter-particle coagulation, deposition, and dilution from particle sampling techniques. In order to understand how experimental parameters might affect coagulation, I need to understand the other ways particles are lost within the chamber during an experiment. The computational model results and monodisperse experiments using particles of various sizes provide insight on particle number concentration decrease due to deposition. A simple calculation in the analysis will account for the particle dilution from the sampling procedure with an APS or SMPS. Particles are drawn out of the main chamber during particle sampling events at a set flow rate and sampling duration. The volume of particle-laden air removed from the chamber is replaced with the same volume of filtered laboratory air. Equation 2.11 is used to correct the diluted, measured particle concentration (C_d) back to the concentration prior to sampling (C) after some number of samples (n_s).

The sample volume (V_s) is determined by multiplying the sample flow rate by the sample duration. Total volume (V_{tot}) is the chamber volume (222.4 L). Every particle concentration-related figure reported in the following sections using this instrument has been corrected for the particle dilution using Equation 2.11. Any particle concentration loss detected after correcting for dilution are from other causes, such as coagulation or deposition.

$$C = \frac{C_d}{1 - \frac{n_s V_s}{V_{\text{tot}}}} \tag{2.11}$$

2.6. Summary

The final chamber design addressed all of the major experimental criteria and maintained the ability to adapt to future research requirements. The computational model in Sections 2.2.1 and 2.2.2 supports the decision to utilize a rotating chamber for extending particle suspension duration while monitoring the gas-phase with cavity ring-down spectroscopy. The following chapters explore the experimental capabilities of the chamber to extend particle suspension durations for selected types of particles (Chapter 3) and the ability to observe heterogeneous chemistry in a variety of model atmospheres (Chapter 4).

Chapter 3

Particulate Matter Suspension Characterization

3.1. Introduction

Particles between 0.1–2.5 μm experience various aerosol aging processes including vapor condensation, surface and bulk heterogeneous reactions, and coagulation with other existing particles to form larger particles. $PM_{2.5}$ exists for days to weeks longer than ultrafine (<0.1 μm) and course (>2.5 μm) particles, allowing for aerosol aging to occur.[14] See Section 1.2.1 for more information on particulate matter atmospheric lifetimes. Atmospheric aging transforms existing particles into complex mixtures of condensed materials, different primary particles, and products from other atmospheric reactions. Such aging processes could affect the hygroscopicity of an insoluble particle, such as mineral dust, or even increase the size enough to enhance removal processes.[13,72] Creating a model atmosphere with pollutant-type molecules allowed us to study simulated particle transport through the atmosphere.

Fine particulate matter laboratory research requires the ability to extend lab-generated aerosol suspension durations to atmospherically relevant timescales. The slowly rotating ACSI main chamber hypothetically lengthens particle suspension durations to several hours or even days, see Chapter 2 for more information on the rotating main chamber.[112–114,128] I developed the ACSI to explore and understand simpler, well-controlled, heterogeneous reactions involved in the overall fine particulate matter aging processes. Determining the suspension efficiency for a well-characterized particle distribution in the rotating main chamber provided the foundation for understanding the effects of complex model atmospheres on polydisperse aerosol dynamics. The first particles used were monodisperse polystyrene latex spheres (PSLs). PSLs bridge the gap between computational models, which involved monodisperse hard spheres,[16] and real laboratory experiments. The larger, 1 μm particles represented the maximum particle size that required high suspension efficiencies in the ro-

tating main chamber. The initial heterogeneous chemistry experiments began with smaller particle distributions that approached 1 μm through coagulation (Section 3.4.2).

Polydisperse, ammonium sulfate aerosols are used in the heterogeneous chemistry experiments described in Chapter 4. Inorganic salts are generally produced via gas-phase acid-base reactions. Salt particles have peak mass concentrations in particles between 0.1–1.2 μm in diameter, within in the size definition of $PM_{2.5}$.[38] The polydisperse ammonium sulfate particles are assumed to be solid when no water vapor was added prior to aerosol introduction. Ammonium sulfate particles are known to be in the solid phase below the characteristic efflorescence relative humidity (35% RH).[129–131] See Section 3.5 for more information on deliquescence and efflorescence of water-soluble molecules. The ammonium sulfate particles are expected to be aqueous droplets when the relative humidity increases above the characteristic efflorescence relative humidity. Controlling the particle phase state and composition allowed for further characterization of how different model atmospheres affect aerosol coagulation dynamics.

The following aerosol dynamics experiments described in this chapter included well-characterized monodisperse PSLs, monodisperse and polydisperse solid ammonium sulfate particles, polydisperse ammonium sulfate, and polydisperse acidic ammonium sulfate particles suspended in a humid chamber. The experiments described in Chapter 4 incorporated the polydisperse suspensions, increased relative humidity, and finally pollutant introduction into the model atmosphere.

3.2. Monodisperse Fine Particulates

Various types of particle suspensions were characterized in the rotating ACSI main chamber to fully understand the effect heterogeneous reactions have on the atmospheric lifetime of $PM_{2.5}$. A series of experiments explored the effect of rotating the chamber on a aerosol dynamics for a variety of particle compositions and distributions. Monodisperse, 0.994 ± 0.012 μm diameter, polystyrene latex solid spheres (PSLs) were chosen as the simplest particle, which

directly related to the computational model described in Section 2.2.1. One-micrometer particles are mid-range $PM_{2.5}$, ($0.1\ \mu m < d_p < 2.5\ \mu m$). The PSLs also represent the upper size range of the aged particles in the polydisperse coagulation experiments, which began with smaller ammonium sulfate particles that undergo coagulation and condensation until the largest particles in the distribution approach 1 μm.

One of the key objectives for the PSL experiments was to define a standard experimental method for maximizing particle suspension durations. The chamber rotation rate was limited experimentally to ~1–2 RPM to minimize belt slipping and deterioration, which arose in low (<1 RPM) and high (>5 RPM) rotating speeds, respectively. Computational models predict high particle suspension efficiencies for rotation rates between 1–2 RPM for particles smaller than ~1 μm (Figure 3.1).[112–114]

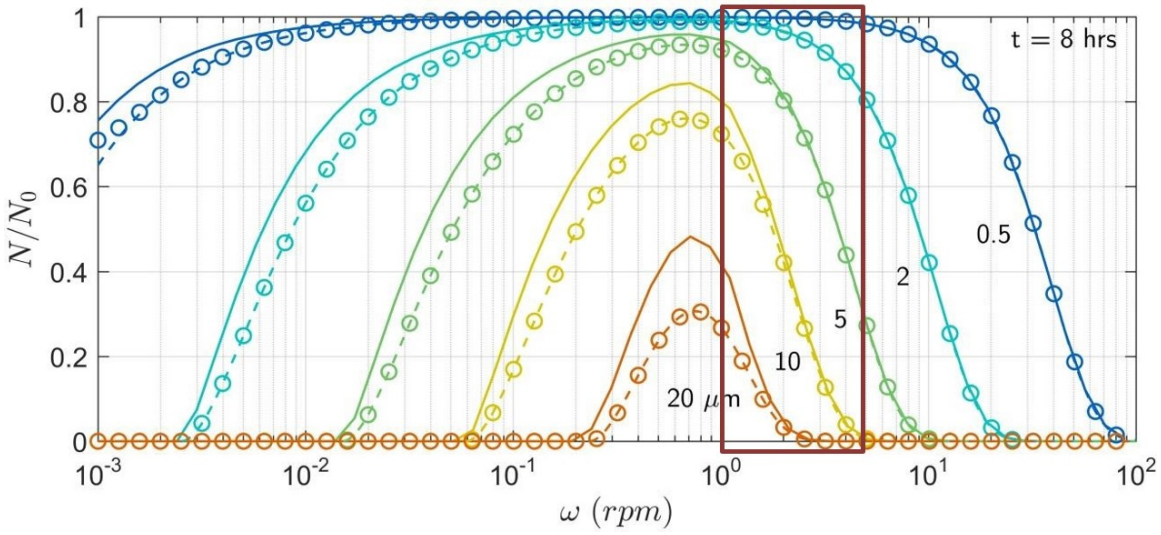

Figure 3.1: Computational models from Asgharian and Moss (solid)[113] Gruel et al. (dashed)[112] and Brown and Dhaniyala (o)[114] models for particle suspension efficiency (N/N_o) as a function of chamber rotation rate for multiple particle sizes and a test duration of 8 hrs. The dark red box represents the practical rotation rates accessible with the ACSI system (1–5 RPM). The figure is adapted from Reference 114.

3.2.1. Experimental Details

3.2.1.1. Materials

The particles employed in this section are monodisperse 0.994 ± 0.012 μm spherical polystyrene latex particles (PSLs) suspended in water with a proprietary surfactant to minimize coagulation in solution were purchased from Thermo Fisher Scientific (Duke Standards 4009A). Research grade UHP N_2 was purchased from Praxair, Inc. The deionized water was acquired from Hahn Hall South (Millipore Purification Systems, 18.2 MΩ).

3.2.1.2. Particle Introduction

At the beginning of the experiment, background measurements were recorded using the procedure described in Section 2.5. The rotating chamber was then evacuated to approximately 350 Torr in preparation for aerosol introduction. Twenty psi of UHP N_2 flowed through a Collison 6-jet nebulizer filled with 30 mL deionized water and 10–15 drops of the PSL suspension to generate the aerosols. The newly generated aerosol droplets were comprised of PSLs and water. The droplets were dried with a TSI 3062 diffusion dryer before introduction into the main chamber. Particle introduction continued until the chamber pressure reached 600 Torr, then UHP N_2 was added until the chamber returned to atmospheric pressure.

3.2.1.3. Sampling Procedure

The aerodynamic particle sizer (APS, TSI 3321) sampled the particle suspension for two minutes at 1 SLPM approximately every hour for 12–36 hours. The APS measures the aerodynamic diameter of the particle, which is defined as the diameter of a water droplet with the same terminal velocity as the irregular particle (see Equation A.5).[16] Sampling for the experiment discussed in Section 3.2.2 utilized all four ports simultaneously, which yielded the average concentration within the chamber. Sampling occurred through one port at a time for Section 3.2.3, which resulted in information on the radial distribution of particles in the rotating chamber. A port on the tube extension on the opposite side to the sampling port

was opened to filtered laboratory air to maintain atmospheric pressure within the chamber during active sampling.

3.2.2. Suspension Efficiency

Monodisperse, solid PSLs were introduced into the chamber to form a fine particulate suspension. The PSLs were periodically sampled over 16 hours. Three rotation speeds were investigated: 0 RPM, 1 RPM and 2 RPM. Figure 3.2 shows the number suspension efficiency (N/N_o) for each speed, where N_o is the initial 0.994 ± 0.012 µm particle concentration (particles/cm^3) immediately after introduction and N is the particle concentration at each sampling event. Particle concentration dilution due to the sampling process is corrected for using Equation 2.11.

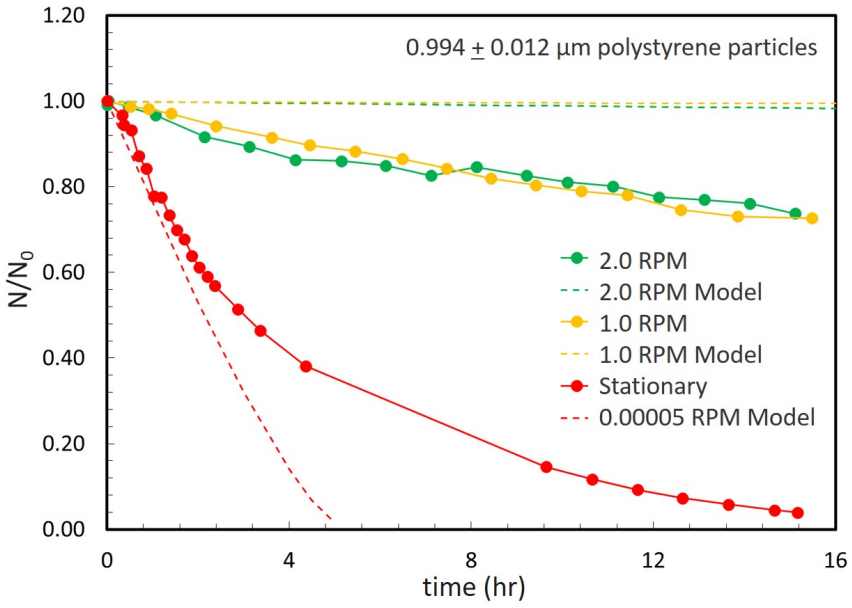

Figure 3.2: Experimental and computed long-term particle suspension efficiency (N/N_o) while the chamber rotates at 1 RPM (yellow) and 2 RPM (green) compared to a stationary chamber (red). The dashed lines correspond to the computed particle suspension efficiency calculated using mathematical models discussed in Section 2.2.1.[114] The particles are 0.994±0.012 µm polystyrene latex spheres. Each data point represents a sample taken with the APS through all four ports simultaneously and was corrected for sample dilution caused by the particle sampling process (Equation 2.11). The lines were added to help guide the eye.

For the stationary chamber (0 RPM), the 0.994 ± 0.012 μm particle concentration falls immediately upon introduction and concentration decreases more than 50% after 2 hours. Monodisperse, 0.994 ± 0.012 μm PSLs should completely deposit after approximately 5 hours according to computational models. However, some of the particles remain suspended longer than the model predicted. We hypothesize the non-ideal, axial flows within the chamber from the sampling/dilution process perturbed the suspension, which lengthened the time required for complete deposition of 1 μm particles.

Computational models suggest that 1 and 2 RPM rotation rates are expected to yield suspension efficiencies >98% for fine particulates on a 15 hour timescale.[112–114] Approximately 70% of the particles remained suspended after 15 hours in the slowly rotating chamber. The models developed by Gruel et al.,[112] Asgharian and Moss,[113] and Brown and Dhaniyala[114] assumed ideal flow scenarios and neglected other forces that negatively affect the particle suspension efficiency. A rotation rate of 2 RPM is used for every experiment unless otherwise noted.

3.2.3. Radial Distribution

A significant design challenge associated with our goal of performing CRDS along the center was the spatial distribution of particles within the rotating main chamber. Particles in the optical path scatter the mid-infrared laser light for the cavity ring-down spectrometer. Our collaborators, Matt Brown and Suresh Dhaniyala at Clarkson University, calculated the concentration profile for 2 μm particles in the chamber rotating at 2 RPM after 16 hours. Figure 3.3A is a half cross-section of the YZ plane of the chamber and the particle concentration is depicted as a color gradient. Figure 3.3B is an XY cross-section of the main chamber. Each red dot represents the location of a 2 μm particle after 16 hours in a rotating chamber. Computational models suggest that $PM_{2.5}$ establishes a uniform distribution throughout the rotating chamber. As shown in Figure 2.4, the CRDS optical path is in the center of the cylindrical chamber, through the uniform particle distribution, which will result in some fraction of light scattered due to the particles.

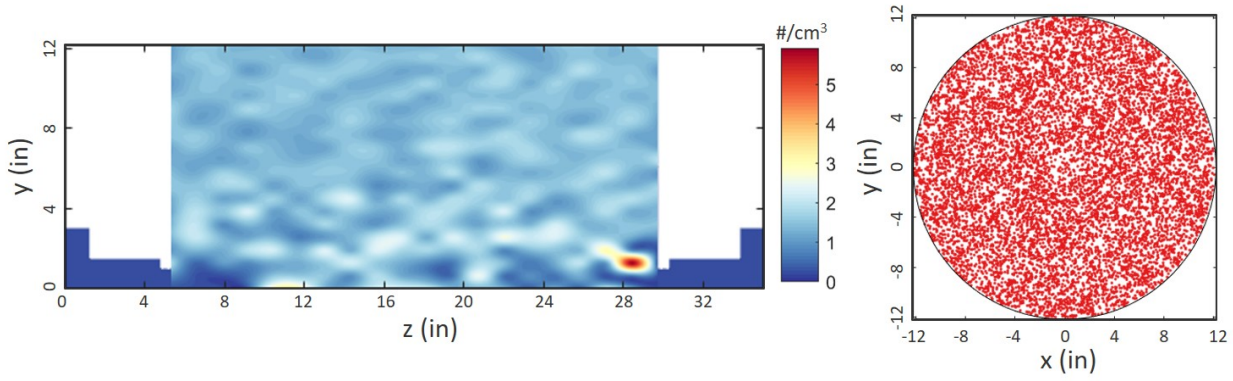

Figure 3.3: A) Computed particle concentration profile in the YZ plane for 2 μm particles after 16 hours while the simulated chamber rotated at 2 RPM. B) Computed particle concentration profile in the XY plane for 2 μm particles after 16 hours while the simulated chamber rotated at 2 RPM. Our collaborator at Clarkson University, Matthew Brown, performed the simulations for the figure.

Mid-infrared light undergoes elastic Rayleigh scattering in the presence of $PM_{2.5}$.[132,133] The ACSI CRDS utilizes mid-IR wavelengths between 9.9 μm and 12 μm. The Rayleigh scattering cross-section is the average fraction of light scattered for a wavelength of light from one particle over all angles. Equation A.20 describes the Rayleigh cross-section in 1 m for one wavelength of light (λ) from a single particle with the diameter, d_p, and refractive index (n). The product of the Rayleigh scattering cross-section and the particle concentration is the total fraction of light scattered from a particle suspension in one meter. Tables 3.1 and 3.2 list the Rayleigh scattering cross-section and fraction of 9 μm and 12 μm mid-infrared light scattered from the typical size and particle concentrations that were used in the following benchmark studies.

Table 3.1: Refractive index, Rayleigh scattering cross-section, and fraction of light scattered from the PSLs and ammonium sulfate particles when $\lambda = 9$ μm with a path length of 1 m.

Particle Material	d_p **(μm)**	**Refractive Index** (n)	σ_s **(m²)**	**N (#/cm³)**	**Fraction of Light Scattered**
Polystyrene latex	0.994	1.563[134]	3.3×10^{-15}	2000	6.6×10^{-6}
Ammonium sulfate	0.100	1.086[135]	9.9×10^{-23}	1×10^{6}	9.9×10^{-12}
Ammonium sulfate	0.400	1.086[135]	4.1×10^{-19}	1×10^{6}	4.1×10^{-8}

Table 3.2: Refractive index, Rayleigh scattering cross-section, and fraction of light scattered from the PSLs and ammonium sulfate particles when $\lambda = 12$ μm with a path length of 1 m.

Particle Material	d_p **(μm)**	**Refractive Index** (n)	σ_s **(m²)**	**N (#/cm³)**	**Fraction of Light Scattered**
Polystyrene latex	0.994	1.563[134]	1.0×10^{-15}	2000	2.1×10^{-6}
Ammonium sulfate	0.100	1.652[135]	1.3×10^{-21}	1×10^{6}	1.3×10^{-10}
Ammonium sulfate	0.400	1.652[135]	5.4×10^{-18}	1×10^{6}	5.4×10^{-7}

According to the information on Rayleigh scattering in Table 3.1 and Table 3.2, one micrometer PSLs and ammonium sulfate nanoparticles elastically scatter a negligible amount of mid-infrared light ($< 2.1 \times 10^{-4}$%). Therefore, minimal Rayleigh scattering occurs in the benchmark and preliminary experiments because the particles are more than an order of magnitude smaller than the mid-infrared light employed by the CRDS.[132,133] Experiments involving particle sizes within an order of magnitude of the CRDS laser wavelength range will need to apply Mie theory to quantify the amount of light scattered by the particles.

The suspension efficiency of the monodisperse PSLs 5 in, 7 in, 9 in and 11 in away from the center axis determined the experimental radial distribution of the particle suspension (Figure 3.4). The introduction and sampling processes were the same as described in Section 3.2.1.2 and Section 3.2.1.3, respectively. However, three of the four valves were closed between the ports and aerosol channel during sampling events to isolate one radius per experiment.

The inset in Figure 3.4 shows the placement of the fours ports on the chamber face plate. Four experiments were conducted in total, one for each radii (5 in, 7 in, 9 in, and 11 in).

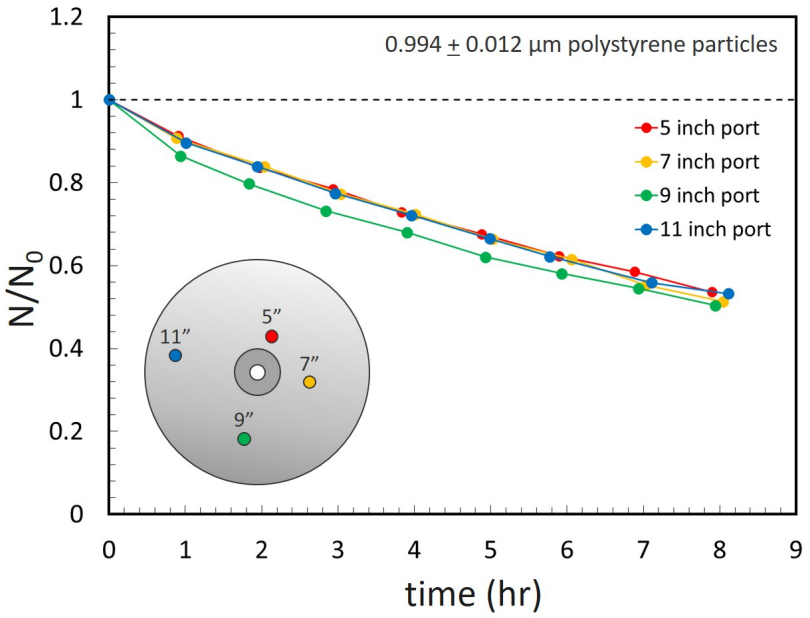

Figure 3.4: Number suspension efficiency (N/N_o) of 0.994±0.012 µm polystyrene latex particles measured at different radii while the chamber rotated at 2 RPM. The data confirmed a uniform distribution of particles throughout the main chamber. The inset shows the placement of the fours ports on the chamber face plate. Each data point represents a sample taken with the APS and was corrected for sample dilution caused by the particle sampling process (Equation 2.11). The lines were added to help guide the eye.

In agreement with computational models, Figure 3.4 indicates the first time long-term uniform particle distributions have ever been reported in a rotating chamber. The uniform distribution and Rayleigh scattering characteristics for 0.994 ± 0.012 µm PSLs results in minimal mid-infrared light scattering from the particles in the CRDS optical path. Any future experiments using the ACSI will need to evaluate the extent different particle types and sizes Rayleigh and Mie scatter the laser light. Next, I explored the suspension efficiency of solid, monodisperse ammonium sulfate salt nanoparticles in the rotating ACSI to transition from a simple, synthetic particle to an atmospherically-relevant system.

3.3. Monodisperse Ammonium Sulfate Nanoparticles

Atmospheric aging processes alter smaller, ultrafine particles that increase in size over time due to coagulation and condensation. High concentrations of ultrafine particles permit particle-particle collisions which initiate coagulation.[16] Background vapors, such as water or other volatile organic compounds condense and partition to the particle phase. Both condensation and coagulation increase particle size. Coagulation decreases the number concentration as particles collide and adhere while condensation preserves the number of particles. Most natural fine particles are considered secondary particles consisting of primary ultrafine particles that have undergone coagulation and condensation processes. Secondary fine particulate matter persists in the atmosphere longer than ultrafine or coarse particles, which allows for aerosol aging, see Section 1.2.1 for more information on atmospheric lifetimes for different sized particles. Fine inorganic salt ions catalyze heterogeneous reactions involving VOCs and particulate matter.[1,74] For example, fine and ultrafine ammonium sulfate particles participate in known atmospheric heterogeneous reactions with amines.[1,106,107] I employed ammonium sulfate for the initial characterization and proof-of-concept experiments because the salt is abundant, reactive, and naturally exists in $PM_{2.5}$.

Monodisperse, dried ammonium sulfate particles consist of an atmospherically-relevant material while satisfying the monodisperse assumptions made in the aerosol dynamics models explained in Section 1.2.1.1. Salt particle generation began with aqueous salt droplets. The droplets flowed through a diffusion dryer, which removed almost all of the water present in the droplets. An electrostatic classifier size selected particles to form the monodisperse distribution. The diffusion-dried, monodisperse particles flowed into the main chamber with no additional water vapor. Figure 3.5 shows a general schematic for monodisperse aerosol generation and introduction into the ACSI. Ammonium sulfate recrystallizes, or effloresces, at 35% RH at 25°C.[129,130] See Section 3.5 and Figure 3.14 for more information on particle phases at different relative humidities. Therefore, the aerosols in the following experiments were solid salt particles rather than aqueous salt droplets because the relative humidity

after particle introduction is below 35% RH. Dried, solid particles are necessary for the initial experiments instead of droplets because the coagulation equations derived in Section 1.2.1.1 assumed solid particles. The experiments in the following sections explore polydisperse particle suspensions introduced into a increasingly complex model atmospheres, which can be perturbed with pollutant gases.

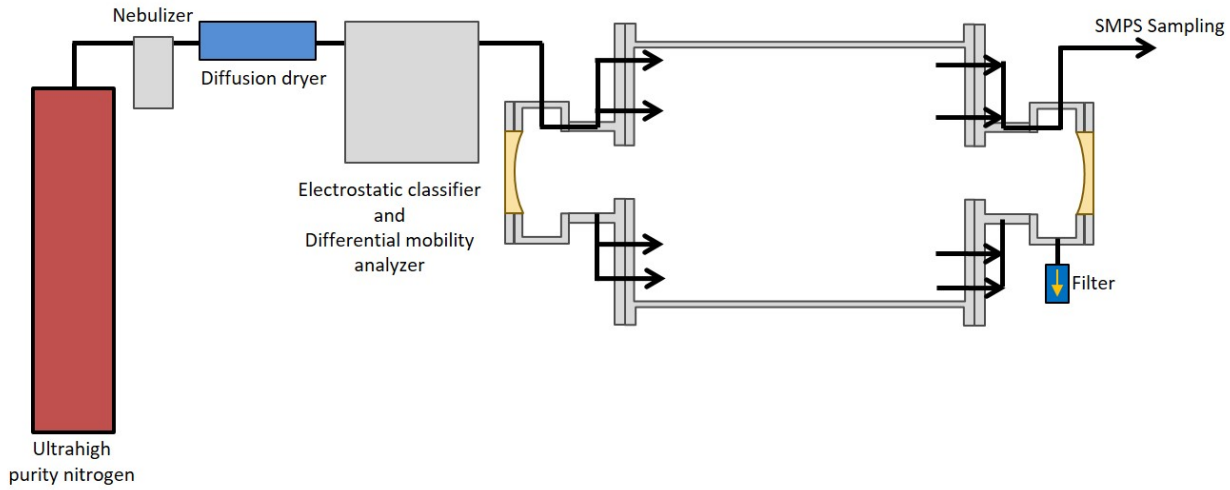

Figure 3.5: Experimental schematic for the introduction of monodisperse ammonium sulfate aerosols through the use of an electrostatic classifier and differential mobility analyzer. Schematic is not to scale.

3.3.1. Experimental Details

3.3.1.1. Materials

Certified ACS grade ammonium sulfate salt was purchased from Fisher Chemical. Research grade UHP N_2 was purchased from Praxair, Inc. The deionized water was acquired from Hahn Hall South (Millipore Purification Systems, 18.2 MΩ).

3.3.1.2. Particle Introduction

As previously described in Section 2.5, experiments began with spectroscopic and particle background measurements taken with the rotating chamber filled to atmospheric pressure with UHP N_2. For monodisperse aerosol introduction, 5 psi of UHP N_2 flowed through a Collison 6-jet nebulizer containing approximately 30 mL of 0.6833 g/L aqueous ammonium

sulfate solution. The newly generated salt aerosols flowed through a TSI 3062 diffusion dryer to remove excess water. Ammonium sulfate particles 90 nm in diameter were selected via an electrostatic classifier (TSI 3080) and long differential mobility analyzer (DMA, TSI 3081) set at 6.0 SLPM sheath flow rate and approximately 0.70 SLPM aerosol flow rate. The aerosol inlet tube leading to the electrostatic classifier had a valve with a Parker Balston filter (9922-05-CQ) open to laboratory air to reduce the aerosol flow rate into the electrostatic classifier. The 90 nm particles flowed into the chamber and a valve and filter attached to the tube extension opposite to aerosol introduction was opened to laboratory air to avoid over-pressurizing the main chamber. Particle introduction continued for 100 minutes.

3.3.1.3. Sampling Procedure

The nanoparticle suspensions were sampled through all four sampling ports simultaneously in triplicate every 20–60 minutes using an electrostatic classifier (TSI 3080), long differential mobility analyzer (DMA, TSI 3081) and water condensation particle counter (TSI 3782) in scanning mobility particle sizer (SMPS) mode. The DMA selects particles with a narrow range of electrical mobilities via an electric field created between the central tube and the outer wall of the column. The electrical mobility of a particle is determined by the terminal electrostatic velocity, which is related to the dynamic viscosity of the air, particle size, and charge (Equation A.6). The sample flowed into the SMPS at approximately 0.60 SLPM aerosol flow rate. Multiple charge and diffusion correction TSI algorithms were applied to each SMPS data set. The algorithms are described in detail by TSI Incorporated.[136] A port on the tube extension on the non-sampling side was opened to filtered laboratory air to maintain atmospheric pressure within the chamber during active sampling.

3.3.2. Suspension Efficiency

Number suspension efficiency alone was sufficient to understand the particle suspension characteristics for large, 1 μm PSLs in a rotating and stationary chamber. The monodisperse PSL experiments had low number concentrations (<2000/cm^3), thus the collisional frequen-

cies were too low to initiate coagulation and no condensable vapors were present to partition onto the particle surface. The particle number and volume concentrations of the PSLs were not affected by particle-particle interactions or the surrounding model atmosphere.

Ultrafine particles ($PM_{0.1}$) readily undergo coagulation and condensation in atmospheric conditions. Coagulation dramatically decreases the number concentration while the volume or mass concentration remains unchanged. Condensation, however, results in a higher particle mass or volume concentration with a stable particle number concentration. See Section 1.2.1.1 for more information on aerosol dynamics. A combination of V/V_o and N/N_o suspension efficiencies provided information on the aerosol dynamics over the course of an experiment, including coagulation, condensation, deposition and the effect rotation has on the overall suspension efficiencies of smaller, ammonium sulfate aerosols.

The 'monodisperse' salt aerosols generated by the electrostatic classifier and DMA column are not perfectly monodisperse, therefore V/V_o provides additional information necessary for the analysis of $PM_{0.1}$. The DMA filters the aerosol distribution for a specific mass-to-charge ratio on the assumption that the aerosols have one charge per aerosol after passing through a neutralizer. Some larger-than-desired aerosols pass through the neutralizer with multiple charges and enter the DMA, which allows the particles to pass through the column with smaller, singularly charged aerosols that have the same mass-to-charge ratio. Therefore, the electrostatic classifier did not generate a perfectly monodisperse suspension. The geometric standard deviations (σ_g) for the experiments described in this section are approximately 1.2, which is considered experimentally monodisperse.[16] The total volume along with total number suspension efficiency provided necessary information for analyzing the potential nanoparticle coagulation and condensation processes in the rotating chamber. Figure 3.6 represents the number and volume suspension efficiency for monodisperse, solid ammonium sulfate particles in the rotating chamber compared to a stationary chamber.

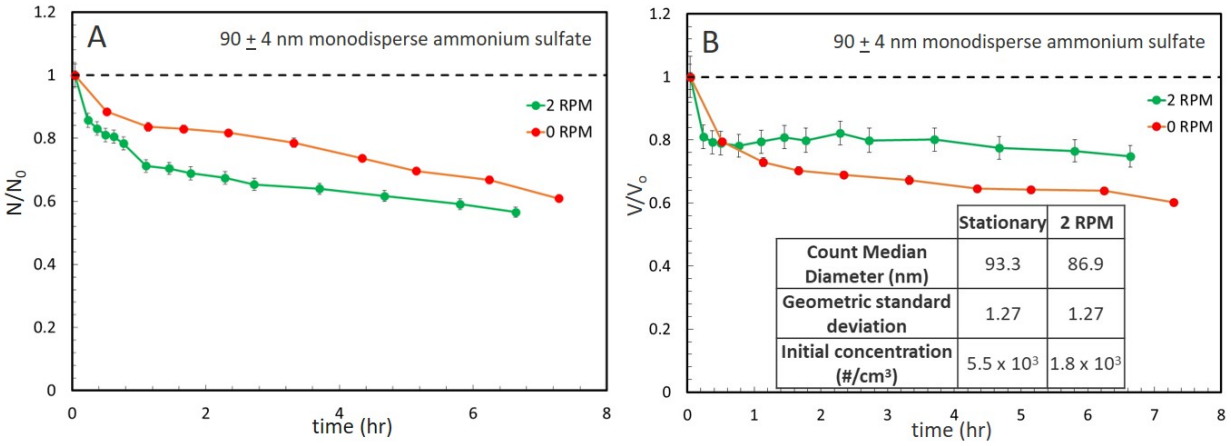

Figure 3.6: Long-term particle number (A) and volume (B) suspension efficiency (N/N_o and V/V_o, respectively) while the chamber rotated at 2 RPM (green) compared to a stationary chamber (red). The particles are 90±4 nm monodisperse ammonium sulfate particles and N_o was approximately 2–5 $\times 10^3/\text{cm}^3$. Each data point represents a sample taken in triplicate with the SMPS and was corrected for sample dilution caused by the particle sampling process (Equation 2.11). The lines were added to help guide the eye. Error bars represent absolute error of the average value, error bars smaller than the data point markers are not displayed. . The inset in Panel B provides the initial particle distribution characteristics for both experiments.

According to the computational model for aerosol dynamics explained in Sections 1.2.1.1, monodisperse, 0.1 μm particles at low concentrations ($<10^4/\text{cm}^3$) are expected to maintain a >50% number and volume suspension efficiencies for over 30 hours in both a rotating and stationary chamber (Equation 1.14). The concentrations of the particle suspensions represented in Figure 3.6 were too low to detect coagulation on the time scale of the experiments. Therefore, the number concentration and volume concentration remained stable over the course of the experiments. Both large, 1 μm, solid particles and ultrafine 90±4 salt particles follow the predicted suspension efficiencies described in Section 2.2.1 for a slowly rotating and stationary chamber.

3.4. Polydisperse Ammonium Sulfate Nanoparticles

Atmospherically-relevant particle suspension involve polydisperse aerosols of varying compositions and phases, not just monodisperse solid spheres, like PSLs. Previous Sections

3.2.2 and 3.3.2 described the initial particle dynamics and analysis techniques for monodisperse fine and ultrafine solid particles in the ACSI. The following experiments employed polydisperse, irregularly-shaped, ammonium sulfate particle suspensions at high number concentrations. High number concentrations (>10^5 particles/cm^3) result in higher collision frequencies that permit substantial coagulation over ~8 hour experiments. For example, a 100 nm particle suspension with 1000 particles/cm^3, the collisional frequency in the 222.4 L ACSI chamber is ~340 collisions/s while a 100 nm particle suspension with 1×10^5 particles/cm^3 will have 3.4×10^6 collisions/s (Equation 1.8). During coagulation, the number of small particles (<100 nm) decreases substantially as particles collide and adhere, which increases the number of larger particles. Overall, the total number concentration decreases due to coagulation, in agreement with Equation 1.14. No particle volume is lost during coagulation, therefore particle volume concentration remains unchanged (Equation 1.15).

$$\frac{dn_c}{dt} = \frac{N}{2}(8\pi d_p D N) = 4\pi d_p D N^2 \qquad \text{(1.8 revisited)}$$

$$N(t) = \frac{N_o}{1 + N_o \gamma \beta \overline{K} t} \qquad \text{(1.14 revisited)}$$

$$C_m = N_o \frac{\pi}{6} \rho_p d_o^3 = N(t) \frac{\pi}{6} \rho_p d(t)^3 \qquad \text{(1.15 revisited)}$$

Equation 1.21 was used to predict the calculated coagulation coefficient for the polydisperse ammonium sulfate distributions. The count median diameter (CMD) was used to determine the β correction factor.[21] A comparison between the calculated and experimental coagulation coefficient, using Equation 1.13, provided insight into the effect of rotation and other factors on particle coagulation rate. An experimental coagulation larger than the predicted $\beta\overline{K}$ results in γ greater than one and indicates external factors enhanced the coagulation rate. Conversely, a γ less than one implies a decrease in coagulation efficiency. The

determination of γ under different conditions for the same aerosol serves as a benchmark for identifying changes in aerosol dynamics in heterogeneous chemistry research with the ACSI.

$$\overline{K} = \frac{2k_bT}{3\eta}\left(1 + \exp(\ln^2\sigma_g) + \frac{2.49\lambda}{\mathrm{CMD}}[\exp(0.5\ln^2\sigma_g) + \exp(2.5\ln^2\sigma_g)]\right) \quad \text{(1.21 revisited)}$$

$$\frac{1}{N(t)} - \frac{1}{N_o} = \gamma\beta\overline{K}t \quad \text{(1.13 revisited)}$$

3.4.1. Experiment Details

3.4.1.1. Materials

Certified ACS grade ammonium sulfate salt was purchased from Fisher Chemical. Research grade UHP N_2 was purchased from Praxair, Inc. The deionized water was acquired from the Hahn Hall South facilities (Millipore Purification Systems, 18.2 MΩ).

3.4.1.2. Particle Introduction

The experiment began with background measurements described in Section 2.5. For polydisperse aerosol introduction, the rotating main chamber was evacuated to approximately 600 Torr. Twenty psi of UHP N_2 flowed through a Collison 6-jet nebulizer, which contained approximately 30 mL of 0.6833 g/L aqueous ammonium sulfate solution. The newly generated salt aerosols flowed through a diffusion dryer to remove excess water before introduction into the main chamber. Dried aerosol introduction continued until the chamber returned to atmospheric pressure.

Low ammonium sulfate aerosol concentration experiments followed a similar procedure as the one described above. The chamber was evacuated to 690–695 Torr prior to aerosol introduction. Aerosol introduction continued until the chamber returned to atmospheric pressure.

3.4.1.3. Sampling Procedure

The nanoparticle suspensions were sampled through all four sampling ports simultaneously in triplicate every 20–60 minutes using an electrostatic classifier (TSI 3080), long DMA (TSI 3081) and water condensation particle counter (TSI 3782) in scanning mobility particle sizer (SMPS) mode. The DMA selects particles with a narrow range of electrical mobilities via an electric field created between the central tube and the outer wall of the column. The electrical mobility of a particle is determined by the terminal electrostatic velocity, which is related to the dynamic viscosity of the air, particle size, and charge (Equation A.6). The sample flowed into the SMPS at approximately 0.60 SLPM aerosol flow rate. Multiple charge and diffusion correction TSI algorithms were applied to each SMPS data set. The algorithms are described in detail by TSI Incorporated.[136] A port on the tube extension on the non-sampling side was opened to filtered laboratory air to maintain atmospheric pressure within the chamber during active sampling.

3.4.2. Suspension Efficiency and Coagulation Analysis

Polydisperse distribution total number (N/N_o) and volume (V/V_o) suspension efficiencies were used to compare the aerosol dynamics in the rotating and stationary experiments, similar to the analysis used for the ultrafine monodisperse particle suspensions. Most of the following experiments employed approximately 2–3 orders of magnitude more particles than the monodisperse studies, which resulted in ~4–6 orders of magnitude higher collision frequency between particles in the chamber (Equation 1.8). Higher concentrations and collision frequencies necessitate a closer inspection of the suspension efficiencies to evaluate the aerosol dynamics for a complex particle suspension. According to aerosol dynamics, each collision results in two particles sticking together, which lowers the number concentration while the particle volume concentration remains unchanged. Therefore, number suspension efficiency alone would not be adequate to determine the effect of the chamber rotation on the particle suspension due to changes over time from particle coagulation. The following

section will explore the effects of particle concentration, rotation, and other external factors on coagulation rate for a polydisperse solid particle in a simple model atmosphere of dry nitrogen gas.

The polydisperse total number suspension efficiency (N/N_o) is expected to drop significantly due to coagulation within the first hour, (Equation 1.14). For example, the number suspension efficiency for a polydisperse suspension with $1{\times}10^6$ particles/cm^3, CMD of 70 nm, and σ_g of 1.7, will decrease the number concentration by half in approximately 12 minutes. Lower concentrations and corresponding lower collision frequencies result in less change in the number concentration over time, which was shown experimentally in both the fine (PSL) and ultrafine (ammonium sulfate) monodisperse experiments described in Sections 3.2.2 and 3.3.2. Figure 3.7 represents the number and volume suspension efficiencies for polydisperse ammonium sulfate particles in the rotating chamber compared to a stationary chamber.

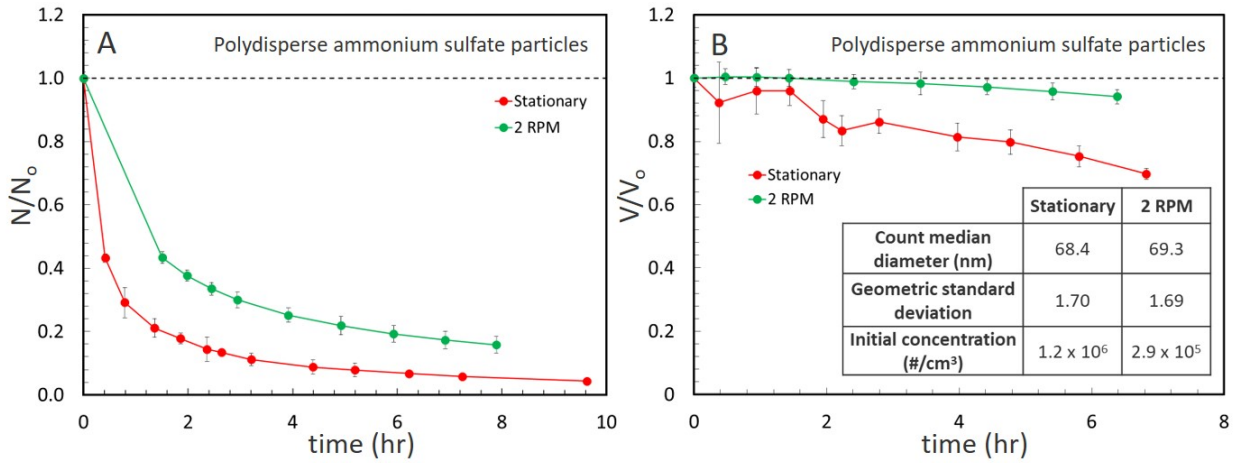

Figure 3.7: Long-term polydispserse ammonium sulfate suspension total number (N/N_o, A) and total volume (V/V_o, B) suspension efficiency while the chamber rotated at 2 RPM (green) compared to a stationary chamber (red). Each data point represents a sample taken in triplicate with the SMPS and was corrected for sample dilution caused by the particle sampling process (Equation 2.11). The lines were added to help guide the eye. Error bars represent absolute error of the average value, error bars smaller than the data point markers are not displayed. The inset in Panel B provides the initial particle distribution characteristics for both experiments.

The immediate decline in particle number concentration decline for the stationary and

2 RPM trials supported the hypothesis that polydisperse suspensions undergo coagulation at high concentrations in the ACSI. The volume suspension efficiency over time, however, was slightly different between the experiments. The 2 RPM experiment maintained almost 100% volume suspension efficiency while the particle volume concentration in the stationary experiment diminished 40% after 8 hours. The decline in total particle volume concentration for the stationary chamber trial suggests that some particles were lost to deposition as coagulation progressed. A low particle concentration study (<1000 particles/cm^3) provided information on polydisperse particle deposition within the rotating chamber. Any decrease in particle number recorded in a low particle concentration is most likely due to deposition, rather than from coagulation.[22] Figure 3.8 includes the number and volume suspension efficiencies for the low concentration trial as well as those depicted in Figure 3.7.

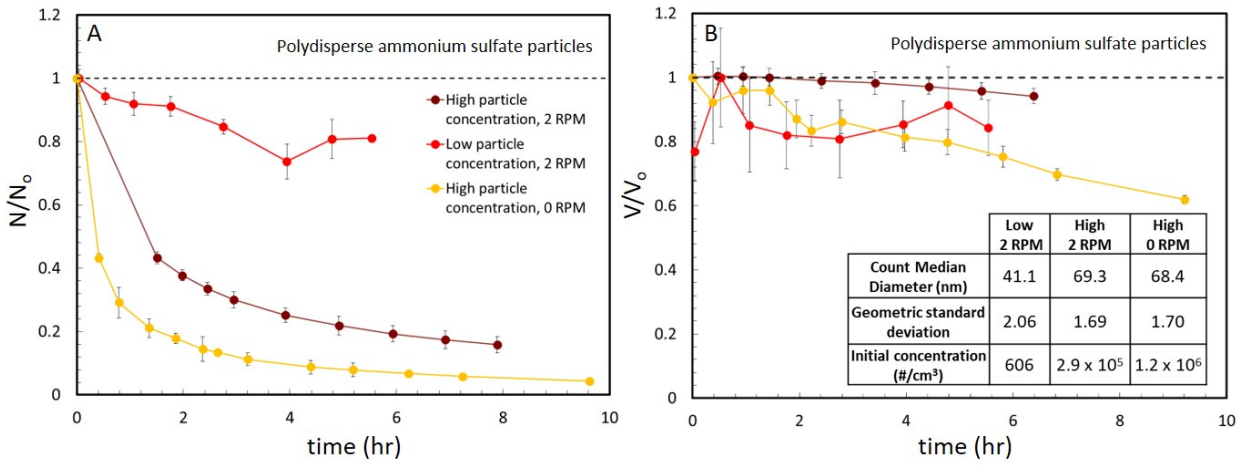

Figure 3.8: A) Number suspension efficiency (N/N_o) for high initial ammonium sulfate aerosol concentration while the chamber rotated at 2 RPM (dark red), 0 RPM (yellow), and low initial ammonium sulfate aerosol concentration (red). B) Volume suspension efficiency (V/V_o) for high initial ammonium sulfate aerosol concentration while the chamber rotated at 2 RPM (dark red), 0 RPM (yellow), and low initial ammonium sulfate aerosol concentration (red). Each data point represents a sample taken in triplicate with the SMPS and was corrected for sample dilution caused by the particle sampling process (Equation 2.11). The lines were added to help guide the eye. Error bars represent absolute error of the average value, error bars smaller than the data point markers are not displayed. The inset in Panel B provides the initial particle distribution characteristics.

Figure 3.8 indicates negligible particle loss in the rotating chamber for low particle

concentrations. Both the number and volume suspension efficiency remained stable for the low concentration ($<10^4$ particles/cm^3) trial while the high concentration studies (10^6 particles/cm^3) exhibited dramatic particle loss, likely from coagulation. In order to confirm particles coagulated in the high concentration studies, the particle number suspension efficiency was analyzed for 6–8 particle sizes throughout the particle distributions for all three trials. A particle suspension that experiences coagulation should show a sharp decrease in the number of small particles and an increase in larger particles as aggregates are formed. No or minimal coagulation is hypothesized for the low concentration trial, which should result in no discernible trends for each particle size. Figure 3.9 shows the number suspension efficiencies for 6–8 particle sizes from all three experiments shown Figure 3.8.

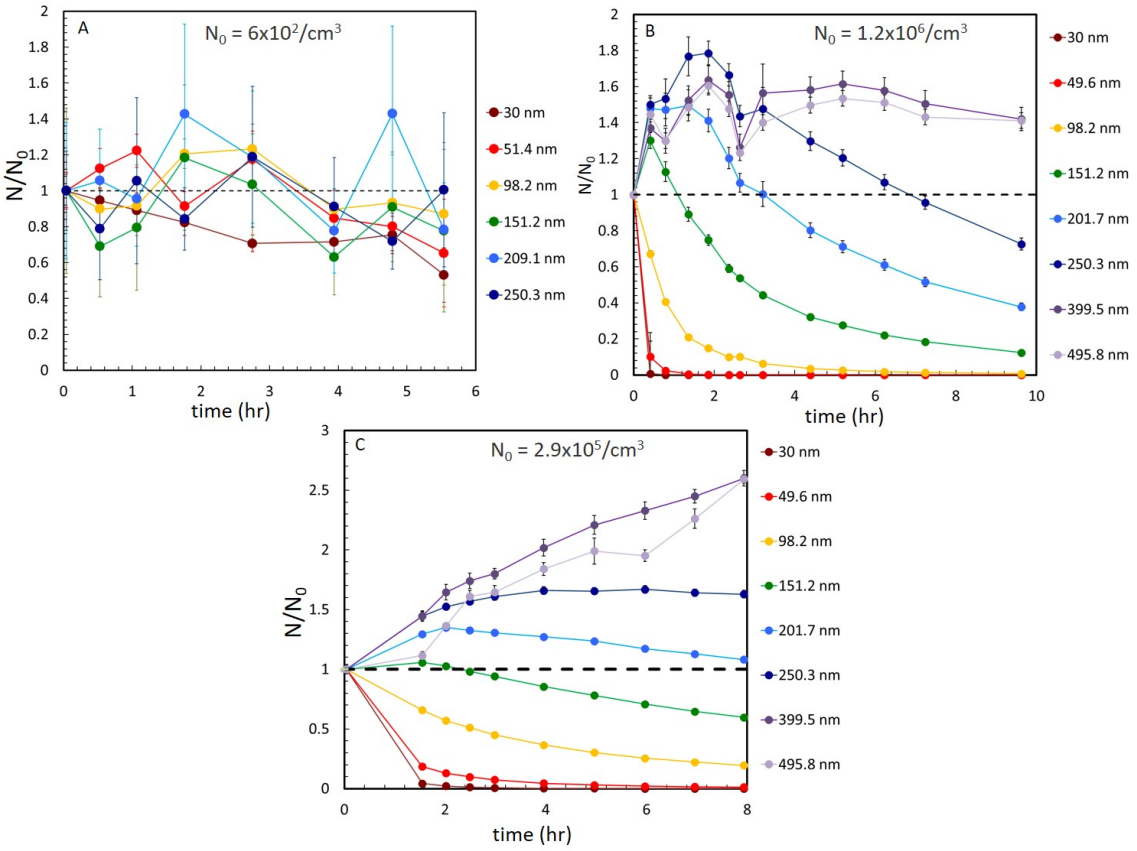

Figure 3.9: Number suspension efficiency (N/N_o) for different particle sizes for low initial ammonium sulfate aerosol concentration while the chamber rotated at 2 RPM (A), high initial ammonium sulfate aerosol concentration in a stationary chamber (B), high initial ammonium sulfate aerosol concentration while the chamber rotated at 2 RPM (C). Each data point represents a sample taken in triplicate with the SMPS and was corrected for sample dilution caused by the particle sampling process (Equation 2.11). The lines were added to help guide the eye. Error bars represent absolute error of the average value, error bars smaller than the data point markers are not displayed.

Figure 3.9A suggests no coagulation or particle loss occurred in the low concentration particle suspension because the number suspension efficiency in the did not exhibit discernible upward or downward trends in the rotating ACSI for all six particle sizes. Figure 3.9B showed a rapid initial decrease in small particle concentration ($\leq$ 98.2 nm) and a corresponding increase in larger particles for the stationary trial, which suggests the high particle concentration permitted the formation of aggregates through coagulation. However, the large particle concentration began to drop after approximately 2 hours. Similar trends in the high

concentration, rotating trial indicated coagulation, except the newly formed large particles remained suspended over the course of the experiment.

Computational models and experimental data shown in Figure 3.8 and Figure 3.9 indicated measurable coagulation within 8 hours depended on the initial concentration of the polydisperse suspensions. The low concentration trial (<1000 particles/cm^3) did not change appreciably over time, which is likely due to low collisional frequency (~300/s) and minimal gravitational deposition.[16,22,137] In the stationary experiment, the larger, newly formed aggregates were lost to gravitational settling after approximately 2 hours, which coincides with the decrease in total number and volume suspension efficiency shown in Figure 3.8. A steady total volume concentration and the trends seen for different particle sizes implied that rotating the chamber kept the new aggregates suspended as coagulation progressed.

The derivation for the size-corrected coagulation coefficient ($\beta\overline{K}$, Equation 1.21) described in Section 1.2.1.1 assumed ideal conditions that are not representative of real experimental conditions. Therefore, calculating experimental coagulation coefficient ($\gamma\beta\overline{K}$) provided insight on how the particle type, phase, and model atmosphere affect aerosol dynamics. A method outlined by Kim et al. determined the experimental coagulation coefficient for high particle concentrations.[22] A plot of Equation 1.13 and experimental data resulted in a straight line with a slope of $\gamma\beta\overline{K}$, where the scalar, γ, is used to fit the experimental data to the calculated coagulation coefficient. A scalar larger than 1 indicates the coagulation is enhanced compared to the derivation outlined in Section 1.2.1.1, while a γ less than one suggests the coagulation is negatively impacted by experimental conditions. Figure 3.10 depicts the data analysis process for determining $\gamma\beta\overline{K}$ for a high particle concentration in a rotating chamber.

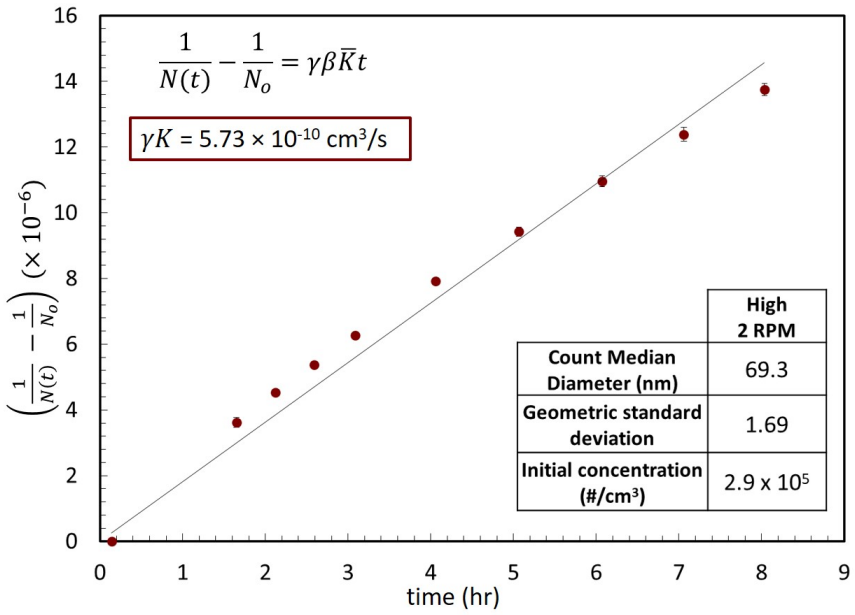

Figure 3.10: Plot depicting the data analysis used to determine the $\gamma\beta\overline{K}$ for the high concentration polydisperse distribution coagulating in a rotating chamber. The product, $\gamma\beta\overline{K}$, is the slope of the line with the intercept set to zero according to the equation in the figure and the method developed by Kim et al..[22] The red outlined inset provides the calculated $\gamma\beta\overline{K}$. The black outlined inset provides the initial particle distribution characteristics. Error bars represent absolute error of the average value, error bars smaller than the data point markers are not displayed.

The difference between the experimental and calculated coagulation coefficients provides insight into the enhancement or reduction of particle coagulation in a model atmosphere. The slope of the line in Figure 3.10 ($\gamma\beta\overline{K}$) was substituted to in Equation 1.14, which was then compared to the number suspension efficiency for both experiments previously reported (Figure 3.11). The calculated change in particle number concentration over time agreed with the experimental data. Initial distribution characteristics for the high concentration suspensions were used to calculate the size-corrected coagulation coefficient ($\beta\overline{K}$, Equation 1.21). The scalar, γ, is determined using the calculated $\beta\overline{K}$ and the experimental $\gamma\beta\overline{K}$.

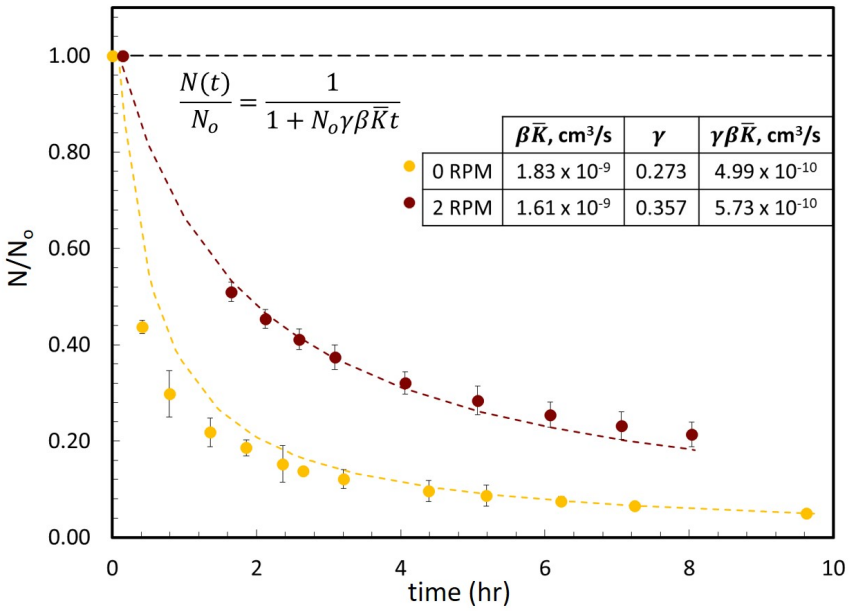

Figure 3.11: Experimental and calculated number suspension efficiency (N/N_o) for high initial ammonium sulfate aerosol concentration while the chamber rotated at 2 RPM (dark red) and 0 RPM (yellow). Each data point represents a sample taken with the SMPS. Error bars represent absolute error of the average value, error bars smaller than the data point markers are not displayed. The dotted traces represent the calculated decrease in number concentration using experimental coagulation coefficients, $\gamma\beta\overline{K}$. The inset provides the size-corrected coagulation coefficient ($\beta\overline{K}$), sticking coefficient (γ), and the product of $\gamma\beta\overline{K}$.

Both trials resulted in a γ less than one, which implies the coagulation measured in the experiment is not as fast or as efficient as predicted by computational models. The particle suspension in a stationary chamber had a much lower γ than a comparable particle suspension in a rotating chamber. Therefore, the lower γ indicates a less efficient coagulation in the stationary chamber when compared to the chamber rotating at 2 RPM. The coagulation derivation described in Section 1.2.1.1 neglected experimental factors, such as turbulence, particle surface charge, shape, and phase, that could affect coagulation efficiency.

Kim et al. reported coagulation coefficients 20–70% larger than the calculated $\beta\overline{K}$ for similarly-sized, polydisperse NaCl salt particles ($\gamma > 1$), unlike the scalars calculated for the ammonium sulfate suspensions that are all less than one.[22] Particle surface charge could explain the discrepancy between the experiments described in this chapter and those previously

reported for NaCl.[22] My experiments only dried the aerosol-laden flow prior to introduction while Kim et al. dried and neutralized most of the particle surface charge with a Kr-85 neutralizer.[22]

Surface charge affects coagulation in a few ways: diminish coagulation due to the repulsion of like surface charges,[138] coagulation enhancement from strongly bipolar surface charges, negligible changes when particles exhibit a Boltzmann equilibrium charge distribution, and coagulation enhancement from the formation of chain-like aggregates.[16] At equilibrium, approximately 28.7% of 100 nm particles are expected to have at least one elementary charge unit on the particle surface (Equation A.21).[16] Figure 3.12 displays the computed fraction of particles between 10–1000 nm with 1 to 5 elementary charges. Hinds states that neutral particles will acquire charge over time from collisions with air molecules and other particles.[16] In addition, Kim et al. reported that high concentrations of similar surface charges stabilized particle suspensions and decreased coagulation.[138] The introduction of aerosols directly from the drier without neutralization most likely resulted in particles with surface charge.

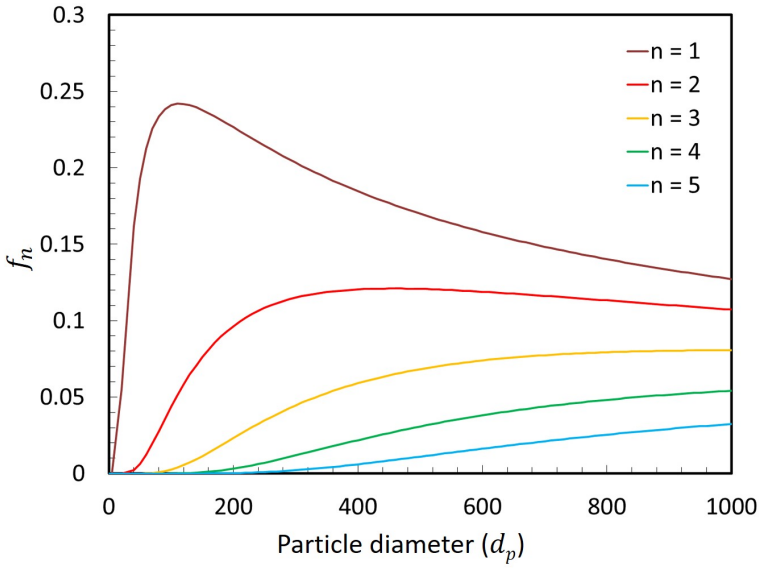

Figure 3.12: Boltzmann's equilibrium charge distribution for ultrafine and fine particulate matter for $n = 1$–5 elementary charges.

The coagulation derivation described in Section 1.2.1.1 also assumed hard, spherical particles, instead of an irregularly-shaped, effloresced salt particles. The ammonium sulfate in the experiments above existed as solid salt particles because the aerosol-laden flow was dried and introduced into the ACSI with humidity lower than ammonium sulfate efflorescence relative humidity. See Section 3.5 for more information on the efflorescence and deliquesence of hygroscopic materials. Irregular particle shapes increase the coagulation coefficient when compared to spherical particles. For example, Zebel reported that ellipsoids with a 10:1 radius ratio enhanced the coagulation coefficient ($\overline{K}$) by 35% when compared to a spherical particle with the same volume.[16,25] If the irregularity of the particle shape affected the coagulation in the ammonium sulfate experiments, the scalar, γ, would have been greater than 1, which indicates an increased experimental coagulation coefficient when compared to $\beta\overline{K}$. Future studies involving scanning electron microscopy will show the extent of irregularity in particulate shapes and how the geometry depends on experimental parameters.

Fractal aggregates and turbulence are factors other than shape and surface charge that alter the coagulation. Fractal aggregates occur when solid particles collide and form long linear chains instead of uniform spherical droplets. Fractal aggregates enhance the coagulation rate.[16] Turbulence and non-ideal flow patterns in the rotating chamber increases the number of collisions between particles,[16] thus enhancing coagulation in a rotating chamber relative to a stationary chamber. However, turbulent coagulation only affects particles larger than 10 μm.[16,22,137] Turbulent coagulation is negligible for $PM_{2.5}$ even though the environment within the rotating chamber is turbulent and the sampling procedure causes turbulence as the samples flow through the tubing.

Non-ideal flows enhance coagulation due to increased particle collisional frequencies in turbulent environments.[16] The flow environment within the chamber is considered non-ideal because of the chamber rotation and sampling procedure. Figure 3.13 shows the calculated velocity contours for tangential, radial and axial velocities in m/s with the chamber rotating at 2 RPM, determined by our collaborator Matt Brown at Clarkson University. Frostling was

the first, to my knowledge, to describe particle distributions within a cylindrical, rotating chamber intended to extend particle suspension durations.[128] The distributions reported only had 6 channels for particle sizes between 0.3–3 μm. In comparison, the SMPS used for all of the ammonium sulfate experiments employs 108 channels between ~20–700 nm, which resulted in a more resolved distribution for every sample collected. The distributions reported by Frostling involve much larger particles than the ammonium sulfate distributions and hypothesized the decrease in particle number concentration is due to coagulation.[128] The analytical solution for polydisperse coagulation coefficients was developed by Lee and Lee and Chen after the Frostling paper was published.[16,23,24,128] Therefore, the prior work reported a calculated coagulation coefficient, which disagrees with current computational models.

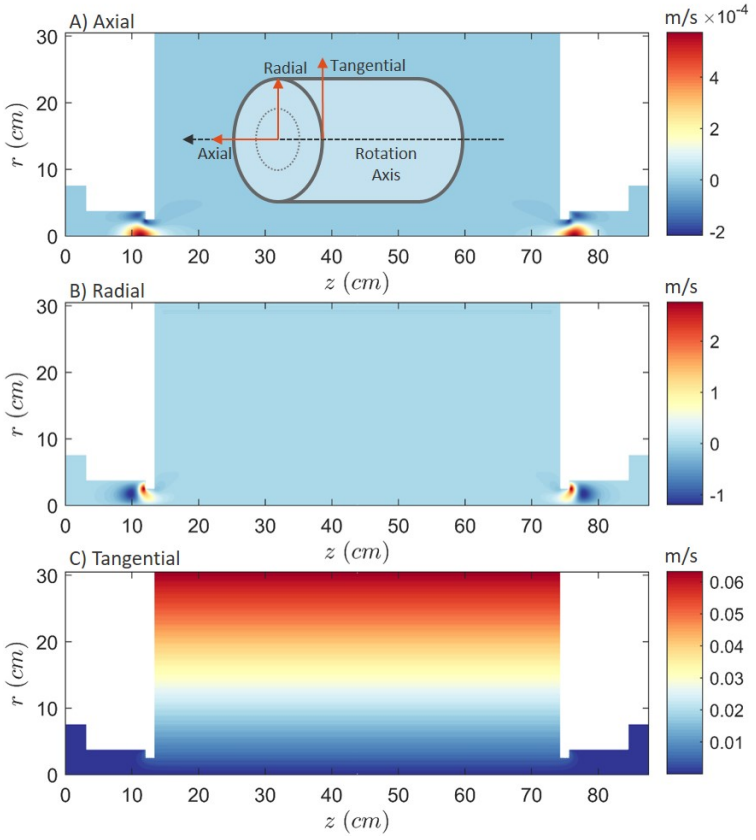

Figure 3.13: Calculated velocity contour within the ASCI, rotating at 2 RPM. The color scale units are m/s for all three contours. Our collaborator at Clarkson University, Matthew Brown, performed the simulations for the figure.

In conclusion, the experimental ammonium sulfate coagulation coefficients were both lower than the calculated $\beta\overline{K}$. There are multiple, well-known factors that affect coagulation rates: the formation of chain-like fractal aggregates, non-ideal turbulent flows, shape, and surface charge. Non-ideal flows, fractal aggregates, and irregular particle shapes all increase coagulation rate. Therefore, those factors are likely not the cause of the difference between the calculated and experimental coagulation coefficients. Surface charge is one of the only plausible explanations for an experimental coagulation coefficient to be less than predicted.[16,138] As mentioned above, the experimental set-up used for these experiments could not neutralize the particles prior to introduction to investigate the relationship between surface charge and coagulation rate for particles with the same composition and phase state.

3.5. Effect of Humidity and Particle Composition on Aerosol Coagulation

Humidity and particle composition affect atmospheric lifetimes of particulate matter, especially in hygroscopic inorganic salt particles. Approximately 81 Tg of sulfur and over 21 Tg of nitrogen are emitted into the atmosphere each year from both anthropogenic and natural sources.[13,29,30,33] Sulfur and nitrogen-containing molecules oxidize in the atmosphere to form molecules such as sulfuric acid (H_2SO_4) and nitric acid (HNO_3). Atmospheric acids and bases react to form secondary ammonium sulfate and other water-soluble, inorganic salt aerosols. Acidic compounds incorporated onto aerosols are not always chemically neutralized by available basic gases,[86] which results in compounds like ammonium bisulfate (NH_4HSO_4) and highly acidic particles (pH < 1).[139,140] Youn et al. collected $PM_{1.0}$ in the Southwest United States and reported NH_4^+:SO_4^{2-} ratios less than 2:1, indicating some of the sulfate was not chemically neutralized by the available basic amines in the atmosphere.[86] Therefore, natural inorganic salt particles consist of complex mixtures, including acidic compounds. The following section employs the ACSI to explore the effect of particle phase state and composition on aerosol dynamics, specifically coagulation.

Acidic particles also facilitate heterogeneous reactions between the particle and surround-

ing gases. Nozière et al. reported that inorganic salt ions, such as ammonium and carbonate, catalyze aldol condensation reactions, which ordinarily require strong acid or base catalysts.[74] Acidic particles contribute to particle growth during new particle formation events through acid-base reactions with amines and basic gases.[1] For example, ammonium bisulfate (NH_4HSO_4) particles react with gaseous alkyl amines without displacing ammonia within the particle.[99] In contrast, chemically neutralized ammonium sulfate ($(NH_4)_2SO_4$) particles release ammonia when exposed to more basic, less volatile alkyl amines.[86,99,100,141] Aerosol acidity affects the known heterogeneous reactions and hygroscopicity of atmospheric particles.[72]

All aerosols and reactive gases in the atmosphere also interact with water. Atmospheric water exists as water vapor (humidity), liquid (droplets or coatings around existing particles), and solid (ice particles). The particle phase of hygroscopic material depends on aerosol composition and the relative humidity of the surroundings.[72,131] Inorganic salts exist either as solid salt crystals at low relative humidity or aqueous droplets at high relative humidity. The following section focuses on the phase state of H_2SO_4, NH_4HSO_4, and $(NH_4)_2SO_4$ at various relative humidities.

At extremely low relative humidities, most inorganic salt particles exist as solid crystals.[131] The particle remains solid until the characteristic deliquescence humidity (DRH), at which point the particle spontaneously forms a saturated aqueous droplet. A continued increase in humidity past the DRH results in water adsorption onto the aqueous droplet, increasing the size of the aerosol. An aqueous droplet develops into a supersaturated droplet when the relative humidity decreases below the DRH. The droplet remains aqueous until the efflorescence relative humidity (ERH) is reached, at which point the droplet recrystallizes back into a solid salt particle. Highly hygroscopic species, like sulfuric acid and ammonium bisulfate, do not effloresce—instead, the aerosol changes smoothly with fluctuating relative humidity.[129,131,139] Figure 3.14 shows the change in aerosol diameter for H_2SO_4, NH_4HSO_4, and $(NH_4)_2SO_4$ at different relative humidities. Notice the sharp increase in aerosol diam-

eter for ammonium sulfate at the 80% RH (DRH) and decrease at 35% RH (ERH).[129–131] Assuming the particles passing through the diffusion dryer do not effloresce prior to introduction into the chamber, the ammonium sulfate particles existed as supersaturated aqueous droplets at 45–50% RH.[129,131]

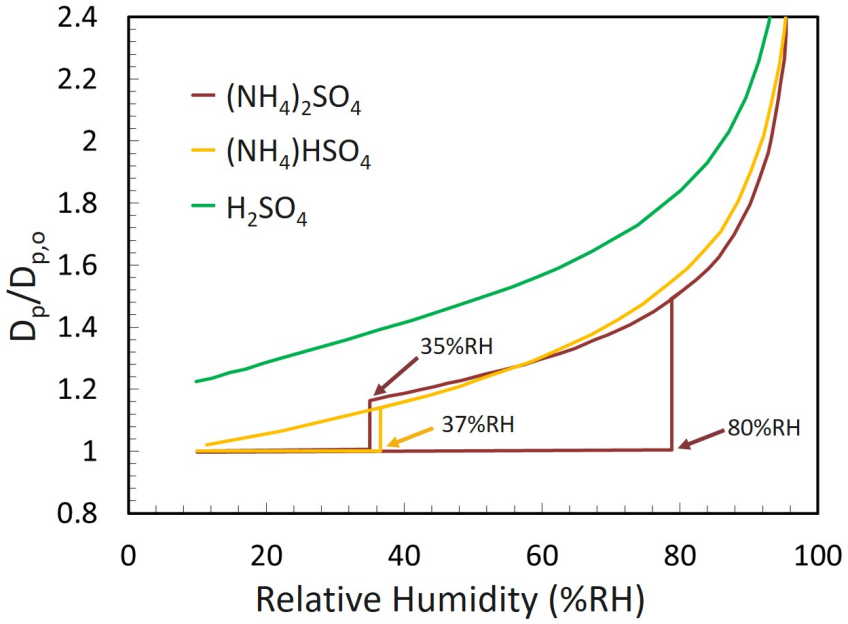

Figure 3.14: Diameter change of ammonium sulfate, ammonium bisulfate, and sulfuric acid as a function of relative humidity. $D_{p,o}$ is defined as the diameter of the particle at 0% RH. This figure adapted from reference 131.

The three humidities explored in the following sections are <15% RH, ~30% RH, and >50% RH. Therefore, ammonium sulfate particles are expected to be solid at <15% RH, solid with some water vapor or a liquid water layer on the particle at ~30% RH, and aqueous salt droplets at >50% RH. As the particle composition changed through the addition of sulfuric acid to the seed solution, the acidic particles are assumed to exist as aqueous, ammonium bisulfate/sulfuric acid salt droplets at all relative humidities. The following section explores the effect of humidity, particle composition, and particle phase on aerosol dynamics of inorganic salts. Similar techniques described in Section 3.4.2 were used to analyze polydisperse particle suspension characteristics for each model atmosphere.

3.5.1. Experimental Details

3.5.1.1. Materials

Certified ACS grade ammonium sulfate salt was purchased from Fisher Chemical. Certified ACS grade sulfuric acid was purchased from Spectrum Chemical. Research grade UHP N_2 was purchased from Praxair, Inc. The deionized water was acquired from the Hahn Hall South facilities (Millipore Purification Systems, 18.2 MΩ). HPLC grade, submicron filtered water used for humidity control was purchased from Fisher Chemical.

3.5.1.2. Particle Introduction

The experiment began with background measurements described in Section 2.5. Water vapor was added until the relative humidity reached the desired level using the procedure in Section 2.5.1.1. For polydisperse aerosol introduction, the rotating main chamber was evacuated to approximately 600 Torr. Twenty psi of UHP N_2 flowed through a Collison 6-jet nebulizer containing approximately 40 mL of 0.6833 g/L aqueous ammonium sulfate solution (pH ~5.5). The newly generated salt aerosols flowed through a TSI 3062 diffusion dryer to remove excess water before introduction into the main chamber. Aerosol introduction continued until the chamber returned to atmospheric pressure.

Sulfuric acid was added to the ammonium sulfate seed solution to generate the acidic particles. The seed solution acidity was increased until the pH reached ~2.5 for one trial and ~1.5 pH for the second. The acidic seed solutions are assumed to contain a mixture of ammonium sulfate, ammonium bisulfate, and sulfuric acid.

3.5.1.3. Sampling Procedure

The nanoparticle suspensions were sampled through all four sampling ports simultaneously in triplicate every 20–60 minutes using an electrostatic classifier (TSI 3080), long DMA (TSI 3081) and water condensation particle counter (TSI 3782) in scanning mobility particle sizer (SMPS) mode. The DMA selects particles with a narrow range of electrical mobilities via an electric field created between the central tube and the outer wall of the column. The

electrical mobility of a particle is determined by the terminal electrostatic velocity, which is related to the dynamic viscosity of the air, particle size, and charge (Equation A.6). The sample flowed into the SMPS at approximately 0.60 SLPM aerosol flow rate. Multiple charge and diffusion correction algorithms from TSI were applied to each SMPS data set. The algorithms are described in detail by TSI Incorporated.[136] A port on the non-sampling tube extension was opened to filtered laboratory air to maintain atmospheric pressure within the chamber during active sampling.

3.5.2. Suspension Efficiency and Coagulation Analysis

As described in Section 3.4.2, the total number and volume suspension efficiencies were used to explore the changes in aerosol dynamics for the polydisperse ammonium sulfate particles at different relative humidities. Figure 3.16 displays the suspension efficiencies for four trials: 1.6% RH, 16.7% RH, 45.7% RH, and 49.8% RH initial relative humidity.

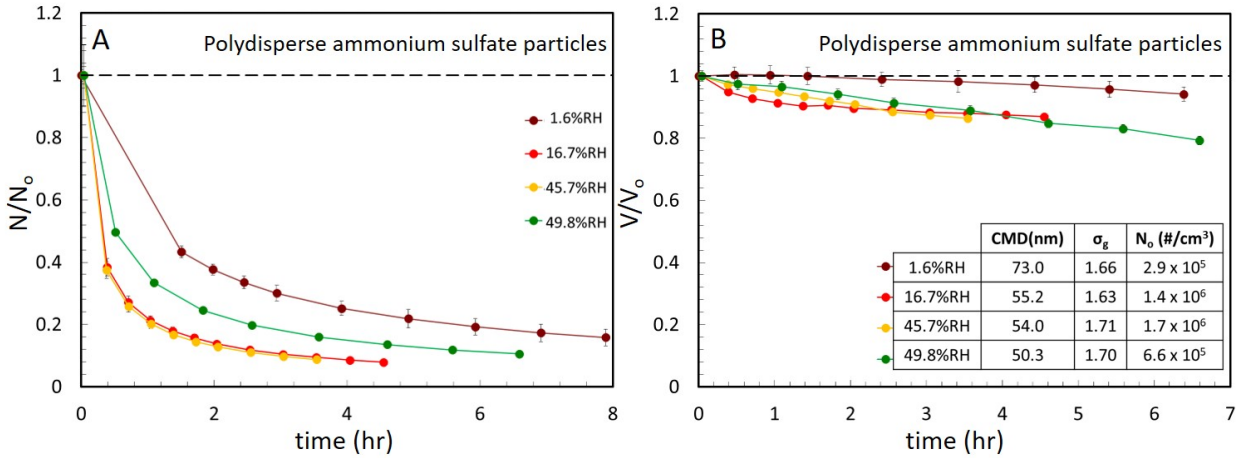

Figure 3.15: A) Ammonium sulfate number suspension efficiency (N/N_o) at 1.6% RH (dark red), 16.7% RH (red), 45.7% RH (yellow), and 49.8% RH humidity (green) while the chamber rotated at 2 RPM. B) Ammonium sulfate volume suspension efficiency (V/V_o) at 1.6% RH (dark red), 16.7% RH (red), 45.7% RH (yellow), and 49.8% RH humidity (green). Each data point represents a sample taken in triplicate with the SMPS and was corrected for sample dilution caused by the particle sampling process (Equation 2.11). The lines were added to help guide the eye. Error bars represent absolute error of the average value, error bars smaller than the data point markers are not displayed. The inset in Panel B provides the initial particle distribution characteristics.

The three trials with humidity >15% RH resulted in a quicker decrease in particle number concentration compared to the very low humidity trial (1.6% RH). Volume suspension efficiencies indicate the loss of some particles for the 16.7% RH, 45.7% RH, and 49.8% RH trials. The polydisperse ammonium sulfate particles in a rotating chamber at any relative humidity exhibit a higher volume suspension efficiency when compared to the particle suspension in a stationary chamber at <5% RH (Figure 3.8). The number suspension efficiency shown in Figure 3.15 quickly decreases while the volume suspension efficiency (V/V_o) remained stable, which suggests the aerosols coagulated during the experiment.

The coagulation of two same-sized, aqueous droplets results in a droplet with twice the volume but a radius only ~26% larger. In contrast, the coagulation of two same-sized, solid particles results in a particle with an effective diameter twice as large as the original particles. Therefore, if the particles are aqueous droplets at approximately 50% RH, the increase in the number of large particles would not be as apparent as in the low humidity experiments. I hypothesize that the aqueous aerosols in the 45.7% RH and 49.8% RH trials will exhibit a limited increase for the N/N_o of larger sized particles compared to the coagulation of solid particles in the experiments <16.7% RH. Figure 3.16 shows the number suspension efficiency for different sized particles at each humidity over time and provides insight into a possible explanation for the lower total volume suspension efficiency highlighted in Figure 3.15.

The different-sized particle suspension efficiencies depicted in Figure 3.16 suggest that as humidity increases, the larger particles do not increase in number significantly as the suspension coagulates. The 16.7% RH trial exhibited similar trends in different particle sizes compared to the 1.6% RH experiment. The number of larger particles increased while the smallest particles decreased rapidly after particle introduction, indicative of coagulation. Although the trends are similar between the 1.6% RH and the 16.7% RH trials, the number of larger particles did not increase as dramatically in the 16.7% RH as in the 1.6% RH trial. The 45.7% RH and 49.8% RH trials showed almost no increase in the number of large particles over the course of the experiment. Small particles still decreased over time, similar

to the experiments known to coagulate at relative humidities <10% RH. The lack of increase in larger particles in the experiments with >35% RH could be due to unaccounted particle loss, particle phase, or a combination of factors. I hypothesize that the salt ions move freely throughout aqueous droplets, which can result in enhanced ionic concentrations on particle surfaces. An enhanced concentration of one ion could negatively impact coagulation through repulsive forces.

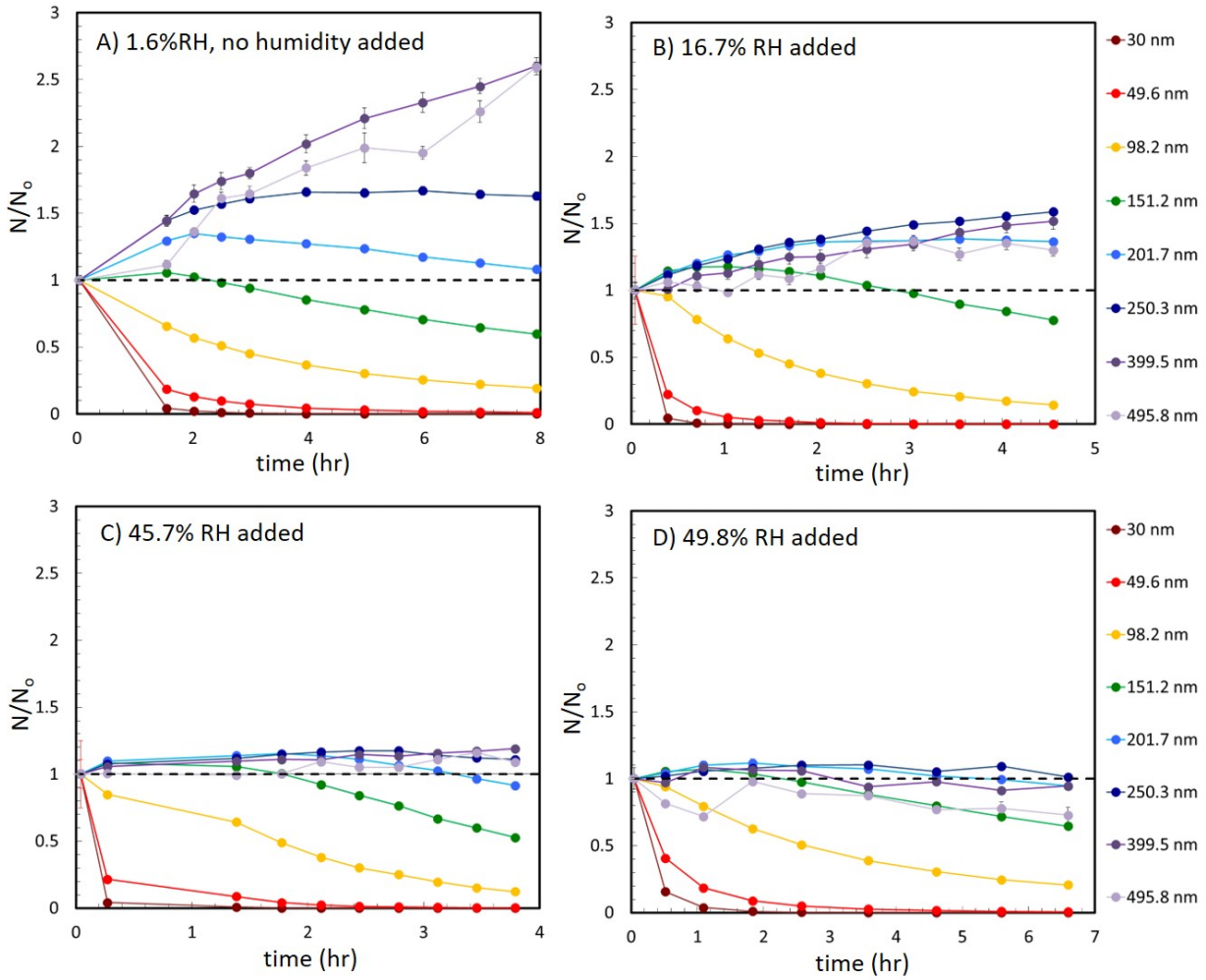

Figure 3.16: Number suspension efficiency (N/N_o) for different particle diameters for ammonium sulfate aerosol with A) 1.6% RH (no added humidity), B) 16.7% RH, C) 45.7% RH, and D) 49.8% RH while the chamber rotated at 2 RPM. Each data point represents a sample taken in triplicate with the SMPS and was corrected for sample dilution caused by the particle sampling process (Equation 2.11). The lines were added to help guide the eye. Error bars represent absolute error of the average value, error bars smaller than the data point markers are not displayed.

The experimental coagulation coefficient was calculated for the ammonium sulfate suspensions to compare the sticking coefficient, γ, at each relative humidity. Equation 1.13 was fit to the total number suspension efficiency for each trial to determine the experimental coagulation coefficient, $\gamma\beta\overline{K}$. The calculated coagulation coefficient, $\beta\overline{K}$, was also determined for each trial. The scalar, γ, was calculated from the difference between the calculated and experimental coagulation coefficients using the analysis discussed in Section 3.4.2. Table 3.3 lists the coagulation coefficients and the scalar for the 1.6% RH, 16.7% RH, 45.7% RH, and 49.8% RH experiments.

Table 3.3: Comparison between the calculated ($\beta\overline{K}$) and experimental coagulation coefficients ($\gamma\beta\overline{K}$) for ammonium sulfate particles at different relative humidities.

Initial Humidity	$\beta\overline{K}$ **(cm^3/s)**	γ	$\gamma\beta\overline{K}$ **(cm^3/s)**
1.6% RH	1.61×10^{-9}	0.357	5.73×10^{-10}
16.7% RH	1.77×10^{-9}	0.318	5.65×10^{-10}
45.7% RH	1.93×10^{-9}	0.280	5.40×10^{-10}
49.8% RH	1.96×10^{-9}	0.295	5.78×10^{-10}

The experimental coagulation gradually decreases in efficiency, i.e. the scalar (γ) decreases, with increasing humidity. The presence of 16–50% water vapor negatively impacted coagulation for ammonium sulfate when compared to the particle suspension coagulation in 1.6% RH. As described in Section 3.5, the ammonium sulfate particles most likely exist as aqueous droplets above 35% RH, the characteristic efflorescence humidity. Therefore, ammonium sulfate aerosols in the 45.7% RH and 49.8% RH experiments are assumed to be droplets, not solid salt particles.

Ault et al. reported that an aqueous mixture of typical sea salt ions form "heterogeneous internal structures" upon reaction with nitric acid, including an enhanced cation concentration the particle surface.[142] The ammonium sulfate particles are inherently acidic (seed solution had a pH of 5.5), therefore the ions could form ionic layers in the aqueous ammonium

sulfate droplets, similar to the internal aerosol structures discovered by Ault et al..[142] The positively charged ion concentration could be enhanced on the aerosol surface. Increased concentrations of like-charged ions on the particle surface result in Coulombic repulsion forces between particles, which decreases the coagulation efficiency.[138] Slower coagulation caused the repulsion of particles with like surface charges supports the discovery that γ decreases with increasing humidity reported in Table 3.3.

Analysis of the acidic aerosol suspensions provided information on how composition, phase, and acidity affected coagulation. Adding sulfuric acid increased the acidity of the seed solution and the aerosols generated. Rindelaub et al. reported that the seed solution pH is much higher than that of the generated aerosol, e.g. a seed solution pH of 1.64 resulted in an aerosol pH of 0.37 determined via Raman microspectroscopy.[139] The three seed solutions were ~5.5 pH (ammonium sulfate only), ~2.5 pH, and ~1.5 pH. The two acidic solutions generated aerosols containing water, ammonium bisulfate, and sulfuric acid. Previous research reported that ammonium bisulfate and sulfuric acid do not effloresce, even at extremely low relative humidities (see Figure 3.14).[129,131] Therefore, in my work, the aerosols generated from the acidic solutions are expected to be aqueous droplets. I hypothesize that the acidic aerosols exhibit lower sticking coefficients (γ) than ammonium sulfate due to an increase in repulsive Coulomb forces from surface charges. Figure 3.17 shows the relationship between the coagulation coefficient scalar, γ, versus relative humidity (% RH) for the 5.5 pH, 2.5 pH, and 1.5 pH seed solutions.

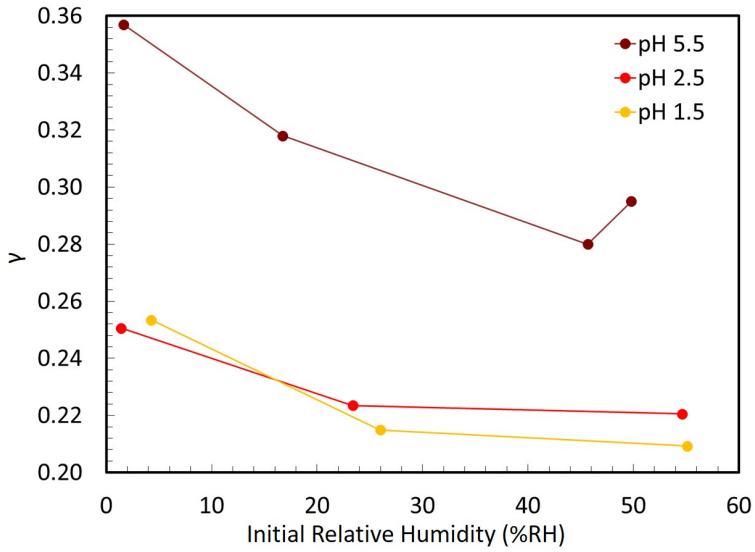

Figure 3.17: Graphical relationship between the coagulation coefficient scalar, γ, and relative humidity for the ammonium sulfate seed solution (dark red, 5.5 pH), and two ammonium sulfate/sulfuric acid seed solutions (red, 2.5 pH and yellow, 1.5 pH).

Acidic particles exhibited a decrease in γ as relative humidity increased, comparable to the ammonium sulfate particles. The aerosols in each trial are expected to be aqueous droplets. The coagulation scalar for acidic, aqueous droplets below 20% RH was similar to that of the ammonium sulfate aerosols in >45% RH. As described in Section 3.4.2, the only external factor that could decrease coagulation efficiency is surface charge.[16,138] Therefore, the low coagulation efficiency for the acidic aerosols resulted in aqueous droplets at all relative humidities and a likely increase in surface charge due to differences in particle composition.

3.6. Summary

Initial experiments involving particulate matter provided the first in depth insight into the aerosol dynamics in the rotating chamber. Monodisperse 1 μm polystyrene latex spheres represented the type of hard, spherical particle used in computational models.[114] The rotating ACSI suspended >70% of the PSLs over 16 hours while the particles deposited quickly (<8 hours) in a stationary chamber. Rotating the chamber at 2 RPM also established a uniform radial distribution of particles. Particle tracking models calculated by our collaborator,

Matt Brown, support both the suspension efficiency and uniform distribution of fine particulate matter. The uniform distribution indicates the particles will scatter the spectroscopic light in the optical path along the central axis. For the particle sizes and wavelengths of light currently used in the ACSI, $<2.4\times10^{-4}\%$ of the light in the optical path is elastically scattered by the particles, according to Rayleigh scattering.

The experiments described in this chapter are the first, to my knowledge, to explore the suspension efficiency of fine and ultrafine salt particles in a rotating chamber with a stationary, central optical path. Computational models predicted ultrafine monodisperse salts, i.e. less than 0.1 μm in diameter, have high suspension efficiencies in stationary and slowly rotating chambers (Figure 2.2). The monodisperse ammonium sulfate salt nanoparticles remained suspended in both the stationary and rotating chamber, as expected for low concentrations of 90±4 nm sized particles. Low monodisperse particle concentrations resulted in low collisional frequencies and thus no coagulation was observed on the 8 hour experimental timescale. No observable amount of monodisperse particles were lost to factors other than coagulation, such as gravitational deposition.

The aerosol dynamics model derived in Section 1.2.1.1 predicted polydisperse particles with a count median diameter of approximately 0.1 μm at low concentrations (<1000 particles/cm^3) will not coagulate. Low concentrations of solid, polydisperse, ammonium sulfate particles suspended in the ACSI had no observable particle coagulation, as expected by the computational model. Coagulation did occur when the initial ammonium sulfate concentrations were higher than $\sim1 \times 10^6$ particles/cm^3. Analysis of the number suspension efficiency (N/N_o) for different sized particles in both the 0 RPM and 2 RPM trials (Figure 3.9) confirmed coagulation in the particle suspensions when $N_o = \sim1 \times 10^6$ particles/cm^3.

Investigation of the number suspension efficiency (N/N_o) for different sized particles in the stationary chamber showed the effect of gravitational deposition on a suspension as particles coagulate. The larger particles formed by coagulation in the stationary trial deposited out of the suspension. In contrast, slow rotation (2 RPM) of the main chamber kept

the newly-formed aggregates suspended over 8 hours. The analysis of the number suspension efficiency (N/N_o) for different sized particles was used for the first time in this chapter to illustrate coagulation in various model atmospheres.

In Section 1.2.1.1, I defined the "sticking coefficient" (γ) that was used to quantify the changes in coagulation caused by different model atmospheres, such as relative humidity and particle composition. The experimental coagulation coefficient ($\gamma\beta\overline{K}$) was calculated using Equation 1.13 for the trials that exhibited coagulation. The experimental coagulation coefficients for all polydisperse ammonium sulfate suspensions were lower than the calculated $\beta\overline{K}$ based on the initial distribution characteristics. Common factors that affect coagulation include turbulence, formation of fractal aggregates, irregular shapes, and surface charge.[16,25,138,143] Surface charge is the only external factor known to slow coagulation in a particle suspension. Therefore, the ammonium sulfate particles are hypothesized to possess like surface charges that decrease coagulation efficiency and stabilize the particle suspension through repulsive forces.[138]

After establishing an analysis technique to quantify changes in coagulation, I explored the effect of particle phase state and composition on the coagulation of ammonium sulfate salt aerosols. Ammonium sulfate aerosols are generated as aqueous droplets and effloresced into solid aerosols in the model atmosphere when the relative humidity dropped below 35% RH. Ammonium sulfate aerosols are expected to be aqueous droplets at any relative humidity higher than 35% RH. Therefore, analyzing the aerosol dynamics at low (<35% RH) and high (>35% RH) humidities elucidated the effect phase state has on coagulation for ammonium sulfate aerosols. As humidity increased beyond the ammonium sulfate efflorescence (35% RH), the coagulation sticking coefficient (γ) decreased. Prior work reported simulated sea salt droplets had an enhanced cation concentration on the particle surface.[142] Therefore, I hypothesize the decrease in the sticking coefficient is related to the mobility of ions in an aqueous droplet versus a solid salt particle.

Coagulation efficiency also depends on particle composition, not just phase state. Acidic

aerosols were generated by adding sulfuric acid to the seed solution, which resulted in seed solutions with 5.5 pH, 2.5 pH and 1.5 pH. Acidic ammonium sulfate droplets contained ammonium bisulfate and sulfuric acid. Unlike ammonium sulfate, ammonium bisulfate and sulfuric acid do not effloresce after aerosol generation, which resulted in only aqueous droplets.[129,131,139] As expected, the coagulation sticking coefficient calculated for acidic ammonium bisulfate aerosols at relative humidities ranging from <10% RH to >55% RH are all lower than the ammonium sulfate aerosols (Figure 3.17). I expect the increased concentration of ions in the acidic droplets likely contribute to lower experimental coagulation coefficients.

Like-charges on the surface of particles, aqueous or solid, slow coagulation.[138,143] Pandis and Seinfeld derived a correction factor (W_c) that represents the effect of surface coulomb forces on the coagulation of two equal sized particles.[143] Equation 3.1 shows the insertion of the correction factor into the equation for coagulation flux. The correction factor is derived from the potential energy of the interaction between two charged particles. See Appendix A.1.3 for the derivation of W_c. The Coulomb force correction factor ($1/W_c$) is greater than 1 for particles with unlike charges and less than 1 for like-charged particles. I hypothesized that the coagulation of ammonium sulfate and ammonium bisulfate aerosols is lower than expected due to like charges on the particle surfaces. I quantified the decrease in coagulation by defining a "sticking coefficient" (γ), which always resulted in a value less than one. The sticking coefficients calculated in this section could be interpreted instead as the Coulomb force correction factor ($1/W_c$). Calculating $1/W_c$ for a polydisperse suspension is not trivial, however the correction factor is still a useful tool to provide insight into the effect of particle composition and phase state on coagulation.

$$J_{1,2} = \frac{1}{W_c} K_{1,2} N_1 N_2 \tag{3.1}$$

Overall, monodisperse and polydisperse particles remain uniformly suspended in the rotating chamber of the ACSI with a stationary optical path along the central axis. Coagulation

occurred when initial particle concentrations are approximately 1×10^5–1×10^6 particles/cm^3. Humidity, particle composition and phase state all affect coagulation through enhanced concentrations of like charges on the particle surface. Chapter 4 explores heterogeneous reactions on particle suspensions analogous to those characterized in this chapter.

Chapter 4

Ammonium Sulfate Heterogeneous Reactions

4.1. Introduction

The atmosphere consists of a highly complex mixture of gases ranging from small, inert diatomic molecules like nitrogen to reactive volatile organic compounds (VOCs).[26] Some reactive molecules, like alkyl amines and ammonia, are emitted directly into the atmosphere, while oxidation produces secondary reactive functional groups, including aldehydes or hydroxyl groups. Sulfur-containing pollutants, such as SO_2 from anthropogenic and natural combustion processes, are oxidized to form sulfuric acid. The process of sulfuric acid and other molecules interacting with particles in the surrounding atmosphere is one type of aerosol aging. Fine particulate matter ($PM_{2.5}$) has the longest atmospheric lifetime, thus particles <2.5 μm age more than larger, short-lived coarse mode particles. VOCs collect on particles and alter the overall reactivity of a surface. For example, Kelly et al. demonstrated that as metal oxide dusts reacted with nitric and sulfuric acid, the particle solubility in water increased. Semi-volatile compounds also condense onto particle surfaces without reacting with the bulk material, which increases the particle size. Aging processes affect the overall atmospheric fate of particles by either changing the particle reactivity or increasing the particle size until the particle settles or washes out of the atmosphere.

Heterogeneous reactions involved in aerosol aging are complex processes that potentially produce new molecules or release gases back into the atmosphere. For example, isopropanol dissolved into water on Gobi Desert dust produces and releases acetone and formaldehyde upon photolysis with UV light.[98] Aqueous ammonium and carbonate ions catalyze aldol reactions with glyoxal molecules.[74] Another inorganic salt, ammonium sulfate, is formed in the atmosphere through the reaction between sulfuric acid and ammonia. Ammonium sulfate releases trace amounts of ammonia upon acid-base reaction with alkyl amines that are more

basic and less volatile than ammonia.[1,99,100,107] In this chapter, research in which the ACSI was employed to investigate the types of heterogeneous reactions described above, especially those that produce gas-phase molecules is described.

Chapter 4 focuses on acid-base reactions that involve alkyl amines and ammonium sulfate aerosols. Short chain alkyl amines and ammonia are abundant gases emitted from both anthropogenic and natural sources.[86] Amines remain in the atmosphere for days in the gas-phase,[87] ambient particulate matter,[85,86] and fog and cloud water.[13,86,88] As sulfuric acid reacts with ammonia to form secondary ammonium sulfate aerosols, the particles are not completely chemically neutralized. The resulting particles are more acidic than a particle with a 2:1 ammonium to sulfate ratio.[86] Most laboratory studies that investigate atmospheric amine chemistry involve non-atmospheric conditions, such as single particle levitation[120] or ammonium sulfate coated flow tube reactor.[99,100] For example, Qiu et al. used a flow tube reactor and chemical ionization mass spectrometer to discover that the monomethyl amine reaction with acidic ammonium sulfate, or ammonium bisulfate, did not release a detectable amount of ammonia, which suggests the alkyl amine only reactively uptakes onto the particle. The ACSI was designed to monitor heterogeneous reactions in a controlled aerosol suspension that better represents the conditions naturally occurring in the atmosphere. Specifically, the spectroscopy integrated into the ACSI was used to detect gas-phase products *in situ* from heterogeneous reactions that occur at the vapor-particle interface, such as the ammonia released off of ammonium sulfate particles.

Cavity ring-down spectroscopy incorporated into the ACSI allowed for the detection of trace gas concentrations nearing the parts per billion (ppb) level *in situ*. Common analytical techniques sensitive enough to detect ppb-level gases usually involve *ex situ* and destructive analysis, such as mass spectrometry or gas chromatography. The *in situ* spectroscopic technique affords the opportunity to monitor changes in the model atmosphere without disturbing the particulate matter. Stable model atmospheres are created in the ACSI via the rotating main chamber, see Chapter 3 for more information on the suspension efficiencies

of ammonium sulfate particles. The following sections explore the effect of the model atmosphere and the particle composition on heterogeneous reactions between monomethyl amine and ammonium sulfate.

4.2. Ammonia Release from Heterogeneous Reaction Between Ammonium Sulfate and Monomethyl Amine

A prevalent atmospheric reaction involves the chemical neutralization of acids, such as sulfuric acid, by basic gases like ammonia or alkyl amines to form secondary particulate matter.[17,86,99,100] Ammonia gas is the most abundant atmospheric base and readily neutralizes sulfuric acid to produce ammonium sulfate. Nitric acid participates in analogous acid-base reactions, however amines preferentially neutralize sulfuric acid over nitric acid.[86] Other amines, such as dimethyl amine, also react with atmospheric acids to form aminium salts.[1] Amine chemistry in the atmosphere has been monitored directly and simulated with laboratory studies involving flow tubes or single particle levitation.[86,99,100,120] The following experiments conducted with the ACSI bridge the gap between the monitoring and collection of particulate matter and laboratory studies with a well-controlled model atmosphere simulating the conditions necessary for amine-related heterogeneous reactions.

Alkyl amines compete with ammonia to form secondary organic aerosols and react with existing salt particles. For instance, Youn et al. observed a peak mass concentration of dimethyl aminium ions that directly correlated with the ammonium and sulfate concentrations in $PM_{2.5}$ collected in the Southwest United States.[86] Table 4.1 lists the pK_b for select atmospheric amines in 25°C water. Aqueous basicity constants provide further insight into the acid-base reactions that occur in a humid atmosphere. The two strongest atmospheric bases, monomethyl amine and dimethyl amine, are known to preferentially form alkyl aminium sulfate particles in new particle formation events with sulfuric acid, even in the presence of ammonia.[1,106,107] Basic alkyl amines also displace ammonium ions in ammonium sulfate aerosols, which causes ammonia to partition back into the gas phase.[1,99,100]

Table 4.1: Base dissociation constants of select alkyl amines in 25°C water.[144]

Compound	Structure	pK_b
Ammonia	NH_3	4.7
Monomethyl amine	CH_3NH_2	3.4
Dimethyl amine	$(CH_3)_2NH$	3.3
Trimethyl amine	$(CH_3)_3N$	4.3

Previous laboratory studies have shown that ammonium sulfate produces gaseous ammonia upon the reactive uptake of alkyl amines in the presence of ≥5% relative humidity.[99,100] The net reaction between monomethyl amine and ammonium sulfate is depicted in Reaction R 4.1.

$$n CH_3NH_{2(g)} + (NH_4)_2SO_{4(aerosol)} \longrightarrow n NH_{3(g)} + (CH_3NH_3)_n(NH_4)_{2-n}SO_{4(aerosol)} \quad (R\,4.1)$$

The ammonia displacement reaction in a humid model atmosphere was selected as a proof-of-concept study since sulfate particles play a critical role in atmospheric aging chemistry. Benchmark tests involved *in situ* monitoring with cavity ring-down spectroscopy as the ammonium sulfate aerosol suspension is exposed to monomethyl amine. The perturbation of a stable model atmosphere with an analyte gas simulates the scenario in which a reactive pollutant alters and ages an existing particle suspension.

4.2.1. Experimental Details

4.2.1.1. Materials

Certified ACS grade ammonium sulfate salt was purchased from Fisher Chemical. The control particles were 1% monodisperse 0.994 ± 0.012 μm spherical polystyrene latex particles (PSLs) suspended in water with a proprietary surfactant to minimize coagulation in solution were purchased from Thermo Fisher Scientific (Duke Standards 4009A). A lecture bottle of ≥99.9% anhydrous ammonia was purchased from Sigma Aldrich. A lecture bottle

of monomethyl amine was purchased from Matheson Tri-Gas. Research grade UHP N_2 was purchased from Praxair, Inc. Deionized water was acquired from Hahn Hall South (Millipore Purification Systems, 18.2 MΩ). HPLC grade, submicron filtered water used for humidity control was purchased from Fisher Chemical.

4.2.1.2. Analyte Introduction

The experiment began with the background procedure described in Section 2.5. Water vapor was added until the relative humidity reached the desired level using the procedure from Section 2.5.1.1. The rotating main chamber was evacuated to approximately 600 Torr. Twenty psi of UHP N_2 flowed through a Collison 6-jet nebulizer containing approximately 40 mL of 0.6833 g/L aqueous ammonium sulfate solution (pH ~5.5). The newly generated salt aerosols flowed through a TSI 3062 diffusion dryer to remove excess water before introduction into the main chamber. Aerosol introduction continued until the chamber returned to atmospheric pressure.

The aerosol suspension reached a stable distribution after 1–2 hours in the chamber. The chamber was evacuated until the pressure was 10 Torr below atmospheric pressure in preparation for monomethyl amine introduction. Twenty seconds of 100 SCCM monomethyl amine gas was introduced into the chamber using a metal sealed mass flow controller (MKS GM50A013503SBV020). UHP N_2 was added until the chamber returned to atmospheric pressure.

4.2.1.3. Sampling Procedure

The nanoparticle suspensions were sampled through all four sampling ports simultaneously in triplicate every 20–60 minutes using an electrostatic classifier (TSI 3080), long DMA (TSI 3081) and water condensation particle counter (TSI 3782) in scanning mobility particle sizer (SMPS) mode. The sample flowed into the SMPS at approximately 0.60 SLPM aerosol flow rate.Multiple charge and diffusion correction TSI algorithms were applied to each SMPS data set. The algorithms are described in detail by TSI Incorporated.[136] A port on the oppo-

site side of the chamber to the aerosol sampling instrument was opened to filtered laboratory air to maintain atmospheric pressure within the chamber during active sampling. A CRDS spectrum was collected during each particle sampling event.

4.2.2. Results and Discussion

The ACSI employs multi-pass, non-destructive, infrared spectroscopy to detect ppb-levels of gases evolved from controlled heterogeneous reactions. The model atmosphere developed to explore the reactive uptake of monomethyl amine onto ammonium sulfate particles involved multiple infrared-absorbing gases, such as water vapor, monomethyl amine, and trace amounts of ammonia. Several control spectra and spectra recorded at strategic points during each experiment validated the displacement of ammonia using Beer's Law (Equation 2.9). To the best of my knowledge, the following results are the first time the reactive uptake of monomethyl amine has been observed *in situ* on an aerosol suspension using infrared cavity ring-down spectroscopy.

$$A(\nu) = \sigma_1(\nu)N_1 d + \sigma_2(\nu)N_2 d + \ldots \sum_{i=1}^{n} \sigma_i(\nu)N_i d \qquad \text{(2.9 revisited)}$$

Spectra were recorded at critical points in the experiment: before and after water vapor (humidity) introduction, after the ammonium sulfate aerosol introduction, and finally after the perturbing the model atmosphere with monomethyl amine. The background spectrum recorded (Figure 4.1) shows the mid-infrared absorption features of the model atmosphere containing only ammonium sulfate aerosols, 60% RH, and UHP N_2. The spectrum of the initial model atmosphere shows absorption features that were subtracted from subsequent spectra recorded after monomethyl amine introduction.

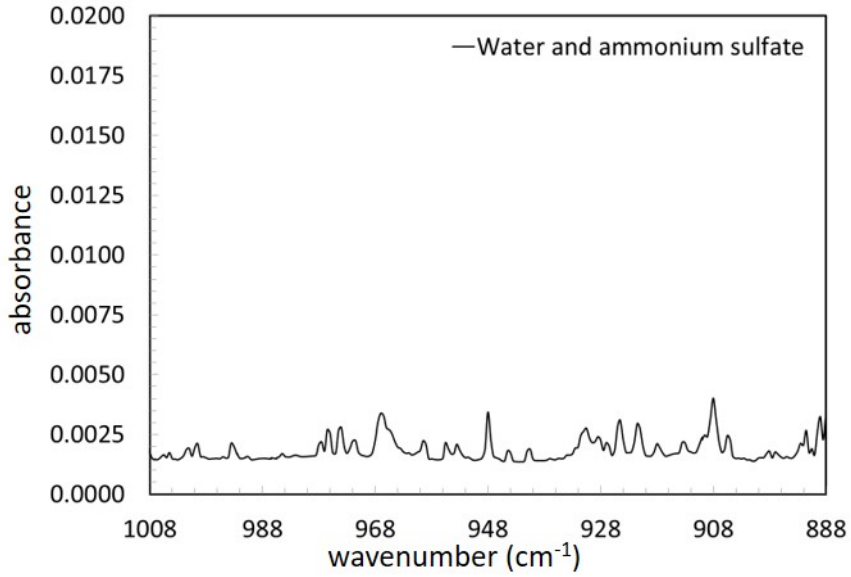

Figure 4.1: Absorption spectrum of the model atmosphere containing only ammonium sulfate aerosols, 60% RH, and UHP N_2.

The CRDS mid-infrared spectrum recorded after monomethyl amine introduction into the model atmosphere is shown as the green spectrum in Figure 4.2. The spectrum includes the additive absorption of each absorbing species in the model atmosphere. The black background spectrum is subtracted from the green spectrum, which results in the spectrum of the excess monomethyl amine and gases produced via Reaction R 4.1.

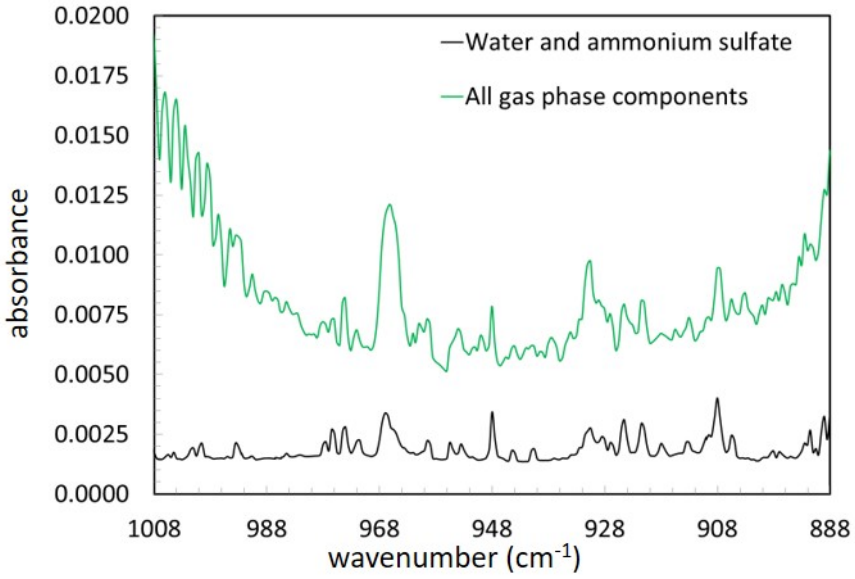

Figure 4.2: Absorption spectra of the initial model atmosphere (black) and mixture of the model atmosphere and the monomethyl amine (green).

The subtraction of the initial model atmosphere spectrum from the total additive absorption spectrum post monomethyl amine introduction produced the blue spectrum in Figure 4.3, representative of the absorption only from the excess monomethyl amine and gas-phase products from Reaction R 4.1. A scaled control spectrum of monomethyl amine in dry UHP N_2, red spectrum in Figure 4.3, is subtracted from the blue spectrum representative of the monomethyl amine and gas products in order to produce the spectrum in Figure 4.4, indicative of only the gas-phase products from Reaction R 4.1.

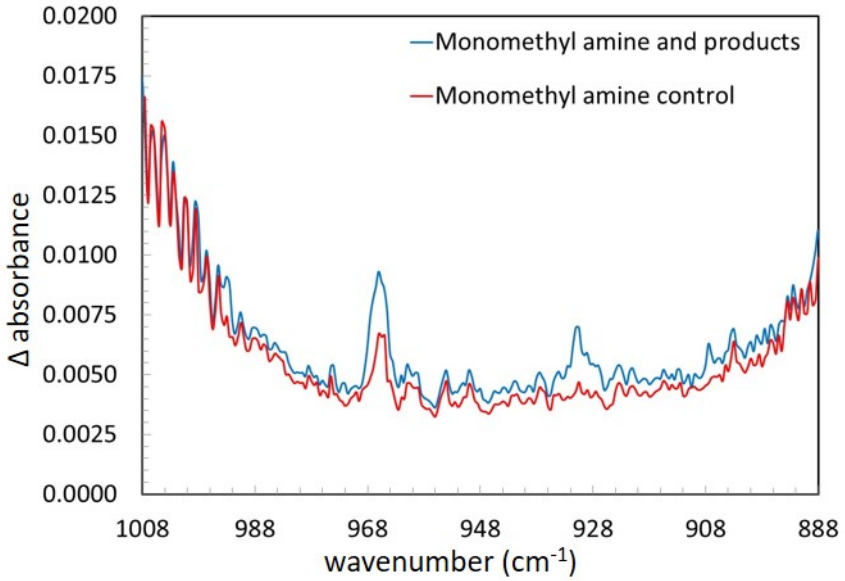

Figure 4.3: Absorption spectra of excess monomethyl amine and gas products (blue) and a scaled monomethyl amine in dry UHP N_2 control spectrum (red).

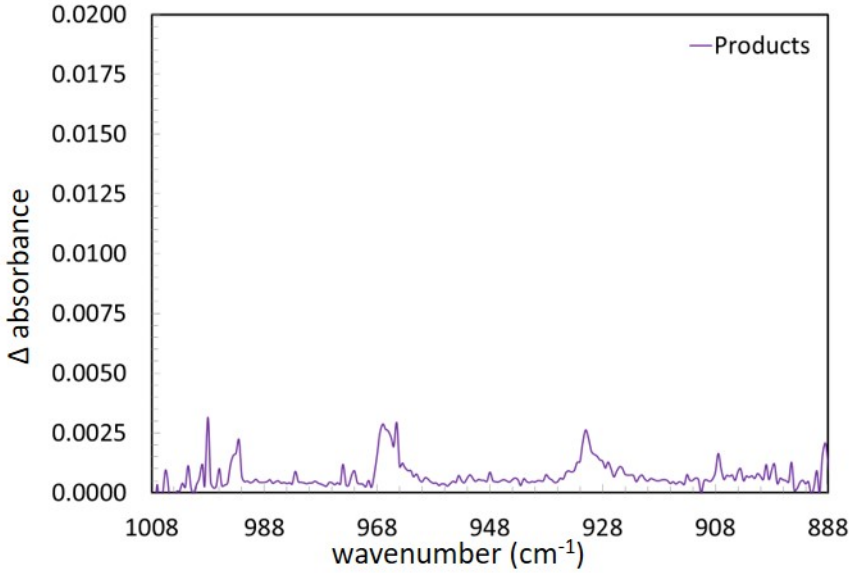

Figure 4.4: Absorption spectrum of the gas-phase products released from the heterogeneous reaction between monomethyl amine and a model atmosphere containing ammonium sulfate, 60% RH, and UHP N_2.

The spectral features in Figure 4.4 suggest the presence of a gas product after the heterogeneous reaction. I hypothesize that the gas produced is ammonia partitioned off of the ammonium sulfate particles after reaction with monomethyl amine. In order to validate the

evolved gas was ammonia, the spectrum was compared with a control spectrum and the calculated High Resolution Transmission (HITRAN) spectral line positions and intensities for ammonia.[124,125] Figure 4.5 shows the comparison between the gas product spectrum, scaled ammonia control spectrum and the HITRAN calculated spectral features for ammonia.

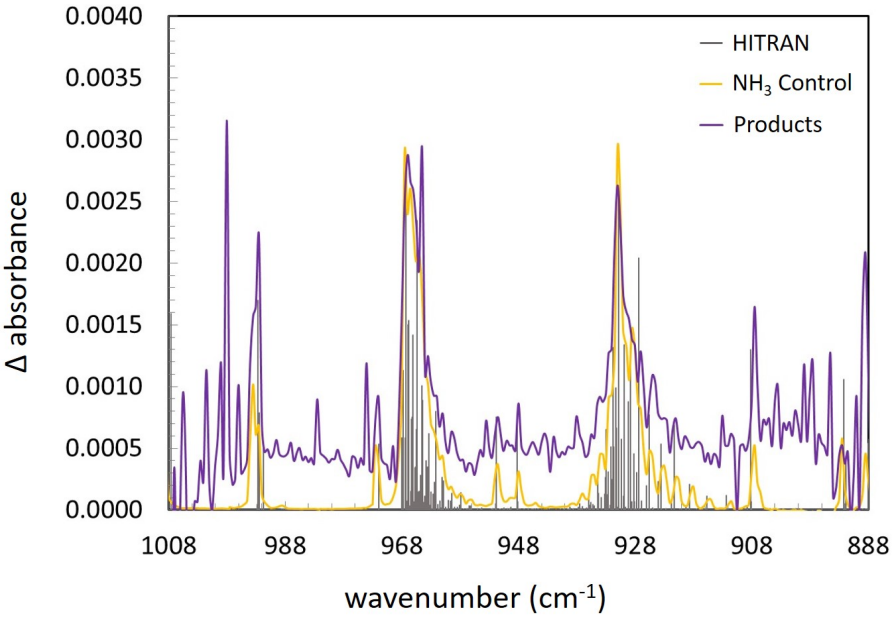

Figure 4.5: Comparison of the products spectrum (purple), ammonia control (yellow) and scaled HITRAN calculated spectral line positions and intensities for ammonia (grey).[124,125]

The spectrum of the evolved reaction products is consistent with the recorded and calculated spectral features of ammonia (Figure 4.5). The CRDS incorporated into the ACSI required 6 minutes to record one spectrum. I expect the amount of ammonia gas detected from the ammonium sulfate/monomethyl amine reaction to remain steady after the first acquisition and throughout the remainder of the experiment, which could last 2+ hours. Figure 4.6 shows CRDS spectra recorded after 0 minutes, 67 minutes, and 120 minutes post monomethyl amine introduction.

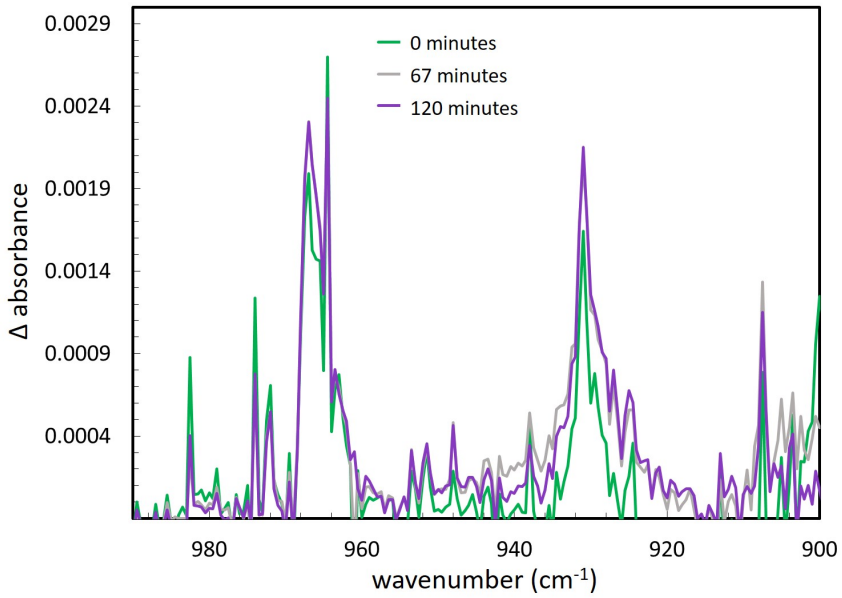

Figure 4.6: Ammonia produced by the reaction between monomethyl amine and ammonium sulfate in 60% RH over time. The green spectrum was recorded immediately after the monomethyl amine introduction process, the grey and purple spectra were recorded at 67 minutes and 120 minutes post exposure.

Ammonia was detected immediately after perturbing the humid ammonium sulfate suspension with monomethyl amine. Figure 4.6 shows that the ammonia spectral features remained constant after 67 minutes and 120 minutes. Stable concentrations of ammonia were also observed for all remaining experiments in this chapter.

Although I hypothesize that ammonia was released directly from the heterogeneous reaction involving ammonium sulfate suspended particles, other possibilities, including chamber-wall reactions, could explain the generation of gas-phase ammonia. The hypothesis was tested with a control experiment to verify the ammonia release required the reactive, ammonium sulfate aerosols. Nonreactive, polystyrene latex particles (PSLs) under similarly humid conditions (~30% RH) replaced the ammonium sulfate aerosols in the control experiment. The experiment began by establishing the model atmosphere, which contained the desired relative humidity and an analyte particle suspension. After the model atmosphere of PSLs and humidity stabilized, monomethyl amine was introduced and Figure 4.7 shows the corresponding

spectra recorded during the control experiment.

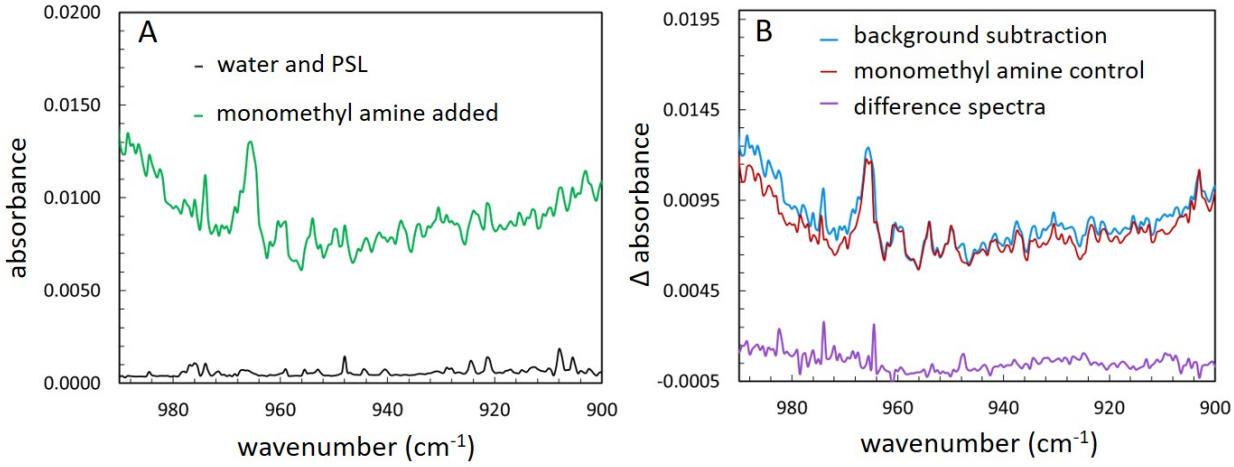

Figure 4.7: Spectra representing the lack of ammonia gas evolution after exposing 0.994 ± 0.012 μm particles to monomethyl amine. A) Black spectrum illustrates the CRDS spectrum of PSLs in approximately 30% RH. Green spectrum was recorded upon release of monomethyl amine into the simulated cloud, thus the spectrum contains features associated with the particles, water vapor, and excess monomethyl amine. B) The black, background spectrum was subtracted from the green spectrum resulting in the blue spectrum, which indicates excess monomethyl amine. The scaled monomethyl amine control spectrum (red) is subtracted from the blue spectrum. Purple spectrum is the difference between the blue and red spectrum.

The final spectrum in Figure 4.7B suggests the monomethyl amine did not produce gas-phase products upon release into the PSL atmosphere. More specifically, no ammonia was released from the control particles or the chamber wall upon monomethyl amine introduction. The lack of ammonia production in the control experiment also indicated minimal ammonium sulfate contamination from particles deposited on the chamber walls or residual aerosol suspensions from previous experiments. Therefore, the heterogeneous Reaction R 4.1 only produced ammonia in the presence of an ammonium sulfate particle suspension and monomethyl amine.

4.3. Effect of Humidity on Ammonia Release from the Reaction between Ammonium Sulfate and Monomethyl Amine

Atmospheric relative humidity dramatically ranges from region to region, which can have a major influence on the dynamics and interfacial chemistry of aerosols. The lowest relative humidities range from ~25% RH in the Saharan Desert to ~70% RH in tropical areas and 100% RH in clouds.[19,20,123] Long-lived $PM_{2.5}$ in the atmosphere might travel from areas of high humidity to low or vice versa. Areas of different relative humidity and pollutant concentrations age and alter fine particulate matter composition. Particle composition and relative humidity dictates if an aerosol exists as a solid or liquid. The transition from a solid to a liquid aerosol is deliquesence and the liquid to solid transition is efflorescence.[131] The particle phase state affects the efficiency of most atmospheric heterogeneous reactions.[100] The ACSI was designed to introduce water vapor into any model atmosphere to mimic natural variations.

The proof-of-concept heterogeneous reaction between monomethyl amine and ammonium sulfate is known to approach 100% completion with ≥10% RH present. Chan and Chan reported that at low relative humidity (<5% RH), monomethyl amine displaced less than 7.1 ± 9.4% of the ammonia in ammonium sulfate particles.[120] However, at high relative humidity, over 50% RH, >95% of the ammonia was displaced by the monomethyl amine. The following section utilizes the humidity control and cavity ring-down spectroscopy capability of the ACSI to explore the effect of relative humidity on the amount of ammonia displaced from Reaction R 4.1.

4.3.1. Experimental Details

4.3.1.1. Materials

Certified ACS grade ammonium sulfate salt was purchased from Fisher Chemical. A lecture bottle of monomethyl amine was purchased from Matheson Tri-Gas. Research grade UHP N_2 was purchased from Praxair, Inc. The deionized water was acquired from the Hahn

Hall South facilities (Millipore Purification Systems, 18.2 MΩ). HPLC grade, submicron filtered water used for humidity control was purchased from Fisher Chemical.

4.3.1.2. Analyte introduction

The experiment began with the background procedure described in Section 2.5. Water vapor was added until the relative humidity reached the desired level using the procedure in Section 2.5.1.1. The rotating main chamber was evacuated to approximately 600 Torr. Twenty psi of UHP N_2 flowed through a Collison 6-jet nebulizer containing approximately 40 mL of 0.6833 g/L aqueous ammonium sulfate solution. The newly generated salt aerosols flowed through a TSI 3062 diffusion dryer to remove excess water before introduction into the main chamber. Aerosol introduction continued until the chamber returned to atmospheric pressure.

The aerosol suspension reached a stable distribution after 1–2 hours in the chamber. The chamber was evacuated until the pressure was 10 Torr below atmospheric pressure in preparation for monomethyl amine introduction. Twenty seconds of 100 SCCM monomethyl amine gas was introduced into the chamber using a metal sealed mass flow controller. UHP N_2 was added until the chamber returned to atmospheric pressure.

4.3.1.3. Sampling Procedure

The nanoparticle suspensions were sampled through all four sampling ports simultaneously in triplicate every 20–60 minutes using an electrostatic classifier (TSI 3080), long DMA (TSI 3081) and water condensation particle counter (TSI 3782) in scanning mobility particle sizer (SMPS) mode. The sample flowed into the SMPS at approximately 0.60 SLPM aerosol flow rate. Multiple charge and diffusion correction TSI algorithms were applied to each SMPS data set. The algorithms are described in detail by TSI Incorporated.[136] A port on the opposite side of the chamber to the aerosol sampling instrument was opened to filtered laboratory air to maintain atmospheric pressure within the chamber during active sampling. A CRDS spectrum was collected during each particle sampling event.

4.3.2. Results and Discussion

Three model atmosphere relative humidities were created prior to ammonium sulfate introduction: no additional water vapor (<5-15% RH), ~30% RH and ≥60% RH. The introduction of aerosol particles, which are never completely desiccated, typically increases the relative humidity approximately 5–20% RH. The aerosols generated were aqueous ammonium sulfate salt droplets, which were then dried and introduced into the main chamber. Two of the experiments had a relative humidity lower than efflorescence humidity of ammonium sulfate (35% RH) after aerosol introduction. Monomethyl amine was added approximately 1–2 hours after aerosol introduction. Figure 4.8 shows the gas-phase product spectra for each trial was determined with the same spectral subtraction analysis process described in Section 4.2.2.

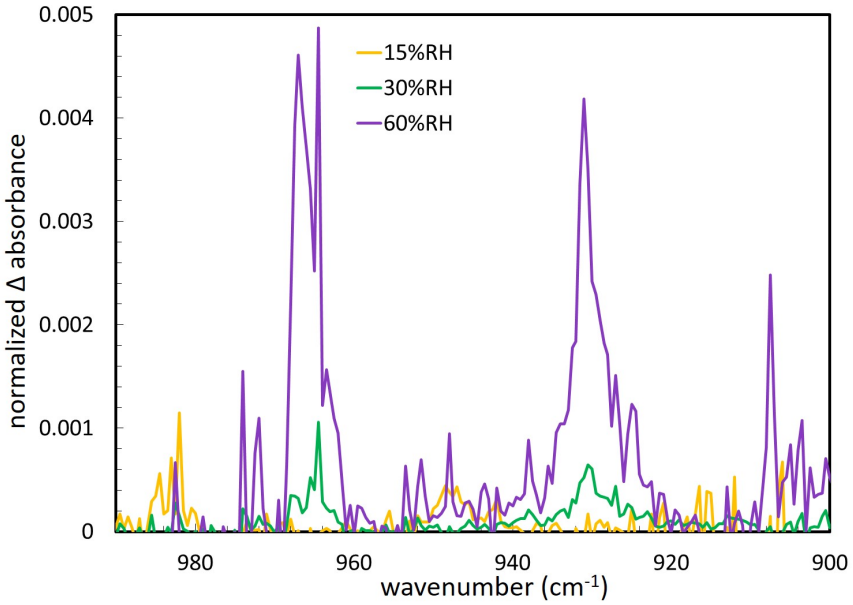

Figure 4.8: Ammonia gas produced from the reaction between monomethyl amine and ammonium sulfate at 60% RH (purple), 30% RH (green) and 15% RH (yellow). All spectra are normalized to the ammonium sulfate particle mass concentration for each trial.

Prior work reported a decrease in ammonia displacement upon reaction between alkyl amines and ammonium sulfate in flow tube reactors and single particle levitation when

the relative humidity was <5–15% RH.[100,120] The three trials conducted with the ACSI were performed at <15% RH, 30% RH, and 60% RH. Each spectrum in Figure 4.8 was normalized to the ammonium sulfate mass concentration in each trial. Ammonium sulfate is the limiting reagent for Reaction R 4.1 and the amount of ammonia available for displacement is proportional to the aerosol concentration. The 60% RH trial exhibited the highest amount of ammonia displaced due to the ammonium sulfate/monomethyl amine reaction. The 30% RH trial showed much less ammonia displacement when compared to the 60% RH trial. No gas-phase ammonia is detected after monomethyl amine introduction into the model atmosphere when the relative humidity was below 15% RH.

I hypothesize that the aerosol phase state affects the reaction efficiency at each relative humidity. Previous studies which used single particle levitation[100,120] and a flow reactor[99] reported Reaction R 4.1 occurred only with excess water present. Chan and Chan also reported that monomethyl amine displaced less than 7% of the ammonium ions in crystalline ammonium sulfate while monomethyl amine displaced over 95% of the ammonium ions in aqueous ammonium sulfate.[120] The particles used in the ASCI experiments are assumed to effloresce into solid particles in the two low humidity trials and exist as an aqueous droplet in the 60% RH trial. As expected, the monomethyl amine displaced less ammonia from crystalline ammonium sulfate (0–15% RH and 30% RH) when compared to the reaction with aqueous aerosols (60% RH). The experiments described in this section demonstrate the capabilities of the ACSI to explore the effect of various model atmosphere compositions on a heterogeneous reaction.

4.4. Effect of Particle Composition on Heterogeneous Acid-Base Reactions

Anthropogenic and natural sources introduce 81 Tg of sulfur and >21 Tg of nitrogen every year.[13,29,30,33] Oxidants, such as ozone and hydroxyl radicals, readily oxidize molecules containing sulfur and nitrogen atoms. Oxidation and other atmospheric reactions produce sulfuric acid (H_2SO_4) and nitric acid (HNO_3). Sulfuric and nitric acid are the two most

abundant, strong acids in the atmosphere.

Atmospheric acids react with almost every type of particle and molecule. For example, nitric acid commonly reacts with mineral oxide dust particles, which increases the hygroscopicity of the dust.[72] Acids incorporated into cloud water droplets contribute to acid rain.[145] Gas-phase acid-base reactions also form secondary inorganic salt aerosols, most commonly ammonium sulfate ($(NH_4)_2SO_4$).[1] Sulfuric acid is not always chemically neutralized by atmospheric bases. Youn et al. reported the NH_4^+:SO_4^{2-} ratio was less than 2:1 in $PM_{1.0}$ from the Southwest United States, which indicated the presence of ammonium bisulfate (NH_4HSO_4).[86] Ammonium bisulfate and other acidic particles (pH < 1)[139,140] catalyze heterogeneous reactions that usually require strong acid or base catalysts, such as aldol condensations.[74]

Sections 4.2 and 4.3 focused on ammonia displacement due to the heterogeneous reaction between monomethyl amine and ammonium sulfate. Ammonium bisulfate also reacts with alkyl amines, however ammonia is not displaced by the reaction.[99] The bisulfate ion donates a hydrogen atom to the alkyl amine instead of an ammonium ion (Reaction R 4.2).

$$CH_3NH_{2(g)} + NH_4HSO_{4(aerosol)} \longrightarrow CH_3NH_3NH_4SO_{4(aerosol)} \qquad \text{(R 4.2)}$$

According to previous literature,[99] little to no ammonia is expected to partition off of the ammonium bisulfate particles upon reaction with monomethyl amine. The following section explores Reaction R 4.2 with monomethyl amine and ammonium bisulfate under humid conditions.

4.4.1. Experimental Details

4.4.1.1. Materials

Certified ACS grade ammonium sulfate salt was purchased from Fisher Chemical. Certified ACS grade sulfuric acid was purchased from Spectrum Chemical. A lecture bottle of monomethyl amine was purchased from Matheson Tri-Gas. Research grade UHP N_2 was

purchased from Praxair, Inc. The deionized water was acquired from the Hahn Hall South facilities (Millipore Purification Systems, 18.2 MΩ). HPLC grade, submicron filtered water used for humidity control was purchased from Fisher Chemical.

4.4.1.2. Analyte introduction

The experiment began with background measurements described in Section 2.5. Water vapor was added until the relative humidity reached the desired level using the procedure in Section 2.5.1.1. Sulfuric acid was added to the ammonium sulfate seed solution to generate the acidic particles. The seed solution acidity was increased until the pH reached ~2.5 for the first trial and ~1.5 pH for the second trial. The acidic seed solutions are assumed to contain a mixture of ammonium sulfate, ammonium bisulfate, and sulfuric acid. The rotating main chamber was evacuated to approximately 600 Torr. Twenty psi of UHP N_2 flowed through a Collison 6-jet nebulizer containing approximately 40 mL of 0.6833 g/L aqueous ammonium sulfate/sulfuric acid solution. The newly generated salt aerosols flowed through a TSI 3062 diffusion dryer to remove excess water before introduction into the main chamber. Aerosol introduction continued until the chamber returned to atmospheric pressure.

The aerosol suspension reached a stable distribution after 1–2 hours in the chamber. The chamber was evacuated until the pressure was 10 Torr below atmospheric pressure in preparation for monomethyl amine introduction. Twenty seconds of 100 SCCM monomethyl amine gas was introduced into the chamber using a metal sealed mass flow controller. UHP N_2 was added until the chamber returned to atmospheric pressure.

4.4.1.3. Sampling Procedure

The nanoparticle suspensions were sampled through all four sampling ports simultaneously in triplicate every 20–60 minutes using an electrostatic classifier (TSI 3080), long DMA (TSI 3081) and water condensation particle counter (TSI 3782) in scanning mobility particle sizer (SMPS) mode. The sample flowed into the SMPS at approximately 0.60 SLPM aerosol flow rate. Multiple charge and diffusion correction TSI algorithms were applied to

each SMPS data set. The algorithms are described in detail by TSI Incorporated.[136] A port on the opposite side of the chamber to the aerosol sampling instrument was opened to filtered laboratory air (Parker Balston 9922-05-CQ) to maintain atmospheric pressure within the chamber during active sampling. A CRDS spectrum was collected during each particle sampling event.

4.4.2. Results and Discussion

Acidic ammonium sulfate aerosols were generated by adding 2–5 drops of concentrated sulfuric acid to the seed solution. The resulting aerosols consist of a mixture of ammonium, sulfate, bisulfate, and hydronium ions. Seed solution pH ranged from ~5.5 to ~1.5, which produces aerosols with much lower pH.[139] For example, a seed solution pH of 1.64 results in an aerosol with a pH of 0.37. Ammonium bisulfate and sulfuric acid are highly hygroscopic and do not effloresce to form crystalline aerosols, even at extremely low relative humidities.[129,131,139] The following experiments were conducted at 55–60% RH because ammonium sulfate aqueous droplets effloresce at 35% RH and Reaction R 4.1 is more efficient at humidities above 50% RH. The acidic aerosol droplet experiments provided information on the effect of particle composition on heterogeneous reactions. The acidic particles have available acidic protons that are from bisulfate, not only from ammonium ions. Therefore, I hypothesize the acidic aerosols will produce much less, if any, ammonia gas upon reaction with monomethyl amine. Figure 4.9 shows the gas product spectra for the ammonium sulfate and two acidic particle suspensions after exposure to monomethyl amine.

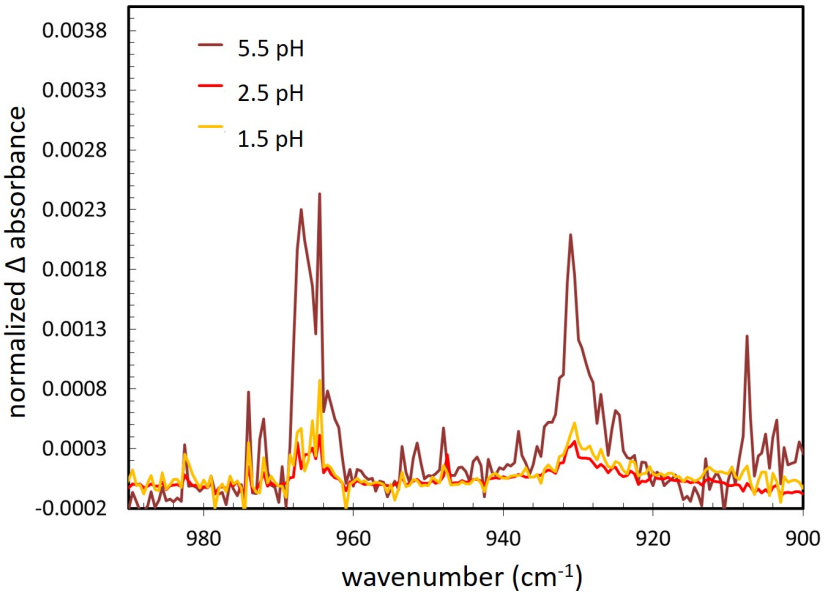

Figure 4.9: Ammonia gas produced from reaction of monomethyl amine with ammonium sulfate at varying levels of acidity in 55–60% RH. All spectra are normalized to the ammonium sulfate particle mass concentration for each trial.

To my knowledge, this is the first time any amount of ammonia has been detected from the reaction of monomethyl amine and a acidic ammonium sulfate aerosol suspension. Prior work by Qiu et al. reported no detectable amount of ammonia released from the monomethyl amine/ammonium bisulfate reaction (Reaction R 4.2) in a low pressure flow reactor and related the results to the same reaction between monomethyl amine and pure sulfuric acid.[99] However, the acidic aerosols suspended in the ACSI released much less ammonia than ammonium sulfate under 55–60% RH, though still a detectable amount. All gas product spectra shown in Figure 4.9 were normalized to the particle mass concentration for each trial because the amount of ammonia available for release into the gas phase is proportional to the mass concentration of the ammonium bisulfate acidic aerosol suspension. Aerosols in all three trials exist as aqueous salt droplets, therefore the decreased displacement of ammonia in acidic aerosols is due to the different aerosol compositions, not the particle phase state. Monomethyl amine mostly reacted with the bisulfate ions rather than exchanging a proton with ammonium ions. A small amount of ammonia is released after monomethyl amine introduction in

the acidic aerosol trials. Increasing the aerosol acidity by adding more sulfuric acid resulted in the same amount of ammonia displacement after monomethyl amine introduction, even though the aerosol bulk material contained excess bisulfate ions. The unexpected detection of ammonia displacement from acidic aerosols is most likely due to the proton donation from ammonium ions, which produces ammonia gas similar to Reaction R 4.1. Further research is needed to quantify the ammonia, monomethyl amine and other gas-phase species using the CRDS or other analysis techniques.

4.5. Summary

The experiments above utilized the ACSI to perform the first ever *in situ* monitoring of heterogeneous reactions in a rotating chamber. A stationary optical path for CRDS incorporated into the central axis of the chamber afforded the ability to detect trace amounts of ammonia gas displaced from ammonium sulfate upon reaction with monomethyl amine. Previous research reported Reaction R 4.3 only occurs when >5% RH was present using a flow tube reactor[99] and single particle levitation.[100] The ACSI explored the reaction in a model atmosphere with more than 60% RH, initially ensuring the excess monomethyl amine displaced ammonia.

$$n CH_3NH_{2(g)} + (NH_4)_2SO_{4(aerosol)} \longrightarrow n NH_{3(g)} + (CH_3NH_3)_n(NH_4)_{2-n}SO_{4(aerosol)} \quad \text{(R 4.3)}$$

As expected, the CRDS detected ammonia released into the 60% RH model atmosphere due to the ammonium sulfate-monomethyl amine reaction. Figures 4.1, 4.2, 4.3, and 4.4 display the spectra recorded during the evolution of ammonia. The reaction released the most ammonia when the model atmosphere had a relative humidity greater than 60%. Less ammonia was detected when the relative humidity decreased to 30% RH and no ammonia was detected when the particles suspended were in 15% RH. Contrary to previous experiments,[99,100] the reaction did not produce as much ammonia when the model atmosphere relative humidity decreased to 30% RH and ~15% RH. I hypothesize that the decrease in

ammonia production is related to the phase state of the ammonium sulfate particles prior to reaction with monomethyl amine. Ammonium sulfate effloresces at 35% RH,[129] therefore the particles are expected to be solid salt particles in the 30% RH and 15% RH model atmospheres. The monomethyl amine is able to displace the ammonia throughout the bulk material of aqueous aerosols at 60% RH and only react with the ammonium ions on the surface of the solid salt particles. The absence of ammonia gas in the 15% RH atmosphere suggests some water on the particle surface is necessary to facilitate the proton exchange between the ammonium ions and monomethyl amine gas.

Ammonium bisulfate is similar in composition to ammonium sulfate, only with an ammonium to sulfate ratio <2:1. Ammonium bisulfate represents the secondary ammonium sulfate particles in the atmosphere where the sulfuric acid is not chemically neutralized by ammonia or other amines.[86] I used the ACSI to explore how a model atmosphere with aerosols comprised of ammonium bisulfate and sulfuric acid interact with monomethyl amine. Qiu et al. did not detect any ammonia released from the reaction between monomethyl amine and ammonium bisulfate, instead the monomethyl amine only experienced acid-base reactive uptake onto the acidic particles.[99]

I performed a series of experiments with aerosols containing a mixture of ammonium bisulfate, sulfuric acid, and water analogous to those conducted by Qiu et al.[99] Ammonium bisulfate and sulfuric acid do no effloresce, even at extremely low relative humidity,[129,131,139] therefore the acidic aerosols are expected to be aqueous droplets, not solid salt particles. The CRDS monitored the introduction of monomethyl amine into a model atmosphere with acidic aerosols and >50% RH. A relative humidity of >50% was chosen in order to directly compare ammonia released from aqueous ammonium sulfate aerosols and acidic ammonium bisulfate/sulfuric acid aerosols without the effect of phase state on the reaction.

In contrast to the results previously reported,[99] the CRDS detected ammonia displacement from the acidic ammonium bisulfate aerosols upon reaction with monomethyl amine. The ammonium bisulfate aerosols produced much less ammonia than ammonium sulfate

aerosols in a similar model atmosphere. I attribute the decrease in ammonia production to the monomethyl amine preferentially exchanging a proton with the bisulfate ion rather than the ammonium ion. Some monomethyl amine still reacts with the ammonium ions in the aerosols to produce ammonia gas (Figure 4.9). Both acidic suspensions produced equal amounts of ammonia. Therefore, the amount of ammonia produced from the acidic aerosol reaction with monomethyl amine is independent of seed solution pH. To my knowledge, the *in situ* ACSI CRDS is the first instrument to detect ammonia displaced off of ammonium bisulfate/sulfuric acid aerosols upon reaction with monomethyl amine.

Chapter 5

Summary and Conclusions

5.1. Summary of Results

The overall purpose of my research project was to develop a new instrument and experimental approach to explore interfacial reactions between atmospherically-relevant aerosols and pollutant gases in a controlled manner. The Atmospheric Cloud Simulation Instrument was designed to extend particle suspension durations in the laboratory and non-destructively monitor the gas-phase species in complex model atmospheres. The experiments described in the previous chapters accomplished the research objectives defined in Chapter 1, restated below.

1. Design an instrumental approach for exploring particle growth over extended durations.

2. Develop experimental methods that enable simultaneous monitoring of gas-phase composition and particle size distributions over time.

3. Use the instrument to study of the emission of interfacial reaction products that result from a perturbation to the atmospheric conditions.

The ACSI design afforded the ability to extend the particle suspension duration while monitoring the gas-phase composition. Fine particulate matter between 0.1–2.5 μm diameter have the longest atmospheric lifetime of up to 30 days and can travel up to thousands of kilometers.[14,19,36,37] In stationary laboratory atmospheric chambers, one-micrometer particles deposit out of the suspension in less than 5 hours.[114] The rotating chamber integrated into the ACSI increased the duration of stable 1 μm particle suspensions to over 24 hours. The chamber design provided the ability to simulate the fine particulate matter transportation through various atmospheric conditions, such as polluted areas and regions of various

levels of humidity. A cavity ring-down spectrometer was incorporated into the center axis to monitor the gas-phase composition during the simulated particle transport through a model atmosphere. See Figure 5.1 for an assembly drawing of the instrument. The first experiments using the ACSI determined the effect of humidity and particle composition on particle coagulation and heterogeneous reactions. Sections 5.1.1 and 5.1.2 summarize the results of the experiments conducted in previous chapters.

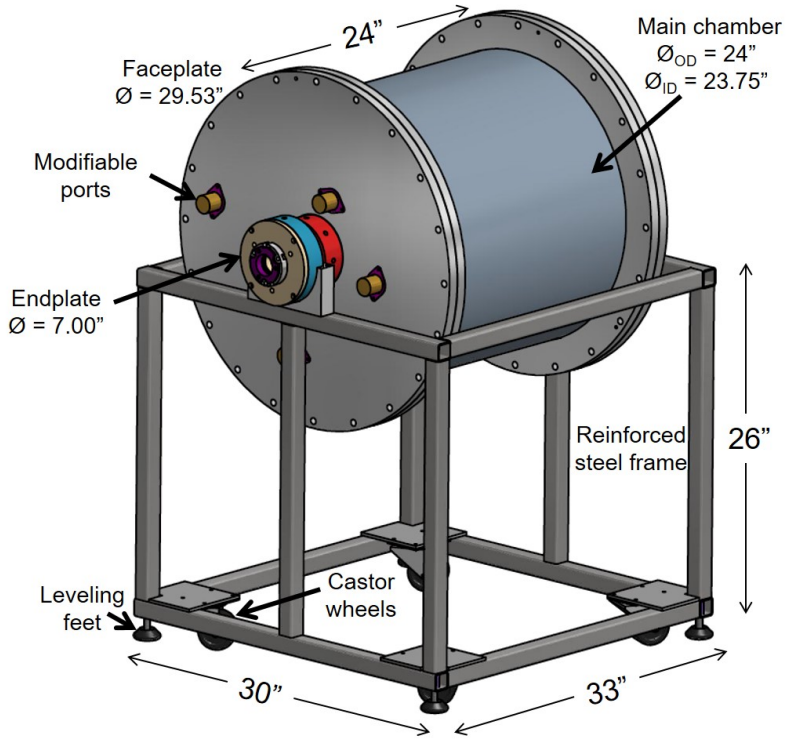

Figure 5.1: Assembly drawing of the Atmospheric Cloud Simulation Instrument. The height of the stand was determined to match the height of the cavity ring-down spectrometer optics table (not shown here). Leveling feet were used to reduce vibrations, align the CRDS, and raise the stand so it did not rest on the castor wheels. The motor, belt, gas lines and the gas-handling manifold omitted for clarity.

5.1.1. Particle Suspension

Computational models refined by our collaborators at Clarkson University predicted the high suspension efficiency of fine particulate matter in the rotating chamber incorporated into the the design of the ACSI.[112–114,119] Chapter 3 described the experiments for analyzing the particle suspension efficiencies for monodisperse 1 μm PSL particles, monodisperse 0.1

μm ammonium sulfate salt particles, and polydisperse ammonium sulfate in various model atmospheres.

The Brown and Dhaniyala model predicted large, 1 μm particles, indicative of $PM_{2.5}$, deposit via gravity in less than 5 hours in a stationary chamber but remain suspended in a chamber rotating at 1–5 RPM indefinitely.[112–114] The 0.994±.012 μm PSL particles used to test the model steadily deposited out of the suspension over 16 hours. Non-ideal flows and the sampling procedure disturb the settling particles, lengthening the expected particle suspension duration by 11 hours. The over 70% of the same particles remained suspended after 16 hours in a chamber rotating at 1–2 RPM. Figure 5.2 shows the number suspension efficiency of the PSLs in the stationary (0 RPM) and rotating chamber (1 and 2 RPM). The particles also established a uniform radial distribution, determined by sampling the suspension at four distances from the center axis.

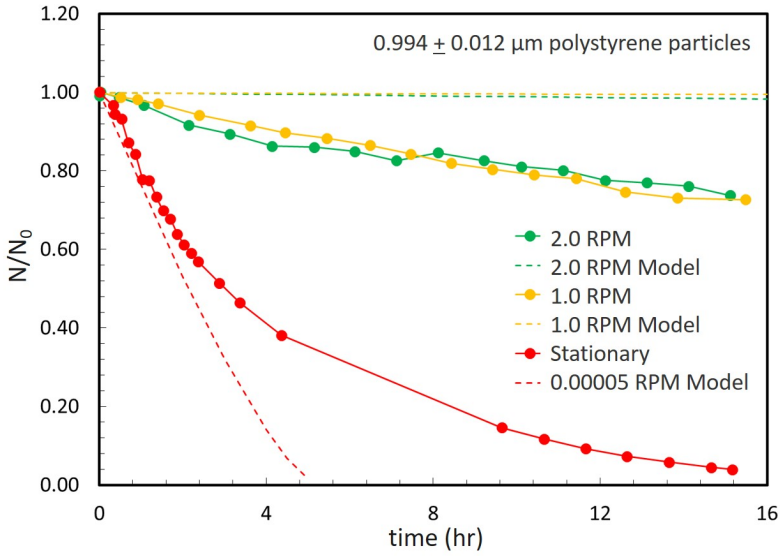

Figure 5.2: Experimental and computed long-term particle suspension efficiency (N/N_o) while the chamber rotates at 1 RPM (yellow) and 2 RPM (green) compared to a stationary chamber (red). The dashed lines correspond to the computed particle suspension efficiency calculated using mathematical models discussed in Section 2.2.1.[114] The particles are 0.994±0.012 μm polystyrene latex spheres. Each data point represents a single sampling event through all four ports simultaneously and the lines are added to help guide the eye.

The aerosol coagulation equations derived in Section 1.2.1.1 and the Brown and

Dhaniyala computational model[114] predicted low concentrations monodisperse 0.1 μm ammonium sulfate aerosols do not coagulate and remain suspended in a slowly rotating chamber. Coagulation causes an immediate decrease in the number suspension efficiency (N/N_o) and no change in the volume suspension efficiency (V/V_o). As expected, the monodisperse ammonium sulfate particles with initial concentrations less than 1×10^4 particles/cm^3 did not exhibit the signs of coagulation. The number concentration of the monodisperse aerosols at such low initial concentrations would decrease by half after >30 hours, almost 4 times longer than the experiment.

Particle concentrations greater than 1×10^5–1×10^6 particles/cm^3 exhibit coagulation detectable on an 8–10 hour experimental time scale. I introduced suspensions of ~1×10^6 particles/cm^3 solid, polydisperse ammonium sulfate into the ASCI and successfully produced conditions favorable for coagulation. The polydisperse aerosol suspensions exhibited a rapid decrease in N/N_o and almost 100% volume suspension efficiency (V/V_o), indicative of coagulation. I employed a method similar to one reported by Kim et al. that used Equation 1.14 to calculate the experimental coagulation coefficient ($\gamma\beta\overline{K}$) for a polydisperse suspension.[22] The "sticking coefficient", defined in Section 1.2.1.1, was used for the first time to quantify the difference between the experimental and the calculated coagulation coefficient for polydisperse aerosol suspensions in Section 3.4.2. For example, the polydisperse ammonium sulfate aerosols in 1.6% RH resulted in a $\gamma = 0.357$, which suggests coagulation is inhibited by repulsive forces from like surface charges.

Prior work has shown that aqueous salt droplets exhibit layers of like-charge ions, such as enhanced cation concentrations near the droplet surface.[142] The ammonium sulfate aerosols below the efflorescence relative humidity (35% RH) are solid salt particles. Therefore, I investigated the effect of surface charge on coagulation with polydisperse ammonium sulfate suspensions in model atmospheres above 35% RH to ensure the aerosols existed as aqueous droplets. The aqueous droplets in 45-50% RH exhibited sticking coefficients (γ) <0.3, indicating the coagulation slowed even more compared to the solid ammonium sulfate suspensions.

Like surface charges are known to negatively impact coagulation in particle suspensions through repulsive Coulomb forces.[16,138,143] I attribute the decrease in γ to ammonium and sulfate ions forming "heterogeneous internal structures,"[142] including a higher concentration of like-charged ions on the aerosol surface.

The addition of sulfuric acid to the ammonium sulfate seed solution produced acidic ammonium bisulfate aerosols with higher ion concentrations used to explore the effect of particle composition on the experimental coagulation coefficient. Acidic ammonium bisulfate does not effloresce,[129,131,139] therefore the aerosols are aqueous droplets with higher concentrations of ions able to form enhanced surface concentrations.[142] I hypothesized that the coagulation of acidic ammonium bisulfate aerosols is inhibited more than the ammonium sulfate aqueous aerosol coagulation. Figure 5.3 relates the decrease in coagulation sticking coefficient (γ) in the acidic ammonium bisulfate aerosols compared to the ammonium sulfate particles to relative humidities ranging from ~2% RH to >55% RH.

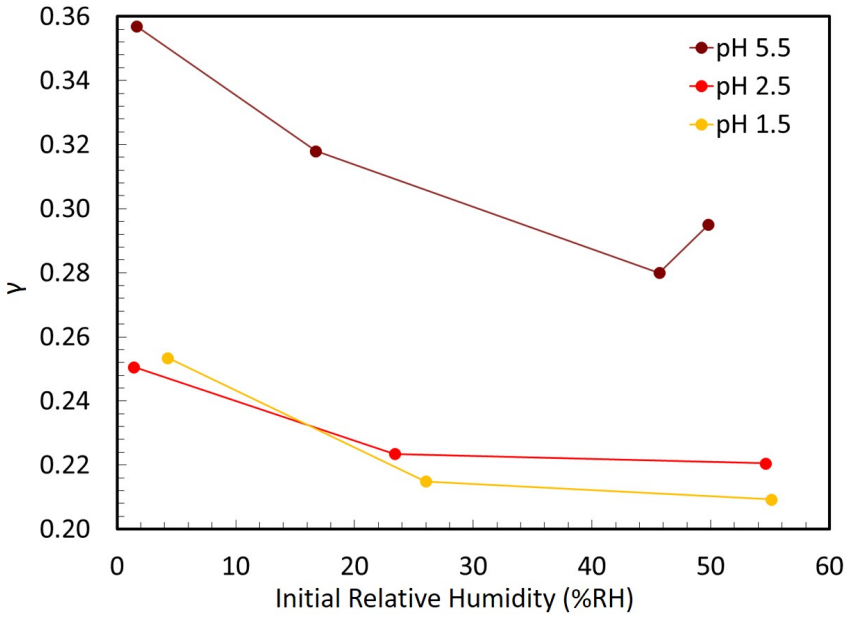

Figure 5.3: Graphical relationship between the coagulation coefficient scalar, γ, and relative humidity for the ammonium sulfate seed solution (dark red, 5.5 pH), and two ammonium sulfate/sulfuric acid seed solutions (red, 2.5 pH and yellow, 1.5 pH).

Every trial of acidic ammonium bisulfate aerosols resulted in a ~10–25% decrease in

the experimental coagulation sticking coefficient (γ). Pandis and Seinfeld reported a derivation for quantifying the effect of Coulomb surface charges on coagulation efficiency.[143] The derivation used the potential energy between two similarly sized, charged particles with some distance (r) between particle centers to calculate a Coulomb correction factor (W_c) for the coagulation coefficient (Equation 5.1). See Appendix A.1.3 for the derivation of $1/W_c$. Under the assumption that the sticking coefficients I calculated are only dependent on surface charge, I hypothesize that the sticking coefficients for ammonium sulfate-type suspensions in the ACSI are actually the Coulomb correction factor, $1/W_c$. To the best of my knowledge, this is the first time experimental coagulation coefficients and the proposed Coulomb correction factors have been quantified for coagulating polydisperse particle suspensions in a rotating chamber.

$$J_{1,2} = \frac{1}{W_c} K_{1,2} N_1 N_2 \tag{5.1}$$

5.1.2. Heterogeneous Reactions

Atmospheric aerosol aging consists of many processes, most notably heterogeneous chemistry at the gas-particle interface. Some heterogeneous reactions produce or displace gases initially in the bulk material of a particle back into the atmosphere.[74,98,99] The trace amounts of gases released from particulate matter is difficult to detect with common analytical techniques. The ASCI employed a sensitive, multi-pass spectroscopy, CRDS, along the center axis to monitor the evolution of ppb-level gases from a model atmosphere perturbed with a pollutant.

Prior work reported ammonium sulfate, a common secondary inorganic aerosol, releases ammonia upon reaction with gaseous alkyl amines with >5% RH present.[99,100,120,146] Experiments described in Section 4.2 determined the ACSI successfully detected ammonia gas release during a heterogeneous reaction involving ammonium sulfate and monomethyl amine in >60% RH. As I decreased the relative humidity in the model atmosphere, much less am-

monia was displaced by the reaction. For the first time, no detectable ammonia was released off of the ammonium sulfate particles at 15% RH. I hypothesize the decrease in ammonia is related to the phase state of the aerosols at the three different relative humidities. Ammonium sulfate effloresces at 35 % RH,[129] therefore the aerosols are expected to be aqueous droplets during the 60% RH experiment and solid salt particles during the 15% RH and 30% RH experiments. From my findings, I hypothesize that monomethyl amine can react with the bulk material of the aqueous ammonium sulfate droplets at 60% RH, which produced more ammonia than the solid particles.

I investigated the effect of slight changes in ammonium sulfate particle composition on the displacement of ammonia upon reaction with alkyl amines. The ammonium sulfate particle seed solution was acidified with sulfuric acid to form ammonium bisulfate/sulfuric acid aerosols. Ammonium bisulfate represents the ammonium sulfate aerosols not chemically neutralized by ammonia in the atmosphere.[86] Qiu et al. reported ammonium bisulfate in a flow reactor tube produced no detectable ammonia upon reaction with alkyl amines and compared the reaction to the reactive uptake of amines onto concentrated sulfuric acid.[99] For the first time to my knowledge, the ACSI CRDS detected a trace amount of ammonia when ammonium bisulfate/sulfuric aerosols in >55% RH reacted with monomethyl amine. Figure 5.4 shows the spectrum of ammonia detected from the heterogeneous reaction involving ammonium bisulfate aerosols. I hypothesize that most of the monomethyl amine will undergo a reactive uptake onto the ammonium bisulfate aerosols, however some small amount ammonium ions undergo proton exchange with the monomethyl amine to produce ammonia gas, independent of aerosol pH.

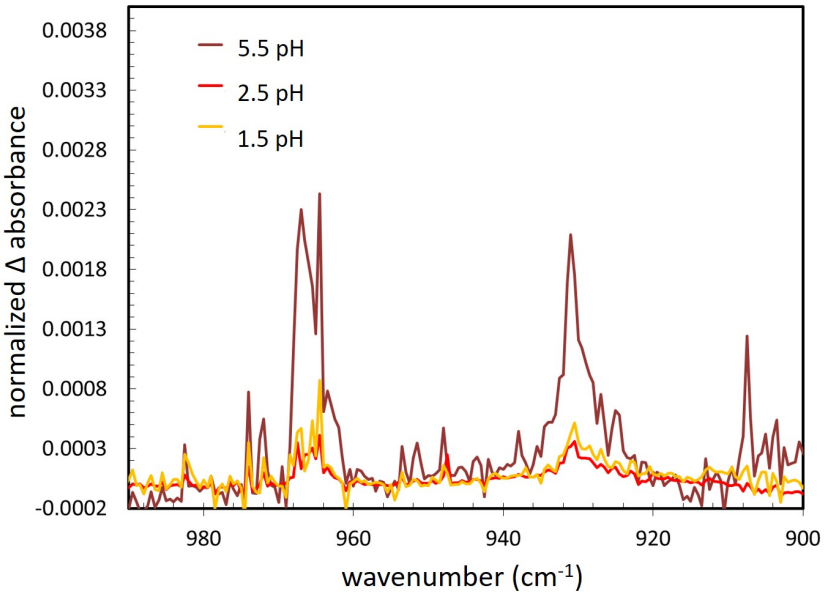

Figure 5.4: Ammonia gas produced from reaction of monomethyl amine with ammonium sulfate at varying levels of acidity in 55–60% RH. All spectra are normalized to the ammonium sulfate particle mass concentration for each trial.

5.2. Future Studies

Future research involving the ASCI will further develop the understanding of particle phase state, composition and charge on coagulation and heterogeneous reactions. For example, incorporating a neutralizer after aerosol generation prior to introduction into the main chamber will provide more insight into the effect of surface charge on coagulation without changing the particle phase or composition. The use of other salts, such as Na_2SO_4 or NH_4HSO_4, could be employed to verify the effects of composition and charge on coagulation. Such experiments will provide insight into the effect of particle phase and charge on atmospheric lifetimes of aerosols due to coagulation and eventually deposition. Alternate inorganic salt suspensions, such as Na_2SO_4 or NH_4HSO_4, could also provide more information on the heterogeneous reaction of monomethyl amine with aerosols. For example, I hypothesize aqueous droplets containing NH_4HSO_4 should exhibit similar coagulation kinetics and ammonia release upon exposure to alkyl amines compared to the acidic ammonium sulfate experiments described in Section 3.5 and Section 4.4. Finally, particle collection and scanning

electron microscope analysis *ex situ* will provide further insight into particle coagulation and composition in various model atmospheres as a function of particle shape and phase state.

5.3. Concluding Remarks

The unique, custom design of the Atmospheric Cloud Simulation Instrument allows for exploration of atmospheric aerosol chemistry. I combined a rotating main chamber and a sensitive, multi-pass spectroscopic technique to study aerosol aging over longer durations. The rotating main chamber successfully prolonged suspension durations for various particle sizes and compositions when compared to a stationary chamber. I demonstrated the ACSI's spectroscopic sensitivity with the identification of gas-phase products using mid-infrared spectroscopy while monitoring heterogeneous chemistry *in situ*. I explored how different model atmospheric conditions, such as humidity, particle composition and the presence of volatile organic compounds, affect particle dynamics and the release of trace amounts of ammonia from ammonium sulfate aerosols.

Bibliography

[1] Tao, Y.; Ye, X.; Jiang, S.; Yang, X.; Chen, J.; Xie, Y.; Wang, R. Effects of amines on particle growth observed in new particle formation events. *Journal of Geophysical Research: Atmospheres* **2016**, *121*, 324–335.

[2] Henschel, H.; Kurtén, T.; Vehkamäki, H. Computational study on the effect of hydration on new particle formation in the sulfuric acid/ammonia and sulfuric acid/dimethylamine systems. *Journal of Physical Chemistry A* **2016**, *120*, 1886–1896.

[3] Galloway, M. M.; Powelson, M. H.; Sedehi, N.; Wood, S. E.; Millage, K. D.; Kononenko, J. A.; Rynaski, A. D.; De Haan, D. O. Secondary organic aerosol formation during evaporation of droplets containing atmospheric aldehydes, amines, and ammonium sulfate. *Environmental Science and Technology* **2014**, *48*, 14417–14425.

[4] Hawkins, L. N.; Lemire, A. N.; Galloway, M. M.; Corrigan, A. L.; Turley, J. J.; Espelien, B. M.; De Haan, D. O. Maillard chemistry in clouds and aqueous aerosol as a source of atmospheric humic-like substances. *Environmental Science and Technology* **2016**, *50*, 7443–7452.

[5] Liggio, J.; Li, S. M. Organosulfate formation during the uptake of pinonaldehyde on acidic sulfate aerosols. *Geophysical Research Letters* **2006**, *33*, L13808.

[6] De Haan, D. O. et al. Brown carbon production in ammonium- or amine-containing aerosol particles by reactive uptake of methylglyoxal and photolytic cloud cycling. *Environmental Science and Technology* **2017**, *51*, 7458–7466.

[7] Kroll, J. H.; Ng, N. L.; Murphy, S. M.; Varutbangkul, V.; Flagan, R. C.; Seinfeld, J. H. Chamber studies of secondary organic aerosol growth by reactive uptake of simple carbonyl compounds. *Journal of Geophysical Research Atmospheres* **2005**, *110*, 1–10.

[8] Kong, L.; Yang, Y.; Zhang, S.; Zhao, X.; Du, H.; Fu, H.; Zhang, S.; Cheng, T.; Yang, X.; Chen, J.; Wu, D.; Shen, J.; Hong, S.; Jiao, L. Observations of linear dependence between sulfate and nitrate in atmospheric particles. *Journal of Geophysical Research* **2014**, *119*, 341–361.

[9] Wilmsmeyer, A. R.; Gordon, W. O.; Davis, E. D.; Mantooth, B. A.; Lalain, T. A.; Morris, J. R. Multifunctional ultra-high vacuum apparatus for studies of the interactions of chemical warfare agents on complex surfaces. *Review of Scientific Instruments* **2014**, *85*, 14101–14705.

[10] Tang, M. J.; Schuster, G.; Crowley, J. N. Heterogeneous reaction of N_2O_5 with illite and Arizona test dust particles. *Atmospheric Chemistry and Physics* **2014**, *14*, 245–254.

[11] Li, Q.; Hu, D.; Leungsakul, S.; Kamens, R. M. Large outdoor chamber experiments and computer simulations: (I) Secondary organic aerosol formation from the oxidation of a mixture of d-limonene and α-pinene. *Atmospheric Environment* **2007**, *41*, 9341–9352.

[12] Wang, Y.; Hopke, P. K.; Chalupa, D. C.; Utell, M. J. Long-term study of urban ultrafine particles and other pollutants. *Atmospheric Environment* **2011**, *45*, 7672–7680.

[13] Pandis, J.; Seinfeld, S. *Atmospheric Chemistry and Physics: From Air Pollution to Climate Change*, 2nd ed.; John Wiley & Sons, Inc.: New York, NY, 2006; pp 21–45.

[14] Heintzenberg, J. Fine particles in the global troposphere: A review. *Tellus B* **1989**, *41 B*, 149–160.

[15] Pandis, S. N.; Seinfeld, J. H. *Atmospheric Chemistry and Physics: From Air Pollution to Climate Change*, 2nd ed.; John Wiley & Sons, Inc.: Hoboken, NJ, 2006.

[16] Hinds, W. C. *Aersol Technology*, 2nd ed.; John Wiley & Sons, Inc.: United States of America, 1999; p 446.

[17] Pandis, J.; Seinfeld, S. *Atmospheric Chemistry and Physics: From Air Pollution to Climate Change*, 2nd ed.; John Wiley & Sons, Inc.: New York, NY, 2006; Chapter 8, pp 350–395.

[18] Whitby, K. T. The physical characteristics of sulfur aerosols. *Atmospheric Environment (1967)* **1978**, *12*, 135–159.

[19] Jaenicke, R. The role of organic material in atmospheric aerosols. *Pure and Applied Geophysics* **1978**, *116*, 283–292.

[20] Ogren, J. A.; Charlson, R. J. Elemental carbon in the atmosphere: cycle and lifetime. *Tellus B: Chemical and Physical Meteorology* **1983**, *35*, 241–254.

[21] Fuchs, N. A. The Mechanics of Aerosols. *Pergamon Press* **1964**, *146*, 1033–1034.

[22] Kim, D. H. S. H. S.; Park, S. H.; Song, Y. M.; Kim, D. H. S. H. S.; Lee, K. W. Brownian coagulation of polydisperse aerosols in the transition regime. *Journal of Aerosol Science* **2003**, *34*, 859–868.

[23] Lee, K. W. Change of particle size distribution during Brownian coagulation. *Journal of Colloid and Interface Science* **1983**, *92*, 315–325.

[24] Lee, K. W.; Chen, H. Coagulation rate of polydisperse particles. *Aerosol Science and Technology* **1984**, *3*, 327–334.

[25] Zebel, G. In *Aerosol Science*; Davies, C. N., Ed.; 1966; Chapter 2.

[26] Pandis, S. N.; Seinfeld, J. H. *Atmospheric Chemistry and Physics: From Air Pollution to Climate Change*, 2nd ed.; John Wiley & Sons, Inc.: Hoboken, NJ, 2006; Chapter 14, pp 628–690.

[27] Zender, C. S.; Bian, H.; Newman, D. Mineral Dust Entrainment and Deposition (DEAD) model: Description and 1990s dust climatology. *Journal of Geophysical Research* **2003**, *108*, 4416.

[28] Gong, S. L.; Barrie, L. A.; Blanchet, J.; von Salzen, K.; Lohmann, U.; Lesins, G.; Spacek, L.; Zhang, L. M.; Girard, E.; Lin, H.; Leaitch, R.; Leighton, H.; Chylek, P.; Huang, P. Canadian Aerosol Module: A size-segregated simulation of atmospheric aerosol processes for climate and air quality models 1. Module development. *Journal of Geophysical Research* **2003**, *108*, 4007.

[29] Kiehl, J.; Rodhe, H. In *Aerosol forcing on climate*; Charlson, R. J., Heintzenberg, J., Eds.; John Wiley & Sons, Inc.: Wiley, NY, 1995; pp 281–296.

[30] Liao, H.; Adams, P. J.; Chung, S. H.; Seinfeld, J. H.; Mickley, L. J.; Jacob, D. J. Interactions between tropospheric chemistry and aerosols in a unified general circulation model. *Journal of Geophysical Research* **2003**, *108*, 4001.

[31] Chung, S. H.; Seinfeld, J. H. Global distribution and climate forcing of carbonaceous aerosols. *Journal of Geophysical Research* **2002**, *107*, 4407.

[32] Liousse, C.; Penner, J. E.; Chuang, C.; Walton, J. J.; Eddleman, H.; Cachier, H. A global three-dimensional model study of carbonaceous aerosols. *Journal of Geophysical Research: Atmospheres* **1996**, *101*, 19411–19432.

[33] Liao, H.; Seinfeld, J. H.; Adams, P. J.; Mickley, L. J. Global radiative forcing of coupled tropospheric ozone and aerosols in a unified general circulation model. *Journal of Geophysical Research* **2004**, *109*, D16207.

[34] Ernő, M. *Fundamentals of Atmospheric Aerosol Chemistry*, 1st ed.; Akadémiai Kiadó: Budapest, Hungary, 1999; p 308.

[35] Ott, S.; Ott, A.; Martin, D.; Young, J. Analysis of trans-Atlantic Saharan dust outbreak based on satellite and GATE data. *Monthly Weather Review* **1991**, *119*, 1832–1850.

[36] Prospero, J. M.; Nees, R. T.; Uematsu, M. Deposition rate of particulate and dissolved aluminum derived from saharan dust in precipitation at Miami, Florida. *Journal of Geophysical Research* **1987**, *92*, 14723.

[37] Gray, E. T.; Monroe, B.; Elkins, K. NASA's Goddard Space Flight Center Dust Crossing. 2015; https://svs.gsfc.nasa.gov/11751.

[38] Wall, S. M.; John, W.; Ondo, J. L. Measurement of aerosol size distributions for nitrate and major ionic species. *Atmospheric Environment (1967)* **1988**, *22*, 1649–1656.

[39] Tabazadeh, A.; Jacobson, M. Z.; Singh, H. B.; Toon, O. B.; Lin, J. S.; Chatfield, R. B.; Thakur, A. N.; Talbot, R. W.; Dibb, J. E. Nitric acid scavenging by mineral and biomass burning aerosols. *Geophysical Research Letters* **1998**, *25*, 4185–4188.

[40] Jordan, C. E.; Dibb, J. E.; Anderson, B. E.; Fuelberg, H. E. Uptake of nitrate and sulfate on dust aerosols during TRACE-P. *Journal of Geophysical Research: Atmospheres* **2003**, *108*.

[41] Clarke, A. D.; Shinozuka, Y.; Kapustin, V. N.; Howell, S.; Huebert, B.; Doherty, S.; Anderson, T.; Covert, D.; Anderson, J.; Hua, X.; Moore, K. G.; McNaughton, C.; Carmichael, G.; Weber, R. Size distributions and mixtures of dust and black carbon aerosol in Asian outflow: Physiochemistry and optical properties. *Journal of Geophysical Research D: Atmospheres* **2004**, *109*, D15S09.

[42] Dibb, J. E.; Talbot, R. W.; Scheuer, E. M.; Seid, G.; Avery, M. A.; Singh, H. B. Aerosol chemical composition in Asian continental outflow during the TRACE-P campaign: Comparison with PEM-West B. *Journal of Geophysical Research: Atmospheres* **2003**, *108*.

[43] Kim, K. W.; He, Z.; Kim, Y. J. Physicochemical characteristics and radiative properties of Asian dust particles observed at Kwangju, Korea, during the 2001 ACE-Asia intensive observation period. *Journal of Geophysical Research D: Atmospheres* **2004**, *109*, D19S02.

[44] Ooki, A.; Uematsu, M. Chemical interactions between mineral dust particles and acid gases during Asian dust events. *Journal of Geophysical Research D: Atmospheres* **2005**, *110*, 1–13.

[45] Sullivan, R. C.; Guazzotti, S. A.; Sodeman, D. A.; Prather, K. A. Direct observations of the atmospheric processing of Asian mineral dust. *Atmospheric Chemistry and Physics* **2007**, *7*, 1213–1236.

[46] Fitzgerald, J. W. Marine aerosols: A review. 1991; https://www.sciencedirect.com/science/article/pii/096016869190050H.

[47] Raemdonck, H.; Maenhaut, W.; Andreae, M. O. Chemistry of marine aerosol over the tropical and equatorial Pacific. *Journal of Geophysical Research* **1986**, *91*, 8623.

[48] Andreae, M. O.; Charlson, R. J.; Bruynseels, F.; Storms, H.; Van Grieken, R.; Maenhaut, W. Internal mixture of sea salt, silicates, and excess sulfate in marine aerosols. *Science* **1986**, *232*, 1620–1623.

[49] Prospero, J. M. Mineral and sea salt aerosol concentrations in various ocean regions. *Journal of Geophysical Research* **1979**, *84*, 725.

[50] Savoie, D. L.; Prospero, J. M.; Nees, R. T. Nitrate, non-sea-salt sulfate, and mineral aerosol over the northwestern Indian Ocean. *Journal of Geophysical Research* **1987**, *92*, 933–942.

[51] Savoie, D. L.; Prospero, J. M. Comparison of oceanic and continental sources of non-sea-salt sulphate over the Pacific Ocean. *Nature* **1989**, *339*, 685–687.

[52] Blanchard, D. C.; Woodcock, A. H. Bubble formation and modification in the sea and its meteorological significance. *Tellus* **1957**, *9*, 145–158.

[53] Monahan, E. C.; Fairall, C. W.; Davidson, K. L.; Boyle, P. J. Observed inter-relations between 10 m winds, ocean whitecaps and marine aerosols. *Quarterly Journal of the Royal Meteorological Society* **1983**, *109*, 379–392.

[54] Mészáros, A.; Vissy, K. Concentration, size distribution and chemical nature of atmospheric aerosol particles in remote oceanic areas. *Journal of Aerosol Science* **1974**, *5*, 101–109.

[55] Gras, J. L.; Ayers, G. P. Marine aerosol at southern mid-latitudes. *Journal of Geophysical Research* **1983**, *88*, 10661.

[56] Parungo, F. P.; Nagamoto, C. T.; Madel, R.; Rosinski, J.; Haagenson, P. L. Marine aerosols in pacific upwelling regions. *Journal of Aerosol Science* **1987**, *18*, 277–290.

[57] Savoie, D. L.; Prospero, J. M. Particle size distribution of nitrate and sulfate in the marine atmosphere. *Geophysical Research Letters* **1982**, *9*, 1207–1210.

[58] Parungo, F.; Nagamoto, C.; Harris, J. M.; Rosenwasser, B.; Ruhnke, L. H.; (U.S.)., E. R. L.; Environmental Sciences Group, *Analyses of aerosol and precipitation samples collected during a transatlantic research cruise*; 1984.

[59] Parungo, F. P.; Nagamoto, C. T.; Rosinski, J.; Haagenson, P. L. A study of marine aerosols over the Pacific Ocean. *Journal of Atmospheric Chemistry* **1986**, *4*, 199–226.

[60] Savoie, D. L.; Prospero, J. M.; Merrill, J. T.; Uematsu, M. Nitrate in the atmospheric boundary layer of the tropical South Pacific: Implications regarding sources and transport. *Journal of Atmospheric Chemistry* **1989**, *8*, 391–415.

[61] Zhu, Y.; Hinds, W. C.; Kim, S.; Shen, S.; Sioutas, C. Study of ultrafine particles near a major highway with heavy-duty diesel traffic. *Atmospheric Environment* **2002**, *36*, 4323–4335.

[62] Jimenez, J. L. et al. Evolution of organic aerosols in the atmosphere. *Science* **2009**, *326*, 1525–1529.

[63] Chang, S. G.; Brodzinsky, R.; Gundel, L. A.; Novakov, T. *Particulate Carbon*; Springer US: Boston, MA, 1982; pp 159–181.

[64] Robinson, A. L.; Donahue, N. M.; Shrivastava, M. K.; Weitkamp, E. A.; Sage, A. M.; Grieshop, A. P.; Lane, T. E.; Pierce, J. R.; Pandis, S. N. Rethinking organic aerosols: Semivolatile emissions and photochemical aging. *Science* **2007**, *315*, 1259–1262.

[65] Carlton, A. G.; Pinder, R. W.; Bhave, P. V.; Pouliot, G. A. To what extent can biogenic SOA be controlled? *Environmental Science and Technology* **2010**, *44*, 3376–3380.

[66] Hahn, J. Organic constituents of natural aerosols. *Annals of the New York Academy of Sciences* **1980**, *338*, 359–376.

[67] Simoneit, B. R.; Mazurek, M. A. Organic matter of the troposphere II. Natural background of biogenic lipid matter in aerosols over the rural western united states. *Atmospheric Environment (1967)* **1982**, *16*, 2139–2159.

[68] Graedel, T. E.; Hawkins, D. T.; Claxton, L. D. *Atmospheric chemical compounds: sources, occurrence, and bioassay*; Academic Press, 1986; p 732.

[69] Rogge, W. F.; Hildemann, L. M.; Mazurek, M. A.; Cass, G. R.; Simoneit, B. R. T. Sources of fine organic aerosol. 2. Noncatalyst and catalyst-equipped automobiles and heavy-duty diesel trucks. *Environmental Science & Technology* **1993**, *27*, 636–651.

[70] Rogge, W. F.; Hildemann, L. M.; Mazurek, M. A.; Cass, G. R.; Simoneit, B. R. T. Sources of fine organic aerosol 3. Road dust, tire debris, and organometallic brake lining dust: roads as sources and sinks. *Environmental Science & Technology* **1993**, *27*, 1892–1904.

[71] Rogge, W. F.; Hildemann, L. M.; Mazurek, M. A.; Cass, G. R.; Simoneit, B. R. T. Sources of fine organic aerosol 4. Particulate abrasion products from leaf surfaces of urban plants. *Environmental Science & Technology* **1993**, *27*, 2700–2711.

[72] Kelly, J. T.; Chuang, C. C.; Wexler, A. S. Influence of dust composition on cloud droplet formation. *Atmospheric Environment* **2007**, *41*, 2904–2916.

[73] Plaza, J.; Pujadas, M.; Gómez-Moreno, F.; Sánchez, M.; Artíñano, B. Mass size distributions of soluble sulfate, nitrate and ammonium in the Madrid urban aerosol. *Atmospheric Environment* **2011**, *45*, 4966–4976.

[74] Nozière, B.; Dziedzic, P.; Córdova, A. Inorganic ammonium salts and carbonate salts are efficient catalysts for aldol condensation in atmospheric aerosols. *Physical Chemistry Chemical Physics* **2010**, *12*, 3864.

[75] Jiang, Y.; Yung, Y. L. Concentrations of tropospheric ozone from 1979 to 1992 over tropical pacific South America from TOMS data. *Science* **1996**, *272*, 714–716.

[76] Armerding, W.; Comes, F. J.; Schülke, B. O(1D) quantum yields of ozone photolysis in the UV from 300 nm to its threshold and at 355 nm. *Journal of Physical Chemistry* **1995**, *99*, 3137–3143.

[77] Pandis, S. N.; Seinfeld, J. H. *Atmospheric Chemistry and Physics: From Air Pollution to Climate Change*, 2nd ed.; John Wiley & Sons, Inc.: Hoboken, NJ, 2006; Chapter 4, pp 98–137.

[78] Pandis, S. N.; Seinfeld, J. H. *Atmospheric Chemistry and Physics: From Air Pollution to Climate Change*, 2nd ed.; John Wiley & Sons, Inc.: Hoboken, NJ, 2006; Chapter 6, pp 204–283.

[79] Houghton, J.; Filho, L. M.; Callander, B.; Harris, N.; Kattenberg, A.; Maskell, K. *Climate Change 1995: The Science of Climate Cliange*; Cambridge University Press, 1995; p 572.

[80] Lurmann, F. W.; Main, H. H. *Analysis of the Ambient VOC Data Collected in the Southern California Air Quality Study*; 1992.

[81] Chameides, W. L. Ozone precursor relationships in the ambient atmosphere. *Journal of Geophysical Research* **1992**, *97*, 6037–6055.

[82] Pandis, S. N.; Harley, R. A.; Cass, G. R.; Seinfeld, J. H. Secondary organic aerosol formation and transport. *Atmospheric Environment. Part A. General Topics* **1992**, *26*, 2269–2282.

[83] Bouwman, A. F.; Lee, D. S.; Asman, W. A.; Dentener, F. J.; Van Der Hoek, K. W.; Olivier, J. G. A global high-resolution emission inventory for ammonia. *Global Biogeochemical Cycles* **1997**, *11*, 561–587.

[84] Ge, X.; Wexler, A. S.; Clegg, S. L. Atmospheric amines - Part I. A review. *Atmospheric Environment* **2011**, *45*, 524–546.

[85] Müller, C.; Iinuma, Y.; Karstensen, J.; Pinxteren, D. V.; Lehmann, S.; Gnauk, T.; Herrmann, H. Seasonal variation of aliphatic amines at the Cape Verde Islands. *Atmos. Chem. Phys* **2009**, *9*, 4318.

[86] Youn, J. S.; Crosbie, E.; Maudlin, L. C.; Wang, Z.; Sorooshian, A. Dimethylamine as a major alkyl amine species in particles and cloud water: Observations in semi-arid and coastal regions. *Atmospheric Environment* **2015**, *122*, 250–258.

[87] Hellén, H.; Kieloaho, A.-J.; Hakola, H. Gas-phase alkyl amines in urban air; comparison with a boreal forest site and importance for local atmospheric chemistry. *Atmospheric Environment* **2014**, *94*, 192–197.

[88] Wang, Y.; Zhang, J.; Marcotte, A. R.; Karl, M.; Dye, C.; Herckes, P. Fog chemistry at three sites in Norway. *Atmospheric Research* **2015**, *151*, 72–81.

[89] Council, N. R. *Rethinking the Ozone Problem in Urban and Regional Air Pollution*; The National Academy Press: Washington, DC, 1991.

[90] Goodman, A. L.; Bernard, E. T.; Grassian, V. H. Spectroscopic study of nitric acid and water adsorption on oxide particles: Enhanced nitric acid uptake kinetics in the presence of adsorbed water. *Journal of Physical Chemistry A* **2001**, *105*, 6443–6457.

[91] Baltrusaitis, J.; Schuttlefield, J.; Jensen, J. H.; Grassian, V. H. FTIR spectroscopy combined with quantum chemical calculations to investigate adsorbed nitrate on aluminium oxide surfaces in the presence and absence of co-adsorbed water. *Physical Chemistry Chemical Physics* **2007**, *9*, 4970–4980.

[92] Fairlie, T. D.; Jacob, D. J.; Dibb, J. E.; Alexander, B.; Avery, M. A.; Van Donkelaar, A.; Zhang, L. Impact of mineral dust on nitrate, sulfate, and ozone in transpacific Asian pollution plumes. *Atmospheric Chemistry and Physics* **2010**, *10*, 3999–4012.

[93] Andreae, M. O.; Crutzen, P. J. Atmospheric aerosols: Biogeochemical sources and role in atmospheric chemistry. *Science* **1997**, *276*, 1052–1058.

[94] Berresheim, H.; Wine, P. H.; Davis, D. D. *Composition, Chemistry, and Climate of the Atmosphere*; Van Nostrand Reinhold, 1995; pp 251–307.

[95] Dentener, F. J.; Crutzen, P. J. Reaction of N_2O_5 on tropospheric aerosols: impact on the global distributions of NO_x, O_3, and OH. *Journal of Geophysical Research* **1993**, *98*, 7149–7163.

[96] Evans, M. J.; Jacob, D. J. Impact of new laboratory studies of N_2O_5 hydrolysis on global model budgets of tropospheric nitrogen oxides, ozone, and OH. *Geophysical Research Letters* **2005**, *32*, 1–4.

[97] Brown, S. S.; Ryerson, T. B.; Wollny, A. G.; Brock, C. A.; Peltier, R.; Sullivan, A. P.; Weber, R. J.; Dubé, W. P.; Trainer, M.; Meagher, J. F.; Fehsenfeld, F. C.; Ravishankara, A. R. Variability in nocturnal nitrogen oxide processing and its role in regional air quality. *Science* **2006**, *311*, 67–70.

[98] Romanías, M. N.; Zeineddine, M. N.; Gaudion, V.; Lun, X.; Thévenet, F.; Riffault, V. Heterogeneous interaction of isopropanol with natural Gobi dust. *Environmental Science and Technology* **2016**, *50*, 11714–11722.

[99] Qiu, C.; Wang, L.; Lal, V.; Khalizov, A. F.; Zhang, R. Heterogeneous reactions of alkylamines with ammonium sulfate and ammonium bisulfate. *Environmental Science & Technology* **2011**, *45*, 4748–4755.

[100] Chu, Y.; Chan, C. K. Reactive uptake of dimethylamine by ammonium sulfate and ammonium sulfate–sucrose mixed particles. *The Journal of Physical Chemistry A* **2017**, *121*, 206–215.

[101] Lederer, M. R.; Staniec, A. R.; Coates Fuentes, Z. L.; Van Ry, D. A.; Hinrichs, R. Z. Heterogeneous reactions of limonene on mineral dust: Impacts of adsorbed water and nitric acid. *The Journal of Physical Chemistry A* **2016**, *120*, 9545–9556.

[102] Usher, C. R.; Michel, A. E.; Grassian, V. H. Reactions on Mineral Dust. *Chemical Reviews* **2003**, *103*, 4883–4939.

[103] Styler, S. A.; Donaldson, D. J. Photooxidation of atmospheric alcohols on laboratory proxies for mineral dust. *Environmental Science and Technology* **2011**, *45*, 10004–10012.

[104] Chen, D.; Ouyang, S.; Ye, J. Photocatalytic degradation of isopropanol over $PbSnO_3$ nanostructures under visible light irradiation. *Nanoscale Research Letters* **2009**, *4*, 274–280.

[105] Barakat, C.; Gravejat, P.; Guaitella, O.; Thévenet, F.; Rousseau, A. Oxidation of isopropanol and acetone adsorbed on TiO_2 under plasma generated ozone flow: Gas phase and adsorbed species monitoring. *Applied Catalysis B: Environmental* **2014**, *147*, 302–313.

[106] You, Y. et al. Atmospheric amines and ammonia measured with a chemical ionization mass spectrometer (CIMS). *Atmospheric Chemistry and Physics* **2014**, *14*, 12181–12194.

[107] Yu, H.; McGraw, R.; Lee, S. H. Effects of amines on formation of sub-3 nm particles and their subsequent growth. *Geophysical Research Letters* **2012**, *39*, n/a–n/a.

[108] Angeling, S.; Suess, D. T.; Prather, K. A. Formation of aerosol particles from reactions of secondary and tertiary alkylamines: Characterization by aerosol time-of-flight mass spectrometry. *Environmental Science and Technology* **2001**, *35*, 3130–3138.

[109] Murphy, S. M.; Sorooshian, A.; Kroll, J. H.; Ng, N. L.; Chhabra, P.; Tong, C.; Surratt, J. D.; Knipping, E.; Flagan, R. C.; Seinfeld, J. H. Secondary aerosol formation from atmospheric reactions of aliphatic amines. *Atmospheric Chemistry and Physics* **2007**, *7*, 2313–2337.

[110] Tang, X.; Price, D.; Praske, E.; Lee, S. A.; Shattuck, M. A.; Purvis-Roberts, K.; Silva, P. J.; Asa-Awuku, A.; Cocker, D. R. NO_3 radical, OH radical and O_3-initiated secondary aerosol formation from aliphatic amines. *Atmospheric Environment* **2013**, *72*, 105–112.

[111] Verreault, D.; Killeen, S. Z.; Redmann, R. K.; Roy, C. J.; Roy, C. J. Susceptibility of monkeypox virus aerosol suspensions in a rotating chamber. *J Virol Methods* **2013**, *187*, 333–337.

[112] Gruel, R. L.; Reid, C. R.; Allemann, R. T. The optimum rate of drum rotation for aerosol aging. *Journal of Aerosol Science* **1987**, *18*, 17–22.

[113] Asgharian, B.; Moss, O. R. Particle suspension in a rotating drum chamber when the influence of gravity and rotation are both significant. *Aerosol Science and Technology* **1992**, *17*, 263–277.

[114] Brown, M.; Dhaniyala, S. A model for particle residence time in a rotating aerosol chamber. 2019; Manuscript in preparation.

[115] Mazurenka, M.; Orr-Ewing, A. J.; Peverall, R.; Ritchie, G. A. D. Cavity ring-down and cavity enhanced spectroscopy using diode lasers. *Annual Reports Section "C" (Physical Chemistry)* **2005**, *101*, 100.

[116] Gupta, M. Highly-precise measurements of ambient oxygen using near-infrared cavity-enhanced laser absorption spectrometry. *Analytical Chemistry* **2012**, *84*, 7987–7991.

[117] Sun, M.; Jiang, C.; Gong, Z.; Zhao, X.; Chen, Z.; Wang, Z.; Kang, M.; Li, Y.; Wang, C. A fully integrated standalone portable cavity ringdown breath acetone analyzer. *Review of Scientific Instruments* **2015**, *86*, 095003.

[118] Sadiek, I.; Shi, Q.; Wallace, D. W.; Friedrichs, G. Quantitative mid-infrared cavity ringdown detection of methyl iodide for monitoring applications. *Analytical Chemistry* **2017**, *89*, 8445–8452.

[119] Goldberg, L. J.; Watkins, H. M.; Boerke, E. E.; Chatigny, M. A. The use of a rotating drum for the study of aerosols over extended periods of time. *American Journal of Epidemiology* **1958**, *68*, 85–93.

[120] Chan, L. P.; Chan, C. K. Role of the aerosol phase state in ammonia/amines exchange reactions. *Environmental Science & Technology* **2013**, *47*, 5755–5762.

[121] Baer, D. S.; Paul, J. B.; Gupta, M.; O'Keefe, A. Sensitive absorption measurements in the near-infrared region using off-axis integrated-cavity-output spectroscopy. *Applied Physics B: Lasers and Optics* **2002**, *75*, 261–265.

[122] O'Keefe, A.; Scherer, J. J.; Paul, J. B.; Saykally, R. J. *Cavity-Ringdown Spectroscopy*; American Chemical Society, 1999; Vol. 720; Chapter 6, pp 71–92.

[123] Lack, D. A.; Quinn, P. K.; Massoli, P.; Bates, T. S.; Coffman, D.; Covert, D. S.; Sierau, B.; Tucker, S.; Baynard, T.; Lovejoy, E.; Murphy, D. M.; Ravishankara, A. R. Relative humidity dependence of light absorption by mineral dust after long-range atmospheric transport from the Sahara. *Geophysical Research Letters* **2009**, *36*.

[124] Rothman, L. et al. The HITRAN 2004 molecular spectroscopic database. *Journal of Quantitative Spectroscopy and Radiative Transfer* **2005**, *96*, 139–204.

[125] Rothman, L. et al. The HITRAN2012 molecular spectroscopic database. *Journal of Quantitative Spectroscopy and Radiative Transfer* **2013**, *130*, 4–50.

[126] Goldenstein, C. S.; Miller, V. A.; Mitchell Spearrin, R.; Strand, C. L. SpectraPlot.com: Integrated spectroscopic modeling of atomic and molecular gases. *Journal of Quantitative Spectroscopy and Radiative Transfer* **2017**, *200*, 249–257.

[127] Lechevallier, L.; Vasilchenko, S.; Grilli, R.; Mondelain, D.; Romanini, D.; Campargue, A. The water vapour self-continuum absorption in the infrared atmospheric windows: New laser measurements near 3.3 and 2.0 μm. *Atmospheric Measurement Techniques* **2018**, *11*, 2159–2171.

[128] Frostling, H. A rotating drum for the study of toxic substances in aerosol form. *Journal of Aerosol Science* **1973**, *4*, 411–419.

[129] Tang, I. N.; Munkelwitz, H. R. Water activities, densities, and refractive indices of aqueous sulfates and sodium nitrate droplets of atmospheric importance. *Journal of Geophysical Research* **1994**, *99*, 18801.

[130] Xu, J.; Imre, D.; McGraw, R.; Tang, I. Ammonium sulfate: Equilibrium and metastability phase diagrams from 40 to −50 °C. *The Journal of Physical Chemistry B* **1998**, *102*, 7462–7469.

[131] Pandis, S. N.; Seinfeld, J. H. *Atmospheric Chemistry and Physics: From Air Pollution to Climate Change*, 2nd ed.; John Wiley & Sons, Inc.: Hoboken, NJ, 2006; Chapter 10, pp 434–488.

[132] Cox, A. J.; DeWeerd, A. J.; Linden, J. An experiment to measure Mie and Rayleigh total scattering cross sections. *American Journal of Physics* **2002**, *70*, 620–625.

[133] Siegel, R.; Howell, J. *Thermal radiation heat transfer*; Taylor & Francis, 2002.

[134] Sultanova, N.; Kasarova, S.; Nikolov, I. Dispersion Properties of Optical Polymers. Proceedings of the International School and Conference on Photonics. 2009; p 9.

[135] Earle, M. E.,; Pancescu, R.G.,; Cosic, B.,; ; Zasetsky, A. Y.,; Sloan, J. J. Temperature-dependent complex indices of refraction for crystalline $(NH_4)_2SO_4$. **2006**,

[136] TSI Incorporated, Scanning mobility particle sizer (SMPS) spectrometer nanoparticle aggregate mobility analysis software module. 2012; https://www.tsi.com/getmedia/b15c636e-69ce-4434-9322-31d056a10f02/SMPS-002appnote?ext=.pdf.

[137] Okuyama, K.; Kousaka, Y.; Yoshida, T. Turbulent coagulation of aerosols in a pipe flow. *Journal of Aerosol Science* **1978**, *9*, 399–410.

[138] Kim, Y.-h.; Yiacoumi, S.; Lee, I.; McFarlane, J.; Tsouris, C. Influence of radioactivity on surface charging and aggregation kinetics of particles in the atmosphere. *Environmental Science & Technology* **2014**, *48*, 182–189.

[139] Rindelaub, J. D.; Craig, R. L.; Nandy, L.; Bondy, A. L.; Dutcher, C. S.; Shepson, P. B.; Ault, A. P. Direct Measurement of pH in Individual Particles via Raman Microspectroscopy and Variation in Acidity with Relative Humidity. *Journal of Physical Chemistry A* **2016**, *120*, 911–917.

[140] Guo, H.; Sullivan, A. P.; Campuzano-Jost, P.; Schroder, J. C.; Lopez-Hilfiker, F. D.; Dibb, J. E.; Jimenez, J. L.; Thornton, J. A.; Brown, S. S.; Nenes, A.; Weber, R. J. Fine particle pH and the partitioning of nitric acid during winter in the northeastern United States. *Journal of Geophysical Research: Atmospheres* **2016**, *121*, 10,355–10,376.

[141] Chu, Y.; Chan, C. K. Role of oleic acid coating in the heterogeneous uptake of dimethylamine by ammonium sulfate particles. *Aerosol Science and Technology* **2017**, *51*, 988–997.

[142] Ault, A. P.; Guasco, T. L.; Ryder, O. S.; Baltrusaitis, J.; Cuadra-Rodriguez, L. A.; Collins, D. B.; Ruppel, M. J.; Bertram, T. H.; Prather, K. A.; Grassian, V. H. Inside versus outside: Ion redistribution in nitric acid reacted sea spray aerosol particles as determined by single particle analysis. *Journal of the American Chemical Society* **2013**, *135*, 14528–14531.

[143] Pandis, S. N.; Seinfeld, J. H. *Atmospheric Chemistry and Physics: From Air Pollution to Climate Change*, 2nd ed.; John Wiley & Sons, Inc.: New York, NY, 2006; Chapter 13, pp 588–627.

[144] Carey, F. A. *Organic Chemistry*, 2nd ed.; McGraw-Hill, Inc.: United States of America, 1992; Chapter 22, pp 895–956.

[145] Pandis, S. N.; Seinfeld, J. H. *Atmospheric Chemistry and Physics: From Air Pollution to Climate Change*, 2nd ed.; John Wiley & Sons, Inc.: New York, NY, 2006; Chapter 20, pp 932–979.

[146] Chan, L. P.; Chan, C. K. Displacement of ammonium from aerosol particles by uptake of triethylamine. *Aerosol Science and Technology* **2012**, *46*, 236–247.

Appendices

Appendix A

Supplemental Theory

A.1. Additional aerosol dynamics equations

Gas viscosity, η, is defined in Equation A.1 and depends on temperature (T), mass of the gas molecule (m), and the gas molecule collision diameter (d_m).

$$\eta = \frac{2(mk_bT)^{1/2}}{3\pi^{3/2}d_m^2} \tag{A.1}$$

The Cunningham slip correction factor, C_c, accounts for small particle 'slip' on a collisional surface.[16] The effect of slip on collisions decreases as particle size increases.

$$C_c = 1 + \frac{2.52\lambda_g}{d_p} \qquad \text{for } 0.1 < d_p < 1 \text{ μm} \tag{A.2}$$

$$C_c = 1 + \frac{\lambda_g}{d_p}\left[2.34 + 1.05\exp\left(-0.39\frac{d_p}{\lambda_g}\right)\right] \qquad \text{for } d_p < 0.1 \text{ μm} \tag{A.3}$$

Gas mean free path, λ_g, is defined in Equation A.4 where n is the gas concentration, and d_m is the collision diameter. At 760 Torr, 293 K, the λ_g of air is approximately 0.066 μm.[16]

$$\lambda_g = \frac{1}{\sqrt{2}n\pi d_m^2} \tag{A.4}$$

Fuchs (1964) provided values for a correction factor, β, to adjust the coagulation coefficient (K_o) as particle size decreases.[21]

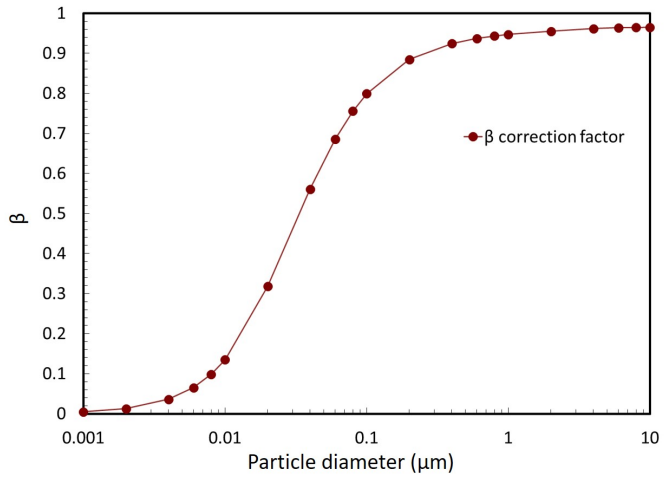

Figure A.1: Size correction factor (β) versus particle diameter for the coagulation coefficient (K) developed by Fuchs (1964).[21]

Conversion between the effective diameter (d_e) of an irregularly shaped particle and the aerodynamic diameter (d_a), where ρ_p is the particle density, ρ_0 is 1.0 g/cm^3, and χ is the shape correction factor. The shape correction factor is always greater than 1.[16]

$$d_a = d_e\left(\frac{\rho_p}{\rho_0 \chi}\right)^{1/2} \tag{A.5}$$

The following equation is the terminal electrostatic velocity (V_{TE}) for a particle of size d with some number of charges (n) in an electric field (E).[16]

$$V_{TE} = \frac{neEC_c}{3\pi\eta d} \tag{A.6}$$

A.1.1. Particle suspension computational model

See Chapter 2 for full explanations for the revisited equations.

$$\left.\frac{N}{N_0}\right|_{\text{rot}} = \exp(-2\tau\omega^2 t) \qquad \text{(2.1 revisited)}$$

$$\left.\frac{N}{N_0}\right|_{\text{grav}} = \frac{(R - r_0)^2}{R^2} \qquad \text{(2.2 revisited)}$$

$$r_0 = \frac{\tau g}{\omega} \qquad \text{(2.3 revisited)}$$

$$\left.\frac{N}{N_0}\right|_{\text{total}} = \frac{(R - r_0)^2}{R^2} \exp(-2\tau\omega^2 t) \qquad \text{(2.4 revisited)}$$

Brown and Dhaniyala used Gruel et al. and Asgharian and Moss models to derive a new model for predicting the particle suspension efficiency for a rotating chamber with the following equations. The new model redefined the particle field while the chamber rotates.

A_i is defined as the area of intersection between two offset circles (the chamber boundary and the particle field), which depicts the particle concentration as a function of rotation (Equation A.7).

$$A_i = 2R^2 \arccos\left(\frac{d}{2R}\right) - \frac{d}{2} \times \sqrt{4R^2 - d^2} \qquad \text{(A.7)}$$

Distance (d) from the chamber origin to particle field center rotating about r_0 (Equation A.8).

$$d = r_0\sqrt{(1 - \cos(\theta)^2 + \sin^2(\theta)} \qquad \text{(A.8)}$$

The rotation angle, θ, is a function of the angular velocity (ω) and time.

$$\theta = \frac{\omega t}{2\pi} \qquad \text{(A.9)}$$

Brown and Dhaniyala reported that the above equation allows for particles to reenter the particle field after leaving the chamber wall boundary. Since particles cannot reenter the particle field, Brown and Dhaniyala numerically calculated the particles deposited on the chamber walls during the first rotation. After the first rotation, the new calculation converges

with the Gruel et al. model. Brown and Dhaniyala derived an analytical solution to quantify the particles deposited on the wall during the first rotation and reenter the particle field in the area of intersection approach. The area of reentry (A_{RE}) is defined in Figure A.2. The other areas shown in Figure A.2 can be calculated using Equations A.10, A.11, and A.12. A_{RE} is calculated using Equation A.13.

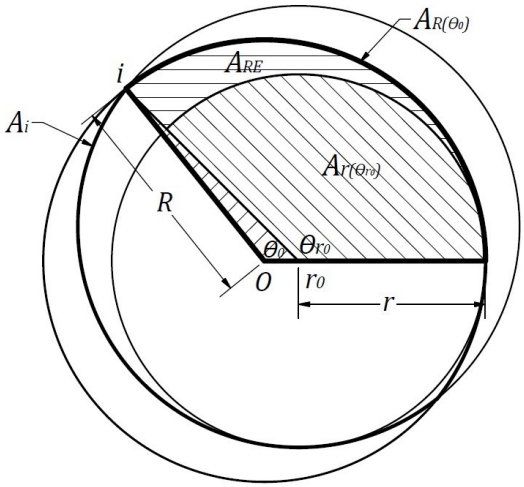

Figure A.2: The particle system at $\theta = 3\pi/2$ broken into sections to quantify the particles reentering the drum throughout the first rotation. Figure from Reference 114

$$A_{r(\theta_{r_0})} = \frac{\theta}{4}(R - r_0)^2 \tag{A.10}$$

$$A_{R(\theta_0)} = \frac{R^2}{2}\left\{\frac{\theta}{2} - \arcsin\left[\frac{r_0}{R}\sin\left(\pi - \frac{\theta}{2}\right)\right]\right\} \tag{A.11}$$

$$A_{Oir_0} = \frac{Rr_0}{2}\sin\left\{\frac{\theta}{2} - \arcsin\left[\frac{r_0}{R}\sin\left(\pi - \frac{\theta}{2}\right)\right]\right\} \tag{A.12}$$

$$A_{RE} = A_{R(\theta_0)} - A_{r(\theta_{r_0})} - A_{Oir_0} \tag{A.13}$$

Equation A.14 defines the transient particle loss during the first rotation due to gravity.

$$\left.\frac{N}{N_0}\right|_{\text{gravity}} = \frac{A_i - 2A_{RE}}{\pi R^2} \tag{A.14}$$

Equation A.15 accounts for the transient particle loss due to gravity and the particle loss due to the rotation.

$$\left.\frac{N}{N_0}\right|_{\text{both}} = \frac{A_i - 2A_{RE}}{\pi R^2} \exp(-2\tau\omega^2 t) \tag{A.15}$$

Table A.1: Summary of the equations for particle suspension efficiency (N/N_o) for all possible chamber sizes, particle sizes, rotation speeds and durations.

r_0	θ	N/N_0
$\frac{r_0}{R} < 1$	$\frac{\omega t}{2\pi} < 1$	$\frac{N}{N_0} = \frac{A_i - 2A_{RE}}{\pi R^2} \exp(-2\tau\omega^2 t)$
	$\frac{\omega t}{2\pi} > 1$	$\frac{N}{N_0} = \frac{(R-r_0)^2}{R^2} \exp(-2\tau\omega^2 t)$
$\frac{r_0}{R} < 1$	$\frac{\omega t}{\pi} < 1$	$\frac{N}{N_0} = \frac{A_i}{\pi R^2} \exp(-2\tau\omega^2 t)$
	$\frac{\omega t}{\pi} > 1$	$\frac{N}{N_0} = 0$

A.1.2. Cavity ring-down supplemental information

The following equations are from Reference 115.

Calculation for the effective path length (d) at a given wavelength.

$$d(\nu) = \frac{\tau_o(\nu)c}{L} \tag{A.16}$$

Minimum detectable change in $\tau(\nu)$ from the standard deviation of the average ring-down time.

$$\Delta\tau_{min}(\nu) = \tau_o(\nu) + 3\sigma_{\tau_o} \tag{A.17}$$

Minimum detectable absorption, α_{min}.

$$\alpha_{min} = \frac{\Delta\tau_{min}}{c\tau_o^2}\frac{L}{d} \tag{A.18}$$

Noise equivalent absorption coefficient, reported in cm^{-1} $Hz^{1/2}$, is the minimum detectable absorption coefficient during a 1 s measurement within one standard deviation. The data collection rate (f_{rep}) must be large enough to determine the relative standard deviation, $\Delta\tau_{min}/\tau_o$. The data acquisition rate for the ACSI CRDS is 1×10^7 Hz. NEA is used as a normalized value to compare various spectroscopic techniques. For example, our CRDS at 967 cm^{-1} has an NEA of approximately 4×10^{-10} cm^{-1} $Hz^{1/2}$.

$$\text{NEA} = \left(\frac{2}{f_{rep}}\right)^{1/2} \frac{\Delta\tau_{min} L}{c\tau_o^2 d} \tag{A.19}$$

$$\sigma_s = \frac{2\pi^5}{3} \frac{d_p^6}{\lambda^4} \left(\frac{(n^2-1)}{(n^2+2)}\right)^2 \tag{A.20}$$

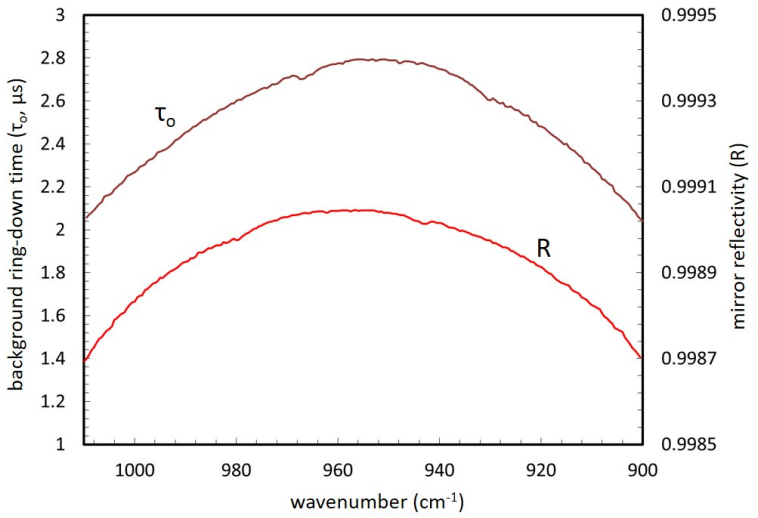

Figure A.3: Background ring-down time (τ_o) and mirror reflectivity when the chamber is filled with 700 Torr UHP N_2.

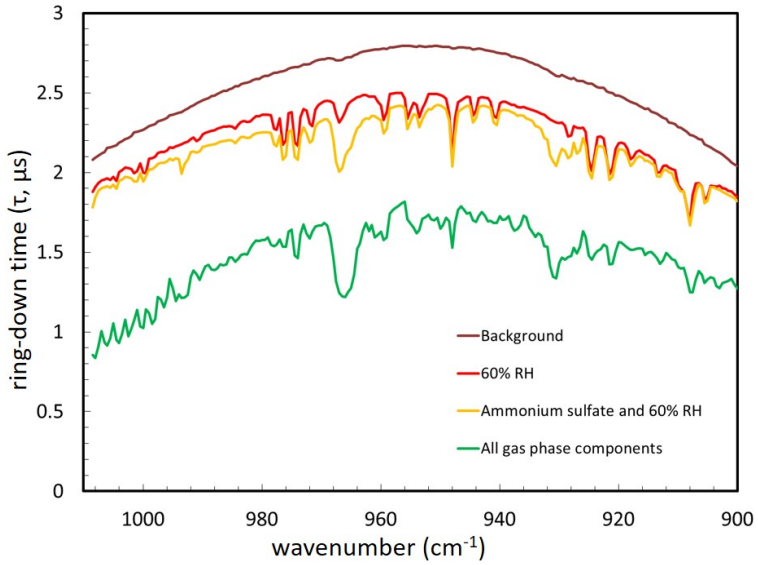

Figure A.4: Ring-down time ($\tau(\nu)$) for the background of 700 Torr nitrogen (dark red), 60% RH (red), ammonium sulfate and 60% RH (yellow), and all of the gas-phase components present after introduction of 20 s of 100 SCCM of monomethyl amine.

Wavenumber	Mirror Reflectivity	Background	Ammonium sulfate and 60% RH	All gas phase components	Wavenumber	Mirror Reflectivity	Background	Ammonium sulfate and 60% RH	All gas phase components	Wavenumber	Mirror Reflectivity	Background	60% RH	Ammonium sulfate and 60% RH	All gas phase components
900	0.997598	2.04032	1.844317	1.819915	1.27235	925.5	0.997598	2.56438	2.255017	2.171415	1.59533	951	0.997598	2.7924	2.79313	2.4929	2.412655	1.7002
900.5	0.997598	2.05156	1.862897	1.83837	1.29734	926	0.997598	2.57353	2.27948	2.21552	1.63067	951.5	0.997598	2.7924	2.79075	2.493123	2.395675	1.70768
901	0.997598	2.06393	2.00156	1.848685	1.33314	926.5	0.997598	2.57238	2.277597	2.13933	1.53472	952	0.997598	2.79075	2.79228	2.49228	2.39886	1.73505
901.5	0.997598	2.08222	1.88434	1.858065	1.31865	927	0.997598	2.57547	2.282087	2.118045	1.49107	952.5	0.997598	2.7861	2.79222	2.440163	2.37151	1.7201
902	0.997598	2.09508	1.89902	1.86909	1.31385	927.5	0.997598	2.59219	2.291987	2.18754	1.52654	953	0.997598	2.79222	2.79385	2.40088	2.33454	1.70919
902.5	0.997598	2.111146	1.900098	1.878585	1.30695	928	0.997598	2.58781	2.231473	2.10586	1.47684	953.5	0.997598	2.79385	2.345967	2.28554	2.28554	1.63948
903	0.997598	2.12537	1.91608	1.890335	1.27366	928.5	0.997598	2.59192	2.226637	2.08929	1.47021	954	0.997598	2.78915	2.42519	2.358145	2.16197
903.5	0.997598	2.13393	1.90992	1.897795	1.28726	929	0.997598	2.60232	2.292573	2.13416	1.45349	954.5	0.997598	2.791	2.438407	2.365425	2.16346	1.65346
904	0.997598	2.14619	1.913607	1.90688	1.33557	929.5	0.997598	2.61214	2.314063	2.14638	1.4663	955	0.997598	2.79264	2.39246	2.321325	2.16892	1.67892
904.5	0.997598	2.15885	1.917657	1.907035	1.34151	930	0.997598	2.60398	2.31126	2.105405	1.43258	955.5	0.997598	2.79294	2.335607	2.27123	2.27123	1.70749
905	0.997598	2.16682	1.849313	1.82303	1.33012	930.5	0.997598	2.60491	2.313437	2.04121	1.33607	956	0.997598	2.79268	2.461717	2.40301	1.8162
905.5	0.997598	2.17611	1.82912	1.80678	1.30777	931	0.997598	2.61917	2.323223	2.07147	1.34738	956.5	0.997598	2.79285	2.49747	2.416735	1.80603
906	0.997598	2.20497	1.909397	1.90774	1.35996	931.5	0.997598	2.63061	2.333593	2.107795	1.41335	957	0.997598	2.7906	2.498633	2.417585	1.79078
906.5	0.997598	2.211111	1.932573	1.92678	1.38051	932	0.997598	2.6437	2.347117	2.20587	1.53299	957.5	0.997598	2.78844	2.49977	2.413575	1.77803
907	0.997598	2.22243	1.930643	1.87326	1.32536	932.5	0.997598	2.65041	2.36121	2.217	1.53654	958	0.997598	2.78389	2.496533	2.407355	1.76501
907.5	0.997598	2.23175	1.859167	1.76495	1.24829	933	0.997598	2.66122	2.370173	2.2703	1.6042	958.5	0.997598	2.78448	2.492263	2.404765	1.74076
908	0.997598	2.23588	1.687933	1.66685	1.2493	933.5	0.997598	2.67278	2.37727	2.287745	1.61948	959	0.997598	2.7742	2.378877	2.275305	1.59308
908.5	0.997598	2.25621	1.779547	1.77498	1.334421	934	0.997598	2.67664	2.383391	2.28961	1.5945	959.5	0.997598	2.77625	2.329093	2.24374	1.57596
909	0.997598	2.26956	1.879837	1.88319	1.40268	934.5	0.997598	2.68784	2.390417	2.32338	1.62399	960	0.997598	2.77506	2.419567	2.327755	1.62692
909.5	0.997598	2.28036	1.897423	1.880345	1.39697	935	0.997598	2.69342	2.397283	2.33324	1.65489	960.5	0.997598	2.77122	2.443507	2.33865	1.60838
910	0.997598	2.28561	1.92282	1.909225	1.40672	935.5	0.997598	2.70344	2.404393	2.33929	1.71784	961	0.997598	2.77036	2.4746	2.35294	1.59401
910.5	0.997598	2.30459	2.013227	1.947315	1.4493	936	0.997598	2.70835	2.410757	2.355545	1.72971	961.5	0.997598	2.76815	2.47725	2.35701	1.67167
911	0.997598	2.31056	2.02017	1.995305	1.45631	936.5	0.997598	2.71516	2.409287	2.35891	1.67124	962	0.997598	2.76342	2.47428	2.33563	1.63005
911.5	0.997598	2.31413	2.03052	2.003335	1.48023	937	0.997598	2.71986	2.411117	2.356285	1.64601	962.5	0.997598	2.76029	2.484057	2.33841	1.68333
912	0.997598	2.33726	2.043717	2.01653	1.49613	937.5	0.997598	2.72495	2.424733	2.37289	1.63475	963	0.997598	2.75832	2.484337	2.324905	1.63615
912.5	0.997598	2.34334	2.039837	2.011165	1.4487	938	0.997598	2.72578	2.425467	2.37831	1.66294	963.5	0.997598	2.75069	2.477103	2.29108	1.55317
913	0.997598	2.35508	2.000613	1.972895	1.4265	938.5	0.997598	2.73743	2.434247	2.386815	1.72625	964	0.997598	2.74358	2.471907	2.27713	1.52002
913.5	0.997598	2.36768	1.99883	1.977085	1.46328	939	0.997598	2.7451	2.443337	2.392355	1.70752	964.5	0.997598	2.73506	2.460907	2.226175	1.35861
914	0.997598	2.37423	2.076393	2.046355	1.48208	939.5	0.997598	2.74553	2.443227	2.39151	1.70391	965	0.997598	2.72389	2.44517	2.157845	1.27447
914.5	0.997598	2.38135	2.091163	2.058155	1.50252	940	0.997598	2.74828	2.433153	2.38153	1.72501	965.5	0.997598	2.72242	2.426643	2.133735	1.24839
915	0.997598	2.39968	2.10791	2.07306	1.49803	940.5	0.997598	2.75298	2.34191	2.29649	1.68211	966	0.997598	2.718	2.384617	2.10648	1.21799
915.5	0.997598	2.39692	2.11273	2.074375	1.48188	941	0.997598	2.75896	2.356287	2.31477	1.68214	966.5	0.997598	2.70526	2.343847	2.026335	1.22336
916	0.997598	2.40852	2.125917	2.091155	1.52172	941.5	0.997598	2.76092	2.443263	2.40419	1.6964	967	0.997598	2.70221	2.31279	2.004565	1.24566
916.5	0.997598	2.41897	2.1371	2.10385	1.5245	942	0.997598	2.76418	2.465953	2.41166	1.69444	967.5	0.997598	2.70245	2.36733	2.065915	1.31719
917	0.997598	2.42999	2.129503	2.088385	1.5197	942.5	0.997598	2.76756	2.469723	2.415995	1.72852	968	0.997598	2.71221	2.435153	2.19978	1.45798
917.5	0.997598	2.43558	2.09629	2.056715	1.51562	943	0.997598	2.77324	2.471137	2.41662	1.75023	968.5	0.997598	2.71779	2.446573	2.37991	1.59152
918	0.997598	2.44426	2.08442	2.04062	1.51378	943.5	0.997598	2.77668	2.46607	2.41212	1.72685	969	0.997598	2.71705	2.45083	2.331565	1.6666
918.5	0.997598	2.45445	2.149483	2.099275	1.52932	944	0.997598	2.77407	2.3919	2.34187	1.6885	969.5	0.997598	2.71093	2.447083	2.33272	1.68367
919	0.997598	2.46611	2.179723	2.13875	1.54519	944.5	0.997598	2.77189	2.355157	2.3148	1.70055	970	0.997598	2.70904	2.437107	2.3248	1.66835
919.5	0.997598	2.47544	2.187653	2.14516	1.55876	945	0.997598	2.78077	2.471367	2.417375	1.74859	970.5	0.997598	2.70527	2.42387	2.31433	1.66772
920	0.997598	2.48124	2.18429	2.143545	1.56436	945.5	0.997598	2.78147	2.475303	2.41869	1.74294	971	0.997598	2.69857	2.393563	2.286895	1.66238
920.5	0.997598	2.48363	2.147143	2.079045	1.50465	946	0.997598	2.78509	2.466063	2.406615	1.76511	971.5	0.997598	2.68897	2.291803	2.19843	1.62919
921	0.997598	2.50001	2.031367	1.97411	1.42632	946.5	0.997598	2.78428	2.452507	2.394095	1.7862	972	0.997598	2.67893	2.306623	2.18822	1.58697
921.5	0.997598	2.5007	1.986527	1.95242	1.42404	947	0.997598	2.78426	2.440103	2.377985	1.76615	972.5	0.997598	2.67783	2.387657	2.24415	1.61628
922	0.997598	2.50985	2.08259	2.077115	1.53372	947.5	0.997598	2.77793	2.33731	2.230715	1.67681	973	0.997598	2.67776	2.39866	2.284635	1.67271
922.5	0.997598	2.5309	2.21247	2.156815	1.54608	948	0.997598	2.77636	2.077357	2.037865	1.52876	973.5	0.997598	2.66632	2.34726	2.22368	1.61301
923	0.997598	2.53183	2.225527	2.16307	1.51692	948.5	0.997598	2.7879	2.368427	2.32481	1.69274	974	0.997598	2.65975	2.16658	2.07878	1.46431
923.5	0.997598	2.53492	2.222563	2.16335	1.50835	949	0.997598	2.78771	2.46153	2.39467	1.71615	974.5	0.997598	2.66176	2.190753	2.09888	1.48028
924	0.997598	2.54528	2.007057	2.08019	1.48869	949.5	0.997598	2.78953	2.485173	2.41908	1.64838	975	0.997598	2.6567	2.37727	2.26409	1.63994
924.5	0.997598	2.55585	2.080393	2.006125	1.45222	950	0.997598	2.79255	2.492667	2.422925	1.71548	975.5	0.997598	2.65048	2.373403	2.25663	1.62688
925	0.997598	2.5568	2.080393	2.006125	1.47818	950.5	0.997598	2.79255	2.492667	2.422925	1.71548	976	0.997598	2.6427	2.20447	2.105405	1.53322

Figure A.5: Raw data for Figure A.3 and Figure A.4.

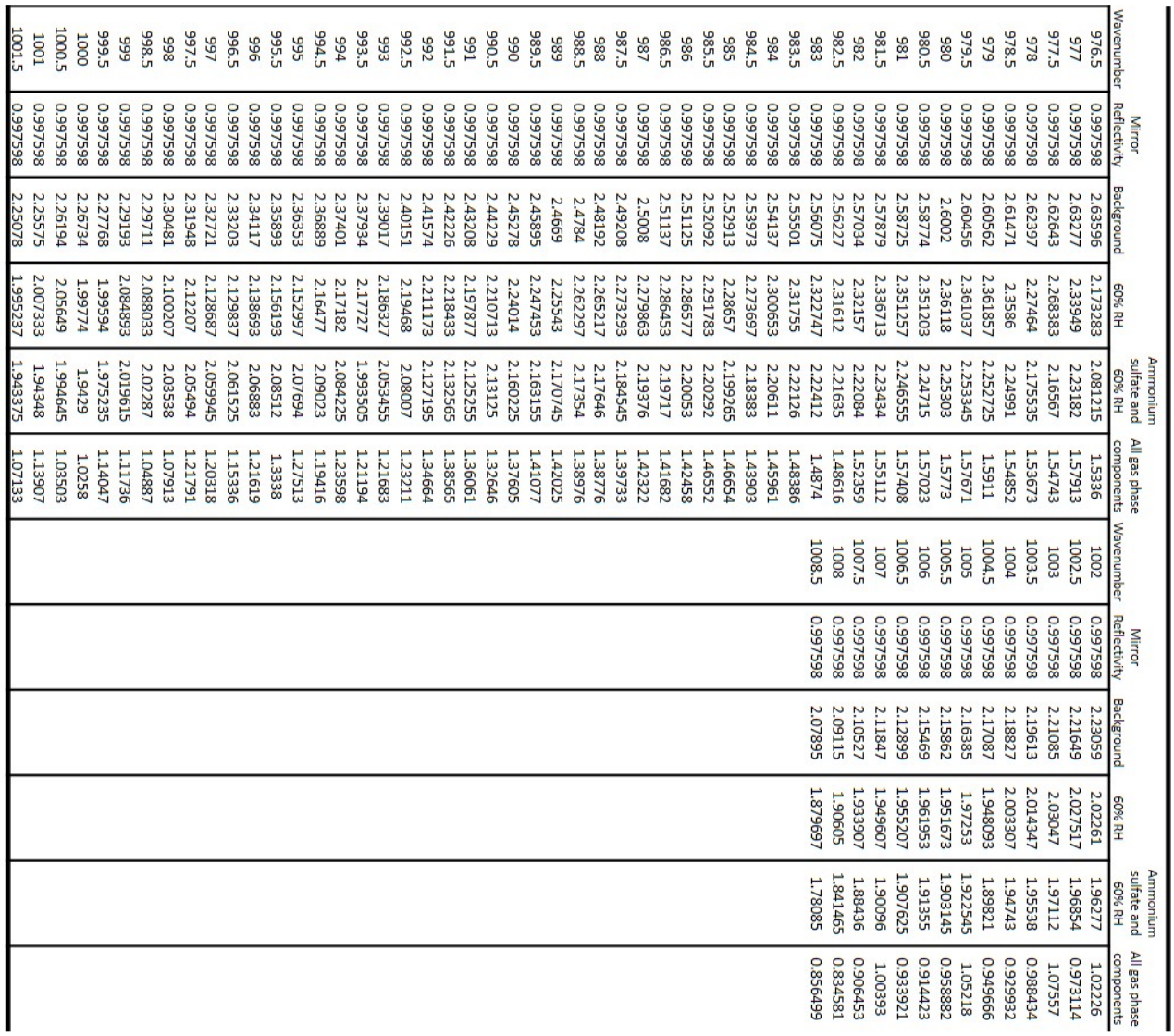

Wavenumber	Mirror Reflectivity	Background	Ammonium sulfate and 60% RH	All gas phase components	Wavenumber	Mirror Reflectivity	Background	60% RH	Ammonium sulfate and 60% RH	All gas phase components
976.5	0.997598	2.63596	2.173283	2.081215	1.5336	1002	0.997598	2.23059	2.02261	1.96277	1.02226
977	0.997598	2.63277	2.33949	2.23182	1.57913	1002.5	0.997598	2.21649	2.027517	1.96854	0.973114
977.5	0.997598	2.62643	2.268383	2.16567	1.54743	1003	0.997598	2.21085	2.03047	1.97112	1.07557
978	0.997598	2.62397	2.27464	2.175535	1.53673	1003.5	0.997598	2.19613	2.014347	1.95538	0.988434
978.5	0.997598	2.61471	2.3586	2.24991	1.54852	1004	0.997598	2.18827	2.003307	1.94743	0.929932
979	0.997598	2.60562	2.361857	2.252725	1.5911	1004.5	0.997598	2.17087	1.948093	1.89821	0.949666
979.5	0.997598	2.60456	2.361037	2.253345	1.57671	1005	0.997598	2.16385	1.97253	1.922545	1.05218
980	0.997598	2.6002	2.36118	2.25303	1.5773	1005.5	0.997598	2.15862	1.951673	1.903145	0.958882
980.5	0.997598	2.58774	2.351203	2.24715	1.57023	1006	0.997598	2.15469	1.961953	1.91355	0.914423
981	0.997598	2.58725	2.351257	2.246555	1.57408	1006.5	0.997598	2.12899	1.955207	1.907625	0.933921
981.5	0.997598	2.57879	2.336713	2.23434	1.55112	1007	0.997598	2.11847	1.949607	1.90096	1.00393
982	0.997598	2.57034	2.32157	2.22084	1.52359	1007.5	0.997598	2.10527	1.933907	1.88436	0.906453
982.5	0.997598	2.56227	2.31612	2.21635	1.48616	1008	0.997598	2.09115	1.90605	1.841465	0.834581
983	0.997598	2.56075	2.322747	2.22412	1.4874	1008.5	0.997598	2.07895	1.879697	1.78085	0.856499
983.5	0.997598	2.55501	2.31755	2.22126	1.48386						
984	0.997598	2.54137	2.300653	2.20611	1.45961						
984.5	0.997598	2.53973	2.273697	2.18383	1.43903						
985	0.997598	2.52913	2.28657	2.199265	1.46654						
985.5	0.997598	2.52092	2.291783	2.20292	1.46552						
986	0.997598	2.51125	2.286577	2.20053	1.42458						
986.5	0.997598	2.51137	2.286453	2.19717	1.41682						
987	0.997598	2.5008	2.279863	2.19376	1.42322						
987.5	0.997598	2.49208	2.273293	2.184545	1.39733						
988	0.997598	2.48192	2.265217	2.17646	1.38776						
988.5	0.997598	2.4784	2.262297	2.17354	1.38976						
989	0.997598	2.4669	2.25543	2.170745	1.42025						
989.5	0.997598	2.45895	2.247453	2.163155	1.41077						
990	0.997598	2.45278	2.24014	2.160225	1.37605						
990.5	0.997598	2.44229	2.210713	2.13125	1.32646						
991	0.997598	2.43208	2.197877	2.125255	1.36061						
991.5	0.997598	2.42226	2.218433	2.132565	1.38565						
992	0.997598	2.41574	2.211173	2.127195	1.34664						
992.5	0.997598	2.40151	2.19468	2.08007	1.23211						
993	0.997598	2.39017	2.186327	2.053455	1.21683						
993.5	0.997598	2.37934	2.17727	1.993505	1.21194						
994	0.997598	2.37401	2.17182	2.084225	1.23598						
994.5	0.997598	2.36889	2.16477	2.09023	1.19416						
995	0.997598	2.36353	2.152997	2.07694	1.27513						
995.5	0.997598	2.35893	2.156193	2.08512	1.3338						
996	0.997598	2.34117	2.138693	2.06883	1.21619						
996.5	0.997598	2.33203	2.129837	2.061525	1.15336						
997	0.997598	2.32721	2.128687	2.059945	1.20318						
997.5	0.997598	2.31948	2.12207	2.05494	1.21791						
998	0.997598	2.30481	2.100207	2.03538	1.07913						
998.5	0.997598	2.29711	2.088033	2.02287	1.04887						
999	0.997598	2.29193	2.084893	2.019615	1.11736						
999.5	0.997598	2.27768	1.99594	1.975235	1.14047						
1000	0.997598	2.26734	1.99774	1.9429	1.0258						
1000.5	0.997598	2.26194	2.05649	1.994645	1.03503						
1001	0.997598	2.25575	2.007333	1.94348	1.13907						
1001.5	0.997598	2.25078	1.995237	1.943375	1.07133						

Figure A.6: Raw data for Figure A.3 and Figure A.4.

Wavenumber	Ammonium sulfate and 60% RH	All gas phase components	Monomethyl amine control	Δabsorbance	Wavenumber	Ammonium sulfate and 60% RH	All gas phase components	Monomethyl amine control	Δabsorbance	Wavenumber	Ammonium sulfate and 60% RH	All gas phase components	Monomethyl amine control	Δabsorbance
900	0.00158	0.00631	0.00624	0.00007	925.5	0.00188	0.00444	0.00391	0.00052	951	0.00151	0.00463	0.00446	0.00018
900.5	0.00151	0.00605	0.00586	0.00019	926	0.00168	0.00432	0.00406	0.00026	951.5	0.00158	0.00449	0.00413	0.00036
901	0.00158	0.00558	0.00559	-0.00001	926.5	0.00210	0.00491	0.00436	0.00055	952	0.00156	0.00426	0.00402	0.00024
901.5	0.00155	0.00587	0.00577	0.00010	927	0.00224	0.00530	0.00450	0.00080	952.5	0.00167	0.00426	0.00424	0.00002
902	0.00154	0.00603	0.00602	0.00002	927.5	0.00190	0.00528	0.00473	0.00055	953	0.00187	0.00418	0.00407	0.00012
902.5	0.00157	0.00621	0.00612	0.00010	928	0.00236	0.00540	0.00453	0.00087	953.5	0.00212	0.00460	0.00429	0.00031
903	0.00156	0.00683	0.00703	-0.00020	928.5	0.00248	0.00538	0.00447	0.00091	954	0.00175	0.00516	0.00521	-0.00005
903.5	0.00156	0.00667	0.00626	0.00041	929	0.00225	0.00586	0.00479	0.00106	954.5	0.00172	0.00486	0.00483	0.00003
904	0.00156	0.00599	0.00566	0.00033	929.5	0.00222	0.00577	0.00461	0.00116	955	0.00194	0.00440	0.00444	-0.00004
904.5	0.00163	0.00590	0.00594	-0.00004	930	0.00243	0.00595	0.00469	0.00126	955.5	0.00219	0.00388	0.00399	-0.00011
905	0.00232	0.00542	0.00521	0.00022	930.5	0.00283	0.00690	0.00516	0.00174	956	0.00155	0.00359	0.00357	0.00001
905.5	0.00251	0.00564	0.00549	0.00015	931	0.00269	0.00692	0.00477	0.00215	956.5	0.00149	0.00373	0.00372	0.00002
906	0.00189	0.00563	0.00540	0.00023	931.5	0.00252	0.00622	0.00455	0.00167	957	0.00148	0.00386	0.00393	-0.00007
906.5	0.00178	0.00548	0.00542	0.00006	932	0.00200	0.00531	0.00443	0.00088	957.5	0.00149	0.00395	0.00392	0.00004
907	0.00224	0.00589	0.00534	0.00055	932.5	0.00197	0.00533	0.00449	0.00084	958	0.00150	0.00403	0.00400	0.00003
907.5	0.00316	0.00626	0.00511	0.00115	933	0.00173	0.00488	0.00436	0.00052	958.5	0.00151	0.00423	0.00415	0.00008
908	0.00407	0.00535	0.00501	0.00034	933.5	0.00168	0.00481	0.00436	0.00045	959	0.00211	0.00502	0.00489	0.00013
908.5	0.00321	0.00497	0.00487	0.00010	934	0.00169	0.00508	0.00462	0.00046	959.5	0.00228	0.00504	0.00488	0.00016
909	0.00241	0.00485	0.00480	0.00005	934.5	0.00156	0.00495	0.00455	0.00040	960	0.00185	0.00494	0.00493	0.00001
909.5	0.00249	0.00491	0.00482	0.00009	935	0.00153	0.00469	0.00455	0.00014	960.5	0.00178	0.00518	0.00510	0.00008
910	0.00230	0.00499	0.00495	0.00004	935.5	0.00154	0.00413	0.00389	0.00023	961	0.00171	0.00540	0.00509	0.00030
910.5	0.00213	0.00470	0.00490	-0.00020	936	0.00148	0.00410	0.00403	0.00007	961.5	0.00168	0.00464	0.00438	0.00026
911	0.00182	0.00495	0.00486	0.00009	936.5	0.00148	0.00465	0.00466	-0.00001	962	0.00177	0.00495	0.00445	0.00049
911.5	0.00179	0.00471	0.00455	0.00016	937	0.00151	0.00489	0.00479	0.00010	962.5	0.00174	0.00444	0.00389	0.00055
912	0.00182	0.00460	0.00453	0.00008	937.5	0.00145	0.00508	0.00492	0.00016	963	0.00180	0.00483	0.00418	0.00065
912.5	0.00188	0.00515	0.00512	0.00003	938	0.00143	0.00483	0.00448	0.00034	963.5	0.00195	0.00553	0.00473	0.00080
913	0.00220	0.00518	0.00488	0.00030	938.5	0.00143	0.00428	0.00416	0.00011	964	0.00199	0.00584	0.00523	0.00061
913.5	0.00223	0.00474	0.00487	-0.00014	939	0.00143	0.00447	0.00438	0.00009	964.5	0.00223	0.00765	0.00520	0.00245
914	0.00180	0.00496	0.00504	-0.00007	939.5	0.00144	0.00450	0.00441	0.00010	965	0.00257	0.00857	0.00731	0.00126
914.5	0.00176	0.00479	0.00482	-0.00002	940	0.00150	0.00426	0.00421	0.00005	965.5	0.00270	0.00887	0.00723	0.00164
915	0.00175	0.00494	0.00508	-0.00014	940.5	0.00193	0.00424	0.00418	0.00006	966	0.00285	0.00924	0.00738	0.00186
915.5	0.00173	0.00514	0.00521	-0.00007	941	0.00186	0.00434	0.00433	0.00000	966.5	0.00330	0.00864	0.00660	0.00205
916	0.00168	0.00477	0.00488	-0.00010	941.5	0.00143	0.00463	0.00460	0.00003	967	0.00344	0.00811	0.00581	0.00230
916.5	0.00165	0.00482	0.00478	0.00004	942	0.00141	0.00468	0.00454	0.00015	967.5	0.00304	0.00734	0.00539	0.00196
917	0.00180	0.00478	0.00470	0.00008	942.5	0.00140	0.00439	0.00453	-0.00014	968	0.00229	0.00617	0.00504	0.00113
917.5	0.00202	0.00463	0.00455	0.00008	943	0.00142	0.00420	0.00407	0.00013	968.5	0.00174	0.00520	0.00491	0.00030
918	0.00216	0.00455	0.00449	0.00006	943.5	0.00145	0.00439	0.00419	0.00020	969	0.00162	0.00457	0.00478	-0.00021
918.5	0.00184	0.00474	0.00470	0.00003	944	0.00178	0.00441	0.00427	0.00013	969.5	0.00160	0.00441	0.00429	0.00012
919	0.00166	0.00479	0.00469	0.00011	944.5	0.00190	0.00416	0.00417	0.00000	970	0.00163	0.00452	0.00470	-0.00018
919.5	0.00166	0.00468	0.00455	0.00013	945	0.00144	0.00422	0.00413	0.00010	970.5	0.00167	0.00447	0.00452	-0.00005
920	0.00169	0.00461	0.00458	0.00002	945.5	0.00144	0.00428	0.00413	0.00015	971	0.00178	0.00438	0.00440	-0.00002
920.5	0.00209	0.00490	0.00483	0.00007	946	0.00151	0.00403	0.00388	0.00015	971.5	0.00221	0.00424	0.00416	0.00008
921	0.00284	0.00519	0.00498	0.00021	946.5	0.00156	0.00379	0.00370	0.00009	972	0.00223	0.00462	0.00407	0.00055
921.5	0.00300	0.00507	0.00490	0.00018	947	0.00164	0.00389	0.00379	0.00010	972.5	0.00193	0.00462	0.00426	0.00036
922	0.00222	0.00455	0.00453	0.00002	947.5	0.00236	0.00395	0.00381	0.00014	973	0.00171	0.00427	0.00435	-0.00007
922.5	0.00183	0.00489	0.00463	0.00026	948	0.00348	0.00436	0.00390	0.00046	973.5	0.00199	0.00454	0.00462	-0.00008
923	0.00180	0.00525	0.00500	0.00025	948.5	0.00191	0.00429	0.00418	0.00010	974	0.00280	0.00539	0.00461	0.00078
923.5	0.00181	0.00536	0.00512	0.00024	949	0.00157	0.00441	0.00431	0.00010	974.5	0.00269	0.00531	0.00544	-0.00013
924	0.00234	0.00510	0.00478	0.00031	949.5	0.00150	0.00489	0.00484	0.00006	975	0.00174	0.00449	0.00448	0.00001
924.5	0.00316	0.00478	0.00417	0.00060	950	0.00146	0.00516	0.00508	0.00008	975.5	0.00176	0.00458	0.00467	-0.00009
925	0.00287	0.00475	0.00408	0.00067	950.5	0.00146	0.00454	0.00449	0.00005	976	0.00258	0.00473	0.00476	-0.00003

Figure A.7: Raw data for Figure 4.1, 4.2, 4.3, and 4.4.

Wavenumber	Ammonium sulfate and 60% RH	All gas phase components	Monomethyl amine control	Δabsorbance	Wavenumber	Ammonium sulfate and 60% RH	All gas phase components	Monomethyl amine control	Δabsorbance
976.5	0.00270	0.00458	0.00456	0.00002	1002	0.00163	0.01251	0.01349	-0.00098
977	0.00182	0.00494	0.00513	-0.00019	1002.5	0.00152	0.01387	0.01480	-0.00094
977.5	0.00216	0.00492	0.00502	-0.00010	1003	0.00147	0.01127	0.01233	-0.00106
978	0.00210	0.00510	0.00521	-0.00011	1003.5	0.00150	0.01335	0.01460	-0.00125
978.5	0.00165	0.00537	0.00545	-0.00008	1004	0.00151	0.01499	0.01674	-0.00174
979	0.00160	0.00493	0.00487	0.00005	1004.5	0.00177	0.01404	0.01710	-0.00306
979.5	0.00160	0.00508	0.00512	-0.00004	1005	0.00155	0.01148	0.01241	-0.00093
980	0.00158	0.00507	0.00511	-0.00004	1005.5	0.00166	0.01381	0.01412	-0.00031
980.5	0.00156	0.00512	0.00518	-0.00006	1006	0.00156	0.01524	0.01672	-0.00149
981	0.00156	0.00507	0.00511	-0.00003	1006.5	0.00145	0.01458	0.01694	-0.00235
981.5	0.00160	0.00526	0.00528	-0.00002	1007	0.00144	0.01254	0.01338	-0.00084
982	0.00163	0.00550	0.00552	-0.00002	1007.5	0.00149	0.01528	0.01826	-0.00298
982.5	0.00163	0.00592	0.00551	0.00040					
983	0.00158	0.00594	0.00612	-0.00018					
983.5	0.00157	0.00597	0.00610	-0.00013					
984	0.00160	0.00619	0.00638	-0.00019					
984.5	0.00171	0.00632	0.00648	-0.00015					
985	0.00158	0.00606	0.00622	-0.00016					
985.5	0.00153	0.00609	0.00614	-0.00005					
986	0.00150	0.00661	0.00675	-0.00015					
986.5	0.00152	0.00669	0.00690	-0.00021					
987	0.00149	0.00659	0.00665	-0.00006					
987.5	0.00151	0.00688	0.00705	-0.00016					
988	0.00151	0.00697	0.00718	-0.00021					
988.5	0.00151	0.00692	0.00714	-0.00021					
989	0.00148	0.00650	0.00663	-0.00014					
989.5	0.00148	0.00658	0.00663	-0.00005					
990	0.00147	0.00704	0.00724	-0.00020					
990.5	0.00159	0.00760	0.00789	-0.00030					
991	0.00158	0.00706	0.00723	-0.00017					
991.5	0.00150	0.00674	0.00684	-0.00010					
992	0.00150	0.00727	0.00723	0.00004					
992.5	0.00172	0.00883	0.00725	0.00157					
993	0.00183	0.00893	0.00818	0.00075					
993.5	0.00217	0.00863	0.00777	0.00086					
994	0.00156	0.00879	0.00835	0.00044					
994.5	0.00150	0.00958	0.01005	-0.00047					
995	0.00156	0.00808	0.00850	-0.00042					
995.5	0.00149	0.00721	0.00758	-0.00037					
996	0.00150	0.00904	0.00882	0.00023					
996.5	0.00150	0.01019	0.01092	-0.00073					
997	0.00149	0.00922	0.00990	-0.00068					
997.5	0.00148	0.00892	0.00931	-0.00039					
998	0.00153	0.01162	0.00930	0.00232					
998.5	0.00157	0.01225	0.01311	-0.00086					
999	0.00157	0.01067	0.01039	0.00028					
999.5	0.00180	0.00988	0.00983	0.00005					
1000	0.00197	0.01228	0.01310	-0.00082					
1000.5	0.00158	0.01240	0.01361	-0.00121					
1001	0.00190	0.00970	0.01040	-0.00070					
1001.5	0.00188	0.01118	0.01102	0.00016					

Figure A.8: Raw data for Figure 4.1, 4.2, 4.3, and 4.4.

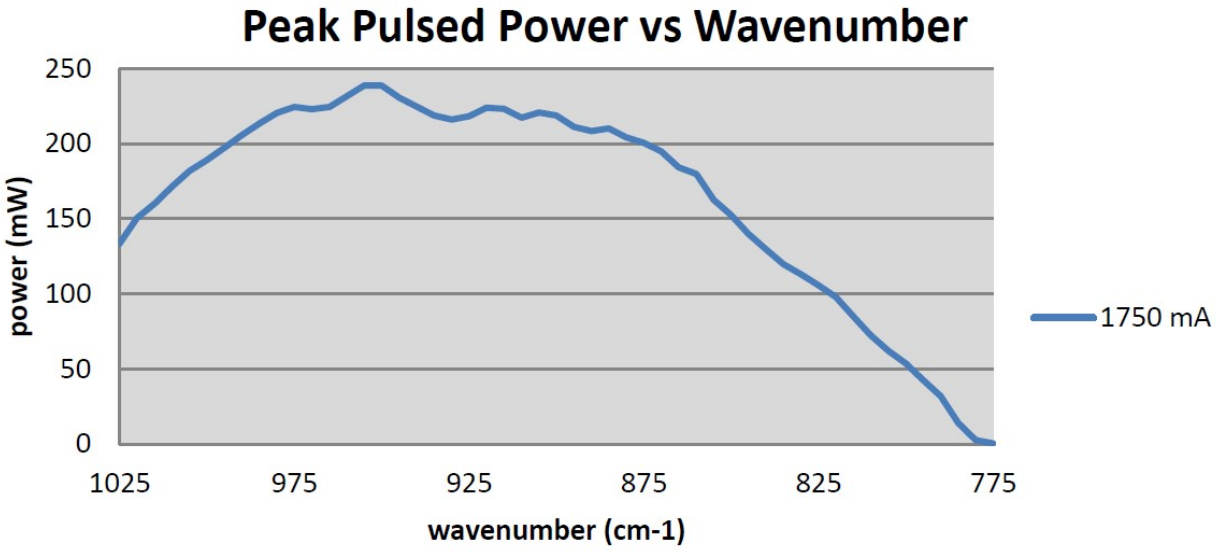

Figure A.9: Laser power diagnostics over the wavelength range recorded by Daylight Solutions.

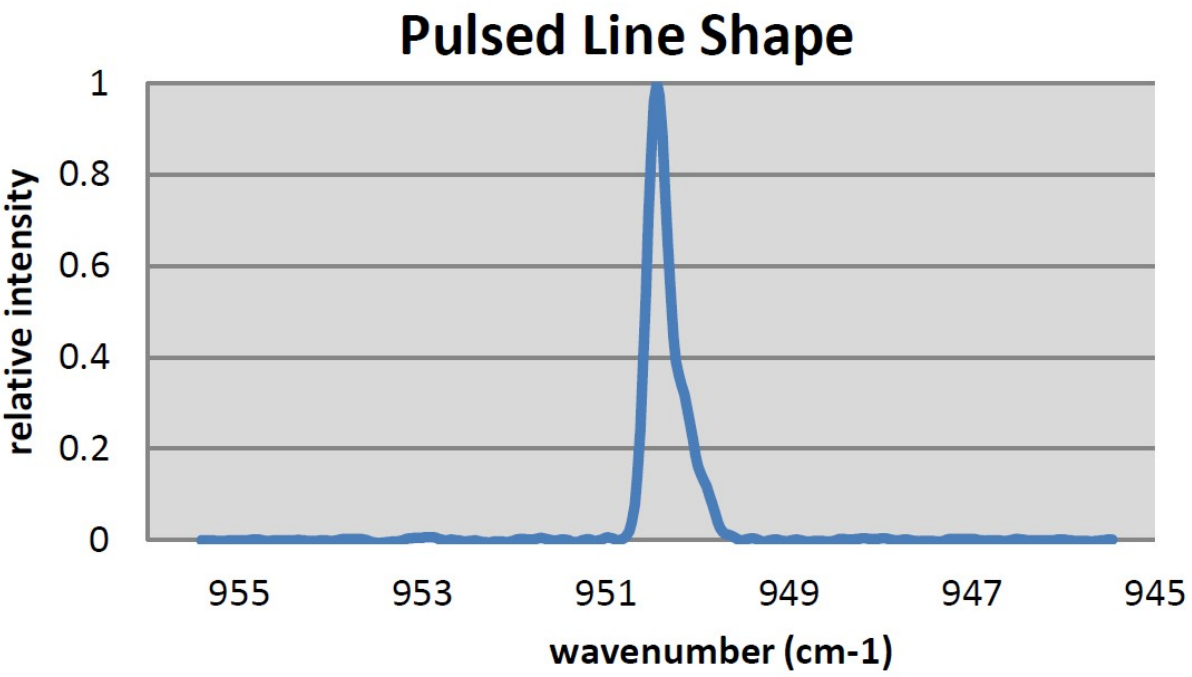

Figure A.10: Laser line shape diagnostics for a pulse at 950 cm^{-1} recorded by Daylight Solutions. The line shape is asymmetrical, or chirped, resulting in an effective line width of the pulse of <1 cm^{-1}. The shape and width of the laser pulse is not appropriate for rotational spectroscopy or for peaks with a FWHM less than the line width of the laser pulse.

A.1.3. Additional particle charge equations

Boltzmann's equilibrium charge distribution on particle surfaces.[16]

$$f_n = \left(\frac{K_E e^2}{\pi d_p k_b T}\right)^{1/2} \exp\left(\frac{-K_E n^2 e^2}{d_p k_b T}\right) \tag{A.21}$$

Fraction of particles of a given size having n positive or negative elementary charge units (f_n) where K_E is the constant of proportionality based on the units (9.0×10^9 $N \cdot m^2/C^2$), e is the charge of an electron ($1.60 \times 10^{-}19$ C), d_p is the particle diameter, k_b is the Boltzmann's constant, T in K, and n is the number of charges on a particle of size d_p.

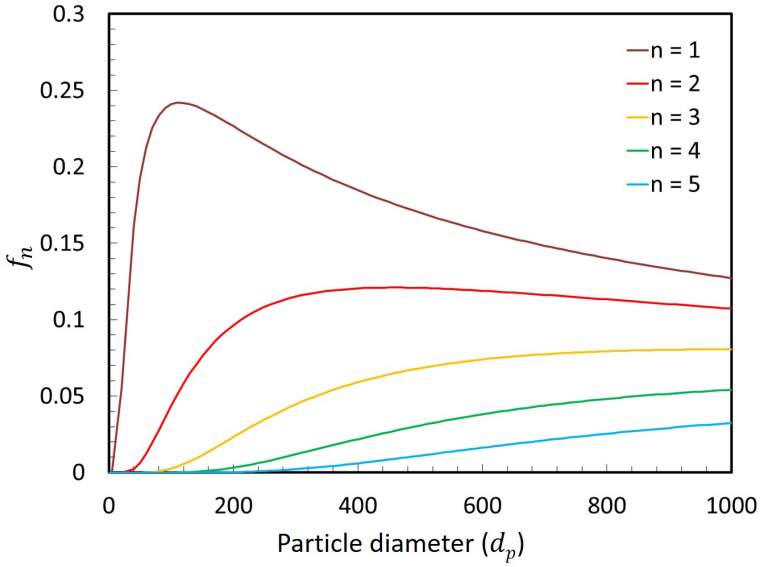

Figure A.11: Boltzmann's equilibrium charge distribution for ultrafine and fine particulate matter for n =1–5.

Coulomb force coagulation correction factor derivation. See Reference 143 for more information on the derivation.

$$W_c = (R_{p1} + R_{p2}) \int_{R_{p1}+R_{p2}}^{\infty} \frac{1}{x^2} \left(\frac{\Phi_c(x)}{k_b T} \right) dx \tag{A.22}$$

Potential energy of the interaction between two particles with charge z_1 and z_2 (including sign) at a distance r between particle centers and e is electronic charge. The dielectric constant for 1 atm air is 1.0005 (ε) and the permittivity of vacuum (ε_0) is 8.754×10^{-12} F/m.

$$\Phi_c = \frac{z_1 z_2 e^2}{4\pi\varepsilon_0 \varepsilon r} \tag{A.23}$$

Substitution of Φ_c into Equation A.22 yields the following equations.

$$W_c = \frac{e^{\kappa} - 1}{\kappa} \tag{A.24}$$

$$\kappa = \frac{z_1 z_2 e^2}{4\pi\varepsilon_0 \varepsilon (R_{p1} + R_{p2}) k_b T} \tag{A.25}$$